Morphing trailing edge wings for transport aircraft

A conceptual assessment

T.H. Leniger

Technische Universiteit Delft

Delft University of Technology

Challenge the future

Morphing trailing edge wings for transport aircraft

A conceptual assessment

by

T.H. Leniger

in partial fulfillment of the requirements for the degree of

Master of Science
in Aerospace Engineering

at the Delft University of Technology,
to be defended publicly on Thursday, July 9th, 2026 at 9:30.

Supervisors:	Dr. ir. M.F.M. Hoogreef	TU Delft
	MEng. P. Georgopoulos	TU Delft
Thesis committee:	Dr. ir. R. Vos,	TU Delft
	Dr. ir. D.M.J. Peeters,	TU Delft

An electronic version of this thesis is available at http://repository.tudelft.nl/.
Cover image: Air Force Research Laboratory Aerospace Systems Directorate, May 2015

Abstract

Aviation was responsible for 2.5% of global energy-related CO_2 emissions in 2023, and the market is projected to double over the next two decades. This growth conflicts with international targets to reach net-zero emissions by 2050. Of the available mitigation pathways, reducing the in-flight energy consumption of aircraft is the most immediately deployable, as it does not depend on new ground infrastructure. The main contributor to the required in-flight energy is aerodynamic drag, which in conventional tube-and-wing aircraft is governed largely by the main wing. A fixed wing is optimized for a single design point, yet operates off-design for much of its mission. Morphing wings can change shape in flight and adapt to the conditions at hand, which offers a route to lower drag across the mission. Aircraft-level studies that quantify this benefit at conceptual design level, while accounting for the accompanying sizing effects, are sparse.

The present thesis assesses the effect of implementing chordwise two-degree-of-freedom (2-DoF) compliant camber-twist morphing trailing edge wings on the sizing, configuration, and performance of CS-25 transport aircraft. Block-fuel consumption is adopted as the primary figure of merit, because it captures the trade between the improved aerodynamic efficiency and the sizing penalties that morphing wings introduce.

Three methodological contributions support this assessment. First, a parametrization method describes the morphed shape of an arbitrary base airfoil from three inputs: the rear spar location and two pseudo-deflection angles. Control points on the camberline are rotated in sequence and fitted with a fourth-order polynomial, after which the airfoil surfaces are reconstructed while preserving the arc length of the suction-side skin, which reflects the physical constraint of the compliant structure. Applied at several spanwise stations, the method represents camber-twist morphing at wing level. Second, the Aircraft Trimmed Performance Analysis Tool (ATPAT) evaluates the trimmed cruise aerodynamic efficiency of morphing wing aircraft. It combines a vortex lattice method with strip theory and simple sweep theory to resolve the induced, viscous, pressure, and wave drag within a runtime of seconds to a minute per evaluation. ATPAT was validated against experimental and computational data on the Fokker 100 and integrated into the Initiator aircraft design toolbox with Bayesian and gradient-based optimizers. Third, the two sizing inputs that have no empirical basis for morphing systems are handled explicitly: the morphing system mass is treated as a parameter bounded above by the specific mass of Fowler flaps, and the achievable high-lift increment is estimated with RANS CFD, yielding a conservative sectional lift increase of 0.63 at full deflection.

The methodology was applied to two reference aircraft, the ATR 72-600 and the Fokker 100. When held to the same top-level requirements, both morphing designs were heavier and had a larger wing area than their conventional counterparts, a direct consequence of the high-lift deficit that makes field performance the limiting constraint. A relaxation of the landing field length of roughly 20% returned the sizing outcomes close to those of the reference aircraft. On the ATR 72-600, the aerodynamic gains did not justify the accompanying penalties: the morphing design at best matched the conventional block fuel on the harmonic mission, and used 6% and 4% more fuel on a shorter $750\,\mathrm{km}$ payload mission and on its maximum-fuel mission. The Fokker 100 achieved a block-fuel reduction of up to 3.6% on its harmonic mission after a 17.5% relaxation of the landing field length, at which point it was sized almost identically to the reference. Its transonic cruise offers an additional pathway to lower drag, since camber morphing can be used to reduce wave drag.

The main finding is conditional on several assumptions. The relative contributions of near-equal sizing and of wave drag reduction to the Fokker 100 benefit were not isolated, and a component-wise drag decomposition is needed to establish whether the result transfers to other transonic transport aircraft. The morphing system mass remains the largest single source of uncertainty and would be narrowed by mass data from a full-scale demonstrator. The high-lift performance is based on only two airfoils and may overestimate the sizing penalty, for which wind tunnel testing is preferred over further RANS. Finally, the block fuel was evaluated at a single cruise point per mission. A segmented analysis is expected to raise the estimated benefit of morphing.

Preface

This report marks the end of an incredible time in Delft. Over the last six years I have developed academically, personally, and I have made friends for life. Studying aerospace engineering has felt like a privilege, as I was allowed to dive as deep as it gets into topics that have interested me for as long as I can remember. I enjoyed working on the research in this report because of its multidisciplinary nature, and because of the practical approach to complex problems it required. I hope you enjoy reading this report as much as I did writing it.

I would like to thank my supervisors, Maurice and Panos, for their time, effort, and continuous support throughout the project. They gave me the freedom to explore the topic and approach it in my own way, while offering their views and advice in a kind way. This really helped putting things into perspective and determine the path to follow. I enjoyed the weekly meetings, especially near the end, where I noticed their interest in the results I was excited about.

I am also grateful to my family for supporting me throughout my time as a student, and for being there to celebrate the milestones. A special thank you goes out to my parents, who allowed and enabled me to study the things that I am interested in. Pap en mam, dank jullie wel. To the friends that I have made in Delft, I would like to say thank you for making the last six years the best years of my life so far. It is hard to believe that everything I have experienced with you happened over such a short period of time.

Who knows what is next? The end of my time as a student at the Delft University of Technology marks the start of a new exciting time. With that, I would like to wish you, the reader, a good and engaging read.

T.H. Leniger
Delft, June 2026

Contents

Nomenclature

Abbreviations

Abbreviation	Definition
AEO	All Engines Operative
ATPAT	Aircraft Trimmed Performance Analysis Tool
CFD	Computational Fluid Dynamics
CFL	Courant–Friedrichs–Lewy
CS	Certification Specifications
CST	Class Shape Transformation
DES	Detached Eddy Simulation
DoF	Degree(s) of Freedom
GHG	Greenhouse gas
HLD	High-Lift Device(s)
IATA	International Air Transport Association
ISA	International Standard Atmosphere
LE	Leading Edge
LES	Large Eddy Simulation
LM	Langtry-Menter (extension of the $k-\omega$ SST model)
MAC	Mean Aerodynamic Chord
MDO	Multidisciplinary Design Optimization
NPLS	Non-planar Lifting Surface
OEI	One Engine Inoperative
OOP	Object-Oriented Programming
RANS	Reynolds-Averaged Navier-Stokes equations
SA	Spalart-Allmaras
SST	Shear Stress Transport
TE	Trailing Edge
VGK	Viscous Garabedian Korn
VLM	Vortex Lattice Method

Symbols

Symbol	Definition	Unit
A	Aspect ratio	[-]
c	Chord	[m]
$\bar{c}$	Mean Aerodynamic Chord	[m]
C_d	Two-dimensional drag coefficient	[-]
C_D	Three-dimensional drag coefficient	[-]
C_{D_0}	Three-dimensional zero-lift drag coefficient	[-]
CGR	Climb gradient	[-]
C_f	Friction coefficient	[-]
c_j	Specific fuel consumption	$[\mathrm{kg\,h^{-1}\,N^{-1}}]$
C_l	Two-dimensional lift coefficient	[-]
C_L	Three-dimensional lift coefficient	[-]
C_M	Three-dimensional moment coefficient	[-]
C_{M_0}	Three-dimensional zero-angle-of-attack moment coefficient	[-]

Symbol	Definition	Unit
C_{M_α}	Three-dimensional derivative of moment coefficient w.r.t angle of attack	[-]
D	Drag	[N]
e	Oswald efficiency factor	[-]
FF	Fuel Fraction	[-]
i_f	Angle of the fuselage centerline w.r.t the horizontal	[deg]/[rad]
i_h	Angle of the centerline of the engines w.r.t the fuselage centerline	[deg]/[rad]
l	Length	[m]
L	Lift	[N]
M	Mach number	[-]
R	Range	[m]
Re	Reynolds number	[-]
ROC	Rate of Climb	[m s^{-1}]
S	Surface area	[m^2]
SM	Stability margin in percentage of Mean Aerodynamic Chord	[-]
T	Thrust	[N]
V	Velocity	[m s^{-1}]
W	Weight	[N]
x	Position along x-axis	[m]
y	Position along y-axis	[m]
z	Position along z-axis	[m]
α	Angle of attack	[deg]/[rad]
δ	Deflection	[deg]/[rad]
ϵ	Geometric twist angle	[deg]/[rad]
γ	Flight path angle	[deg]/[rad]
ρ	Density	[kg m^{-3}]
λ	Taper ratio OR shape factor	[-] / [-]
Λ	Sweep angle	[deg]/[rad]
μ	Mechanical friction coefficient	[-]

Subscripts

Subscript	Definition
app	Approach
cr	Cruise
E	Empty
F	Fuel
L	Landing
LOF	Lift-off
OE	Operating Empty
PL	Payload
pwr	Power
$struct$	Structural
$syst$	Systems
tfo	Trapped fuel and oil
TO	Take-off

1 Introduction

In 2023, the commercial aviation market was responsible for 2.5% of global anthropogenic CO_2 emissions related to energy, reaching more than 90% of pre-Covid-19 levels[1]. After the recovery from the pandemic, Airbus projects the market to continue growing at an average annual rate of 3.6% [1]. This implies that the aviation market is set to double in size over the next twenty years. At the same time, the United Nations (UN) Net Zero Coalition[2] outlines that global greenhouse gas (GHG) emissions must be reduced by 45% before 2030, and reach net-zero by 2050 to avoid the worst effects of climate change. The already significant contribution of the aviation market to global CO_2 emissions, and the expected growth of the market, are conflicting with the objective outlined by the UN. Therefore, there is a clear need for reducing the climate impact of the aviation market. In order to realize this, the International Air Transport Association (IATA) published a roadmap in 2023, highlighting key technologies for the reduction of the climate impact of aircraft [2]. These technologies are divided into three pillars: batteries & hybrid electric aircraft, hydrogen aircraft & sustainable aviation fuel, and the reduction of in-flight energy consumption. Aside from design and certification challenges for hybrid-electric and hydrogen aircraft, the implementation of these technologies also requires significant adaptations to ground infrastructure. The reduction of in-flight energy, however, is independent of ground infrastructure and can be pursued alongside existing propulsion technologies, making it the most immediately deployable of the three.

In the aircraft technology roadmap, the reduction of in-flight energy consumption is split up over three areas of innovation: propulsion, aircraft systems, and aerodynamics & structures. The focus in the propulsion area is on extracting more useful energy from the fuel, while emitting less greenhouse gasses. The focus in the latter two areas is on reducing the power required to operate the aircraft. The main contributor to this required power is the aerodynamic drag in flight, which is directly tied to an aircraft's aerodynamic- and structural characteristics. In conventional tube-and-wing aircraft, the aerodynamic characteristics are predominantly determined by the main wing. The design of the main wing is subject to numerous requirements and constraints. It should perform acceptably everywhere throughout the flight envelope and optimally in the design condition. Acceptably and optimally are keywords here, indicating that the design of the wing is inherently compromised between different phases of flight. On top of that, the mission profile, in terms of aircraft mass, airspeed, and flight altitude, varies between flights. Yet, the wing is designed and optimized with respect to a single nominal condition: the design point [3]. This means that the wing is operating in off-design conditions for significant portions of its operating time.

The implementation of morphing wings could help mitigate the challenge described above. Morphing wings can change shape in flight, allowing them to adapt to the operating conditions at hand. This ability allows for in-flight optimization of the wing shape to minimize drag, leading to a reduction in in-flight energy consumption. Realizing this potential, however, requires an assessment of the technology at aircraft level, factoring in the effects of morphing wings on the aerodynamic characteristics of an aircraft, as well as the implications on aircraft sizing and configuration. The conceptual-level studies

[1]International Energy Agency https://www.iea.org/energy-system/transport/aviation
[2]https://www.un.org/en/climatechange/net-zero-coalition

that quantify these effects and how they weigh against each other are currently sparse in literature. This is the gap that the present study aims to address, as formalized in section 1.1.

1.1. Scope & research objective

To narrow the scope of this study, the type of morphing wings considered will be defined first. Morphing wings can be classified based on the type of shape change they undergo [4]. Distinction is made between large-scale, and small-scale changes. Large-scale changes are often called planform morphing, of which variable sweep wings are an example. The small-scale changes are often referred to as out-of-plane morphing, and include camber morphing, and wing warping or twist morphing. This thesis focuses on compliant camber-twist morphing trailing edge wings. The potential performance improvements of these wings include reduced friction drag, pressure drag, induced drag, and wave drag for aircraft operating in transonic conditions [5]. Chapter 2 will further discuss the classification of morphing wings, as well as detail the drag reduction mechanisms.

The specific concept upon which the present study is based is a chordwise two-degree-of-freedom (2 DoF) compliant camber-twist morphing trailing edge wing, proposed by Georgopoulos *et al.* [6]. The concept stands out by exhibiting two degrees of freedom in chordwise direction, potentially enabling larger morphing deformations, as well as morphing into reflexed shapes. The latter property allows for decoupling of the aerodynamic moment and lift generated by airfoils. This has the potential to reduce the required load on the horizontal stabilizer to trim the aircraft, which leads to a reduction of trim drag. The concept achieves twist morphing by differential actuation at different spanwise positions. A cross-sectional view of the concept is presented in Figure 1.1.

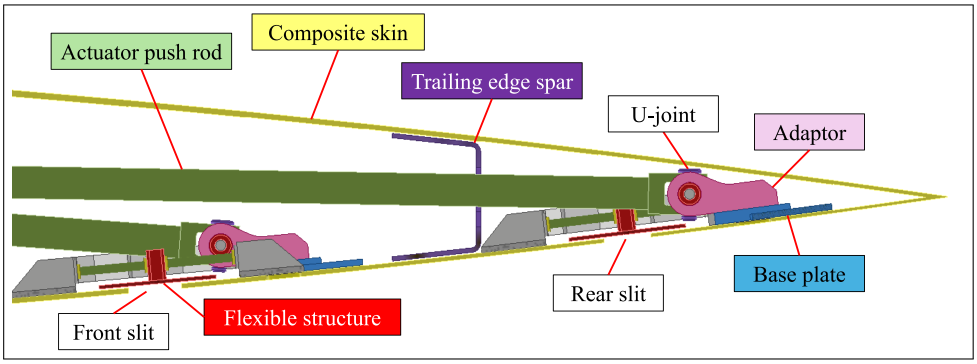

Figure 1.1: Cross-sectional view of the 2-DoF morphing trailing edge wing concept [6]

The aircraft considered in the present study fall under the CS-25 regulations. These regulations apply to turbine powered aircraft with a maximum certified take-off mass above 5700 kg [7, 8]. This group of aircraft is selected for its significant contribution to the climate impact of aviation compared to general aviation, and the willingness of the market to adopt solutions that increase efficiency. The conceptual focus of this study, the concept by Georgopoulos *et al.* [6], and the aircraft scope together form the research objective for the present study, as formalized below.

> *The present thesis aims to assess the effects of implementing chordwise 2-DoF morphing trailing edge wings on the sizing and configuration of CS-25 transport aircraft at conceptual design level, and to analyze the performance of these aircraft relative to conventional reference designs*

The main research objective consists of three distinct parts, which are captured in the sub-objectives stated below.

1. To investigate the effect of implementing chordwise 2-DoF morphing trailing edge wings on the conceptual design of CS-25 aircraft, quantified by changes in take-off weight, wing area, and configuration relative to a reference design.

2. To investigate the sensitivity of the conceptual design outcome of CS-25 aircraft with 2-DoF morphing trailing edge wings to top-level design requirements.

3. To analyze the performance of conceptual CS-25 aircraft with 2-DoF morphing trailing edge wings and compare it to the performance of reference conceptual designs.

With the aim of the present thesis laid out, section 1.2 will motivate the structure of the present report.

1.2. Structure

This thesis is divided into three parts. The first covers the literature review and technical background, the second contains the methodological contributions, and the third presents the results.

The first part aims to explore the topic of morphing wings for transport aircraft and to establish the technical background required for the methodological contributions and results that follow. The formal research questions are derived at the end of this part, based on the preceding findings. Chapter 2 reviews the literature on morphing wings for transport aircraft, motivating the scoping and the research gap that were introduced in section 1.1. Chapter 3 introduces the methods used in conceptual aircraft design, and synthesizes how these methods may need to change when applied to aircraft with morphing wings. Chapter 4 discusses aerodynamic solvers and optimization techniques, addressing the trade-off between drag reduction mechanisms identified in chapter 1. Chapter 5 documents numerical estimation methods for the maximum lifting capabilities of airfoils, addressing a gap in conceptual design relationships identified in chapter 3. The research questions are formalized in chapter 6, which closes the first part.

The second part contains the methodological contributions that act as building blocks towards the design and analysis of morphing wing transport aircraft. Because the conceptual design of aircraft with morphing wings is currently underresearched, these methods can be regarded as standalone results that enable future research on the topic. Chapter 7 presents a parametrization method for chordwise 2-DoF camber morphing that minimizes the number of design variables, which is advantageous for the shape optimization of morphing wings. chapter 8 details an aircraft trimmed performance analysis tool. This tool was developed to address the gap identified in Chapter 4, where no suitable aerodynamic analysis tool for the morphed wing shape optimization was found. Finally, chapter 9 documents the sizing methodology and its integration into the Initiator aircraft design toolbox. The integration of the parametrization method from chapter 7 and the trimmed performance analysis tool from chapter 8 within the toolbox is also detailed here.

The third part presents the results. Chapter 10 presents a maximum lift study on morphing airfoils. The need for this study is motivated in chapter 3, and the available methods are discussed in chapter 5. This study sits before the sizing studies in chapter 11 because it generates important inputs to those studies. Chapter 11 presents the block fuel comparison between the reference and morphing wing conceptual aircraft, addressing the main research objective. The conclusion and discussion are presented in chapter 12.

The relationships between the parts and the chapters within them is presented visually in Figure 1.2.

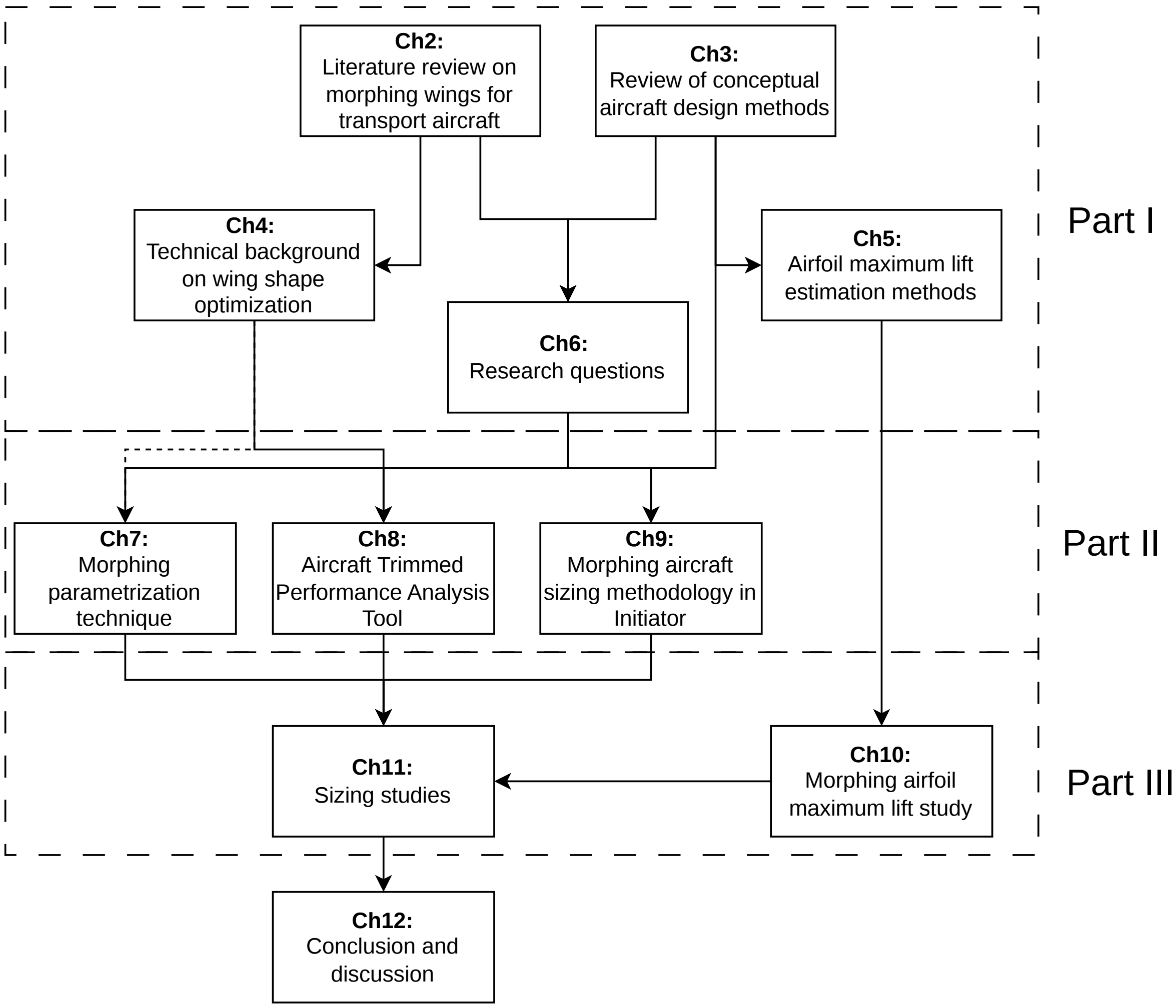

Figure 1.2: Visual representation of the structure of the present thesis

I

Literature Review & technical background

2

Morphing wings: an overview

The present chapter documents the literature review into the topic of morphing wings, providing a background for the scoping decisions made in chapter 1. First, section 2.1 discusses the definitions given in the literature for morphing and the morphing concept under study within them. Following, the mechanisms through which compliant camber-twist morphing wings may reduce aerodynamic drag are discussed in section 2.2, aiming to motivate this research and support the statements made in section 1.1. Finally, section 2.3 will detail current research efforts and outstanding challenges in morphing wing technology, as well as establish the conceptual-design gap this thesis addresses.

2.1. Definitions and classification of morphing wings

The exact definitions given in the literature for morphing in the aeronautical context vary, although the common ground is that morphing wings are shape changing wings. The definitions mostly disagree about what is considered morphing, and what type of structures are associated with it. Weisshaar [9] describes morphing as *"a set of technologies that increase a vehicle's performance by manipulating certain characteristics to better match the vehicle state to the environment and task at hand"*. Following this relatively broad definition, he argues that high-lift devices and retractable landing gear can be classified as morphing devices in a later publication [4]. Concilio *et al.* [3] and Barbarino *et al.* [10] emphasize the association of the technology with smart structures, which are defined as structural architectures with fully integrated devices that give the system additional capabilities to adapt to various instantaneous functions or changes to the external environment while preserving the characteristic of withstanding loads. In line with the association with smart structures, morphing is also associated with exotic, or smart materials. The interest in these materials mainly comes from novel actuation strategies that may help eliminate complex, heavy mechanisms through which morphing may be achieved. Weisshaar [4] argues that identifying morphing with these materials is a viewpoint that is too restrictive. In light of the concept upon which the present study is based, introduced in chapter 1, the association of morphing with smart structures is fitting. The morphing trailing edge can adapt to the external environment while remaining load carrying. Furthermore, the actuators are fully integrated into the wing itself. The association with exotic materials can be seen as too restrictive in this case, as the concept currently does not implement those [6].

2.2. Drag reduction mechanisms

As briefly introduced in chapter 1, compliant camber-twist morphing wings can reduce friction drag, pressure drag, induced drag, and wave drag for aircraft operating in transonic conditions. Furthermore, the two chordwise degrees of freedom of the morphing concept under study allow deformation into reflexed shapes, enabling partial decoupling of the aerodynamic moment and lift generated. This may be used to reduce trim drag.

The label camber-twist morphing suggests two independent mechanisms, but in the concept under study the two are coupled. Spanwise variation in camber morphing produces wing twist, which means that the twist degree of freedom is realized through camber morphing at the section level. Camber is an airfoil property, while the resulting twist distribution acts at the wing level. The drag reduction mechanisms below are organized following this division, starting with the wing-level effects of twist on induced drag and proceeding to the airfoil-level effects of camber on pressure, friction, and wave drag. The trim drag mechanism that is specific to the concept under study is treated separately at the end.

Twist morphing provides control over the spanwise lift distribution of the wing. By shaping this distribution to better resemble the ideal elliptical one, the induced drag generated by the wing can be reduced. The induced drag depends on the lift coefficient, wing aspect ratio, and the Oswald efficiency factor e, as expressed in equation (2.1). The Oswald factor represents the resemblance of the lift distribution to the ideal elliptical distribution. For conventional transport aircraft, it ranges between 0.75 and 0.85 in the design condition [11, 149].

$$C_{D_i} = \frac{C_L^2}{\pi \cdot AR \cdot e} \tag{2.1}$$

Spanwise control over the lift distribution also enables the elimination of conventional discrete control surfaces such as ailerons. The resulting absence of gaps, hinge lines, and other excrescences improves the smoothness of the wing surface. This reduces excrescence drag and, to a small degree, may reduce turbulence over a portion of the wing, lowering skin friction drag.

Camber-twist morphing wings can further reduce induced drag by acting as active aeroelastic wings, which reduce dynamic loads on the wing structure. This allows for a lighter design, which lowers the aircraft weight and thereby the lift coefficient in cruise. The result is a reduction in induced drag through equation (2.1). Active aeroelastic wings are not necessarily morphing wings. An example of an active aeroelastic system based on conventional control surfaces is the Boeing 787, which implements a gust load alleviation systems. Camber-twist morphing wings form a subset of active aeroelastic wings within which load alleviation is achieved through the morphing degrees of freedom.

At the airfoil level, camber morphing provides control over the sectional lift coefficient at a given angle of attack [10, 826]. This control allows the pressure distribution to be optimized, reducing both pressure and friction drag at the section. Additionally, Niu *et al.* [5] showed that trailing edge camber morphing can be used to reduce wave drag in transonic conditions. By varying the trailing edge camber, the position and strength of the shockwave over a supercritical airfoil could be controlled and optimized, reducing wave drag.

The two chordwise degrees of freedom of the concept under study additionally allow deformation into reflexed shapes, which partially decouples the aerodynamic moment from the lift generated. Reflexed shapes reduce the rearward loading on the airfoil sections along the wing, which decreases the nose-down aerodynamic moment generated. This, in turn, lowers the downward load required from the horizontal tail for trim. The lift the main wing has to generate is consequently lower, leading to a further reduction in induced drag through equation (2.1). For conventional transport aircraft, trim drag accounts for between 0.5% and 5% of the total aircraft drag [12].

Considered together, these mechanisms imply that the wing shape for minimum drag at a given flight condition is the outcome of an optimization problem in which several drag components must be balanced. For example, increasing camber to bring the lift distribution closer to elliptical may simultaneously increase the pressure drag at the affected section. This trade-off is a key implication for the present study.

2.3. Status, research & outstanding challenges

This section provides an overview of the status of morphing for transport aircraft, recent research efforts, and outstanding challenges. The status of morphing on in-service aircraft is discussed first. Recent research efforts are then covered along three main lines of work. The first is the use of morphing for high-lift generation. The second is the mechanical design and subsystem investigation of morphing systems. The third is the application of morphing in optimization studies of aircraft performance and structures. The outstanding challenges are folded into the discussion of each line of work.

Compliant morphing surfaces are not seen on the state-of-the-art jet transport aircraft of today. In the narrow-body segment, these are the Airbus 320 Neo family, Boeing 737 Max family, and the Embraer E2 family. In the wide-body segment, they are the Boeing 787 and Airbus 350. The narrow-body examples are all redesigns of airframes that entered service over twenty years ago, namely the Airbus 320 family, Boeing 737NG family, and the Embraer E1 family [13–15]. The newer aircraft are an evolution of the older ones rather than a full redesign, which explains why morphing technologies are not yet seen on them. The wide-body examples were both launched over twenty years ago [13, 14]. At the time these aircraft were first designed, smart materials and structures were not yet at the technology readiness level required for implementation. These aircraft do, however, employ a degree of camber morphing by deflecting control surfaces on the wing based on their cruise condition [16], indicating that manufacturers do see merit in the technology.

The use of morphing in the context of high-lift generation has been investigated in two distinct ways. The first considers camber morphing of distinct flaps, which retain the function of a conventional high-lift device in take-off and landing [17, 18]. The second considers the use of a compliant morphing trailing edge for high-lift generation [19]. Both approaches also cite wing shape optimization in cruise as a key performance benefit, but they differ in the deflections they can achieve. For the distinct flap approach, only the portion of the flap exposed to the flow in the retracted position is able to provide camber morphing functionalities. The fully compliant morphing trailing edge does not have this constraint. Pecora [17] does not present numerical results for the maximum lifting capabilities of the distinct morphing flap. Instead, the high-lift performance of the single-slotted camber morphing flap under study in the article is said to have enhanced high-lift performance compared to a conventional double-slotted flap. Besides the compliant morphing trailing edge, the concept under study by Ameduri *et al.* [19] features a droop nose. Two-dimensional results showed that the achievable sectional lift increment due to leading and trailing edge morphing on a base airfoil that is visually estimated to be a NACA 6 series airfoil is around 0.5. The airfoil and high-lift results are shown in Figure 2.1a and Figure 2.1b respectively.

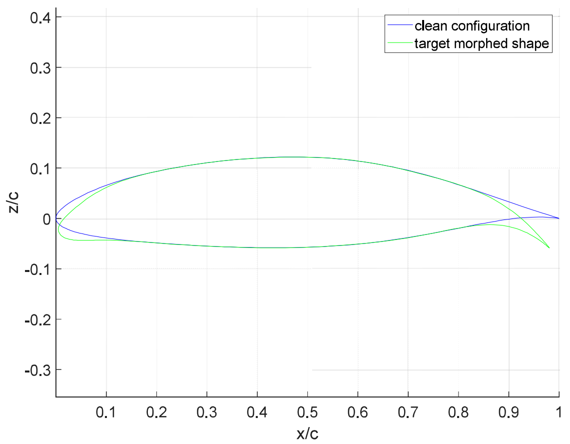

(a) Baseline airfoil and high-lift configuration

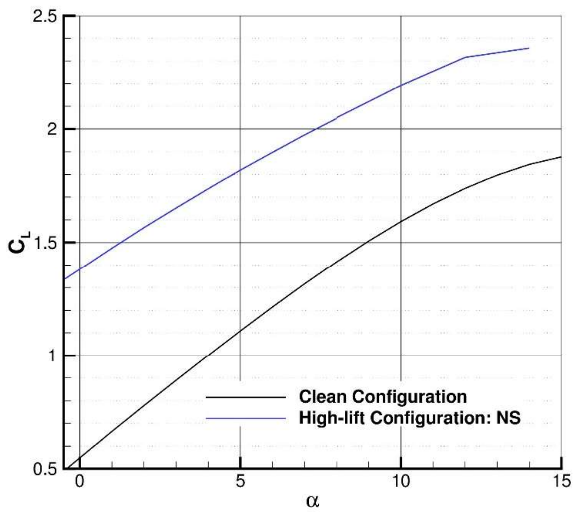

(b) Two-dimensional high-lift results

Figure 2.1: High-lift study by Ameduri *et al.* [19] on a compliant morphing airfoil with a droop nose, evaluated using a RANS based solver

Beyond the aerodynamic results, these studies dedicate significant focus to the mechanical design of the morphing wing, which is the next area of research. Studies within this area focus on the mechanical design, actuation strategies, and aeroelastic interactions of morphing systems [6, 20, 21]. Although the mechanical design of morphing wings is not the focus of the present thesis, these studies are named here because they originate from a key challenge pertaining to compliant morphing wings. This challenge is the paradox of morphing structures, as defined by Concilio *et al.* [3]. Morphing structures should retain the classical function of a structure, which is to carry loads under limited displacement, while being compliant to the desired deformations for morphing. The structural characteristics required to do this are complex, prompting the research into the topic. Barbarino *et al.* [10] mention smart materials and structures as one of the possible solutions to the paradox, which is likely the cause of the term morphing being associated with these materials and structures, as introduced in section 2.1. The complexity of the mechanical design also means that the studies in this area are detailed in nature and focused on the individual concepts under study. This limits the exportability and scalability of results from one study to the other, which is identified as a key bottleneck by Giuliani *et al.* [22].

Wing morphing has also been at the center of a number of optimization studies. These include a cruise performance optimization through variable camber trailing edge flaps (VCTEFs) for an Airbus 320 [23], an aerostructural optimization of a morphing wing for the NASA Common Research Model (CRM) [24], and a design and trajectory optimization of a morphing trailing edge wing on the NASA CRM [25]. The predicted fuel burn benefits reported by these studies are modest. Orlita and Vos [23] finds a fuel burn reduction of only 0.35% over the harmonic range for camber morphing distinct flaps. The small improvement is attributed to conventional wings being highly optimized. The morphing deflections deemed feasible in this study are small in comparison to those possible with the concept under study in this thesis, since only the part of the VCTEF exposed to the flow is able to deform, as illustrated in Figure 2.2. Jasa *et al.* [25] reports fuel burn savings between 0.2% and 0.7% over varying mission ranges, with larger savings on longer missions. This study only considered twist morphing, which means that most of the drag reduction mechanisms introduced in section 2.2 are not utilized.

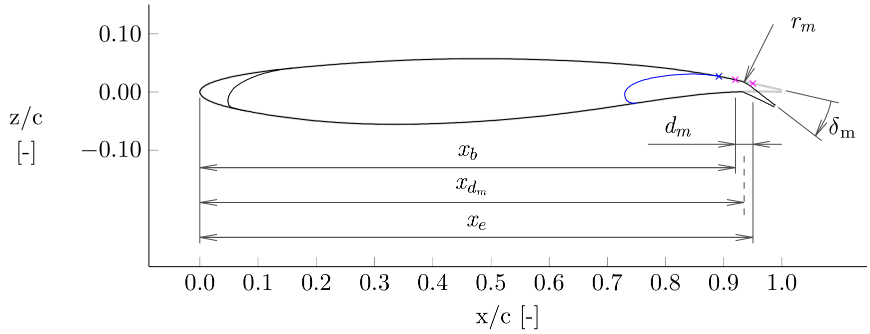

Figure 2.2: Demonstration of morphed upper-flap surface concept by Fokker-GKN, from [23]

The aerostructural optimization study by Fujiwara *et al.* [24] reports a larger benefit. A fuel burn reduction of 5% was found for a morphing trailing edge device along 40% of the trailing edge of the wing of the NASA CRM. This reduction is primarily attributed to the reduction in wing structural weight due to adaptive maneuver load alleviation using the morphing system. A key underlying assumption in this study is that the morphing system does not incur a weight penalty and that all desired morphing shapes can be achieved.

A common denominator in the optimization studies presented above is that the effect of the morphing system on the aircraft sizing is not taken into account, focusing on a fixed reference aircraft geometry. Furthermore, Fujiwara *et al.* [24], Orlita and Vos [23], and Jasa *et al.* [25] all assume no weight penalty due to the morphing system. The aircraft-level consequences of adopting a morphing wing, including the sized wing area, maximum take-off mass, and installed power, remain unaddressed at conceptual design level. This is the gap that the present thesis aims to fill. Without an assessment of the technology at aircraft level, the question of whether camber-twist morphing wings actually have merit for transport aircraft cannot be answered.

3

Conceptual aircraft design

The relevance of conceptual aircraft design to the aircraft level investigation of the viability of 2-DoF morphing trailing edge wings has been laid out in chapter 1. The present chapter therefore provides a background on the conceptual aircraft design process and the estimation methods for the high level parameters that are crucial in generating a valid design. Given the iterative nature of the conceptual design process, automated approaches can significantly improve concept evaluation time. One such program is the Initiator [26], developed at the Faculty of Aerospace Engineering of TU Delft, which forms the basis for the conceptual assessments carried out in this thesis. The design process and relevant methods are presented in section 3.1, and the Initiator is introduced in section 3.2.

3.1. Conceptual design process

The conceptual design process translates a set of design requirements into a coherently sized aircraft configuration, producing important initial estimates for size, weight, and performance. Conceptual design methods are extensively documented by authors like Torenbeek [11], Roskam [27], and Raymer [28]. The focus in this section will be on methods governing parameters that are directly influenced by the aerodynamic and structural characteristics of the wing, such as wing sizing and weight estimation, as these are expected to produce meaningfully different outcomes for morphing wing aircraft compared to conventional designs. Many of the methods presented are reliant on empirical data or previous experience from aircraft that have entered service. The reason for this is the tight coupling of the disciplines aerodynamics, structures, propulsion, and systems in aircraft design [29], meaning changes in any one parameter propagate throughout the entire design. This is best exemplified by the concept of weight growth, also known as the snowball effect. Weight growth is driven by a feedback loop, which is illustrated in Figure 3.1. In the context of this study, it adds to the motivation of carrying out an assessment of morphing wings at conceptual level, ensuring the potential performance benefits are investigated within a converged aircraft design. The methods being reliant on empirical data and previous experience will be put into context later on in this chapter.

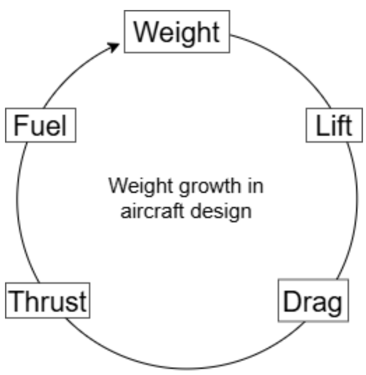

Figure 3.1: Weight growth in aircraft design

A flowchart of the design process, as proposed by Torenbeek [11], is presented in Figure 3.2. The iterative characteristic of the process is evident from the feedback loops in the flowchart. Of the steps shown, the fuselage design, and undercarriage design are not expected to differ significantly from conventional designs and are therefore not treated in detail in the present chapter. Furthermore, a ”rubberized” approach will be taken for the sizing of the engines, and propellers if applicable. Rubberized sizing scales engines to meet the thrust requirements of the aircraft rather than being selected from a fixed catalog of existing powerplants. This approach is not uncommon in aircraft design, and may be necessary due to the long development cycles of aircraft engines [11, 186]. Finally, estimations for noise and operating costs fall outside the scope of this study. The fuel consumption is adopted as the primary measure of economic viability, as it encompasses the trade-off between the sizing effects and aerodynamic effects of morphing wings. Following from this discussion, the methods treated in the remainder of this section are the weight estimation, wing- and thrust-sizing, and drag estimation, as these are the steps most directly governed by the aerodynamic and structural characteristics of the wing.

3.1.1. Class 1 weight estimation

The Class 1 weight estimation is the first step after the determination of the initial concept. The Class 1 weight estimation heavily relies on empirical relationships and experience from existing aircraft. The parameters estimated in this step are the take-off weight W_{TO}, the operating empty weight W_{OE}, and the mission fuel weight W_F for the design mission. First, the take-off weight is broken down into the expression in equation (3.1) [30, 5].

$$W_{TO} = W_{OE} + W_F + W_{PL} \tag{3.1}$$

In the expression above, W_{PL} is the payload weight, which is directly related to the payload in the design requirements. For passenger transport aircraft, an average weight of a person plus baggage is assumed [30, 8]. For the determination of the fuel weight, the fuel weight is first broken down as in expression (3.2), where $W_{F_{used}}$ and $W_{F_{res}}$ are the fuel used throughout the design mission and the reserve fuel respectively. The reserve fuel is often expressed as a fraction of the fuel used or as a required additional range for diverting [30, 9].

$$W_F = W_{F_{used}} + W_{F_{res}} \tag{3.2}$$

The weight of the fuel used throughout the design mission is found using the fuel-fraction method. The mission is broken up into phases like taxi, take-off, climb, cruise, descent, and so on. For each mission phase, the fuel-fraction is the ratio of the weight at the end of that mission phase to the weight at the start of that mission phase [30, 11], as expressed in (3.3).

$$FF_i = \frac{W_{i+1}}{W_i} \tag{3.3}$$

Subsequently, the total fuel fraction for a given mission can be found using equation (3.4).

$$FF_{mission} = \prod_{i=1}^{N} FF_i \tag{3.4}$$

Now, the mission fuel weight can be related to the take-off weight. Given the weight of the aircraft at the start of a mission is the take-off weight W_{TO}, and that the weight at the end of the mission is $W_{TO} - W_{F_{used}}$, the used fuel weight can be expressed as in equation (3.5).

$$W_{F_{used}} = W_{TO}\left(1 - \prod_{i=1}^{N} FF_i\right) \tag{3.5}$$

The fuel fractions for the different mission segments are found analytically or from previous experience. For short mission segments, previous experience is often used. These are mission segments like engine start and warm up, taxi, take-off, and landing [30, 12]. For segments like cruise and loitering, versions

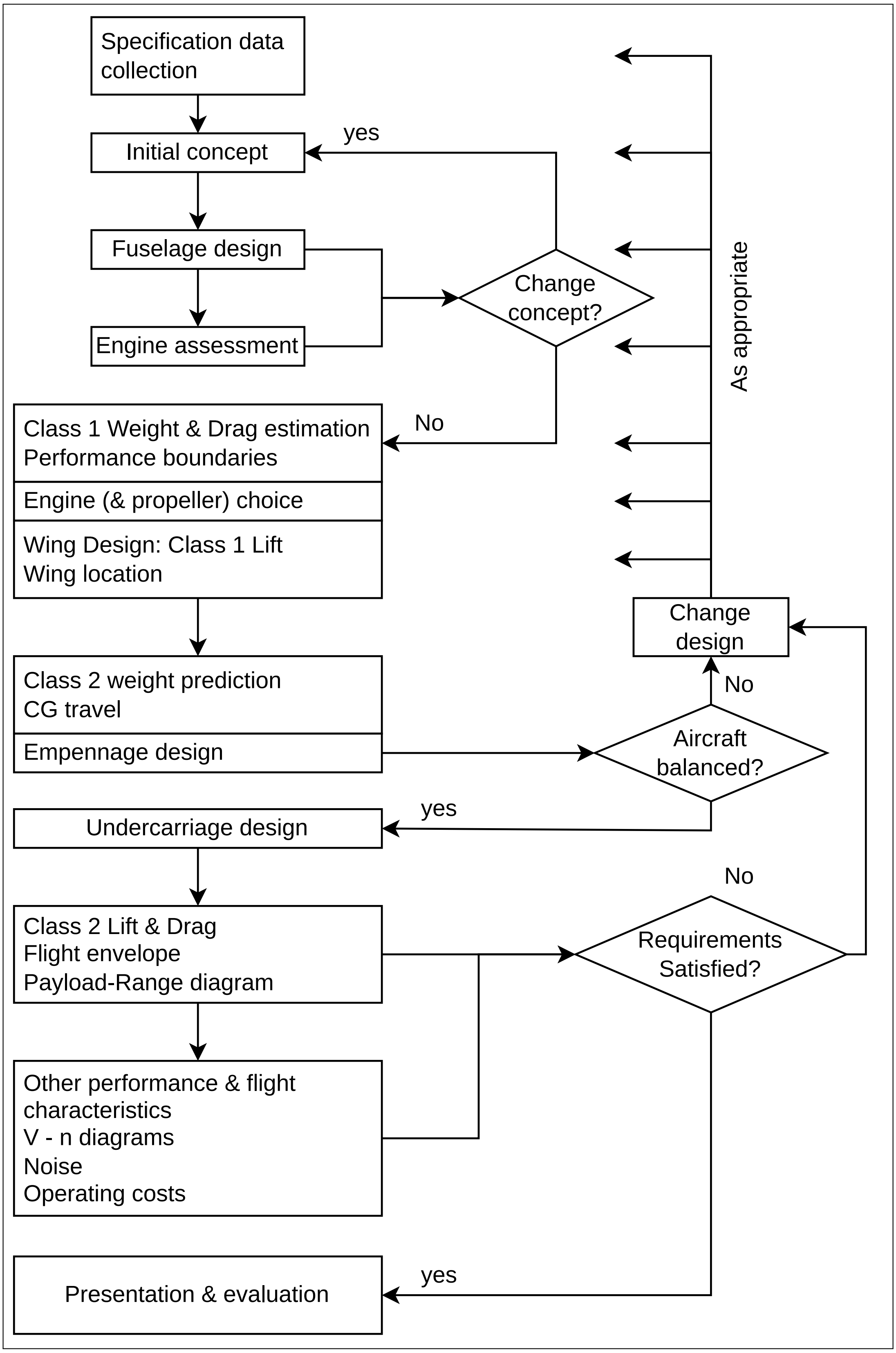

Figure 3.2: Conceptual design process, reproduced from [11]

of the Breguet range equation are used. Equation (3.6) shows the Breguet range equation for jet-powered aircraft, where R_{cr} is the cruise range, V is the cruise speed, $\frac{L}{D}$ is the lift-to-drag ratio, and c_j is the specific fuel consumption, which is a measure of the fuel burned by the engine for a unit thrust [30, 15]. As can be seen in expression (3.6), it provides a relation between the fuel fraction for the cruise phase to the required cruise range.

$$R_{cr} = \left(\frac{V}{c_j}\right)_{cr} \left(\frac{L}{D}\right)_{cr} \ln\left(\frac{W_{end}}{W_{start}}\right) \tag{3.6}$$

The operating empty weight of the aircraft can be further broken down into expression (3.7), where W_E is the empty weight, W_{tfo} is the weight of trapped fuel and oil, and W_{crew} is the crew weight. The required amount of crew members is found from the applicable regulations, which are the CS-25 regulations in the present study. The crew weight is subsequently found using the average weight of a crew member plus baggage, like the payload weight for passenger transport aircraft. W_{tfo} is often expressed as a fraction of the take-off weight, which can be up to 0.5% [30].

$$W_{OE} = W_E + W_{tfo} + W_{crew} \tag{3.7}$$

The empty weight can be related to the take-off weight using empirical relationships. Within various classes of aircraft, there is a linear relation between $\log_{10} W_E$ and $\log_{10} W_{TO}$ tuned with empirical constants. This is shown in equation (3.8), where A and B represent the empirical constants [30, 18].

$$\log_{10} W_{TO} = A + B \log_{10} W_E \tag{3.8}$$

When the established relationships are substituted in equation (3.1), equation (3.9) is obtained, which can be solved for the take-off weight.

$$W_{TO} = 10^{\frac{\log_{10} W_{TO} - A}{B}} + M_{tfo} W_{TO} + W_{crew} + W_{TO}\left(1 - \prod_{i=1}^{N} FF_i\right) + W_{PL} \tag{3.9}$$

The substantial reliance of the take-off weight estimation on empirical data has a number of implications on the applicability to the take-off weight sizing of aircraft with morphing wings. Given that no transport aircraft with morphing wings have been built or entered service, there is no data available on the weight of such aircraft. Hence, care needs to be taken when applying the empirical relationship between empty weight and take-off weight in equation (3.8). Correction factors exist for new technologies [30, 48], such as composite structures, but the lack of empirical data means that there is no validated correction factor for the weight of morphing wings. Furthermore, as discussed in chapter 1, morphing wings could reduce the weight of the wing structure by acting as active aeroelastic wings, creating another discrepancy in the weight prediction. An important desired outcome of this study, however, is the sensitivity of the design to the characteristics of morphing wings. Hence, the aforementioned uncertainties will be taken into account as parameters.

The use of the Breguet range equation in expression (3.6) also has implications when applied in the design of aircraft with morphing wings. As morphing wings can change shape in flight, there is no singular value for the aerodynamic efficiency in cruise. Technically, there is an optimum wing shape, in terms of the lift-to-drag ratio, for every flight condition the aircraft may encounter. The deformations applied to the wing are therefore part of an optimization problem. Note, however, that the Breguet range equation assumes a constant lift-to-drag ratio, also when applied to conventional aircraft. For this to be true, the aircraft would have to be climbing into thinner air continuously, which never exactly holds.

As the Class 1 estimation methods are applied at the earliest stage of the conceptual design process, limited geometric data is available, meaning higher-fidelity physics-based weight estimations can not be applied yet. The Class 1 weight estimation is therefore a necessary step in obtaining first estimates for the size of various components. The iterative nature of the conceptual design process is expected to correct any discrepancies introduced by the statistical weight estimation as the design converges.

3.1.2. Wing area and thrust sizing

The next step in the conceptual design process is the sizing of the wing area, and thrust or power. The estimation of these parameters is subject to numerous constraints. In this step, values for the wing loading, $\frac{W}{S}$, and the thrust loading or power loading, $\frac{T}{W}$ and $\frac{W}{P}$ respectively, are selected that satisfy all these constraints. The combination of these parameters yields the design point. Typically, the constraints are presented graphically in a wing-thrust loading diagram, of which an example is shown in Figure 3.3. The present section aims to synthesize how the constraint boundaries shift due to the implementation of morphing wings. As morphing primarily affects the aerodynamic characteristics of the wing, the constraint boundaries are most likely to change in the wing loading values. To keep the information provided aligned with the goal of this section, the relations presented will primarily be for jet aircraft. This is deemed sufficient as the wing sizing of propeller powered and jet powered aircraft is influenced by morphing wings in a similar manner.

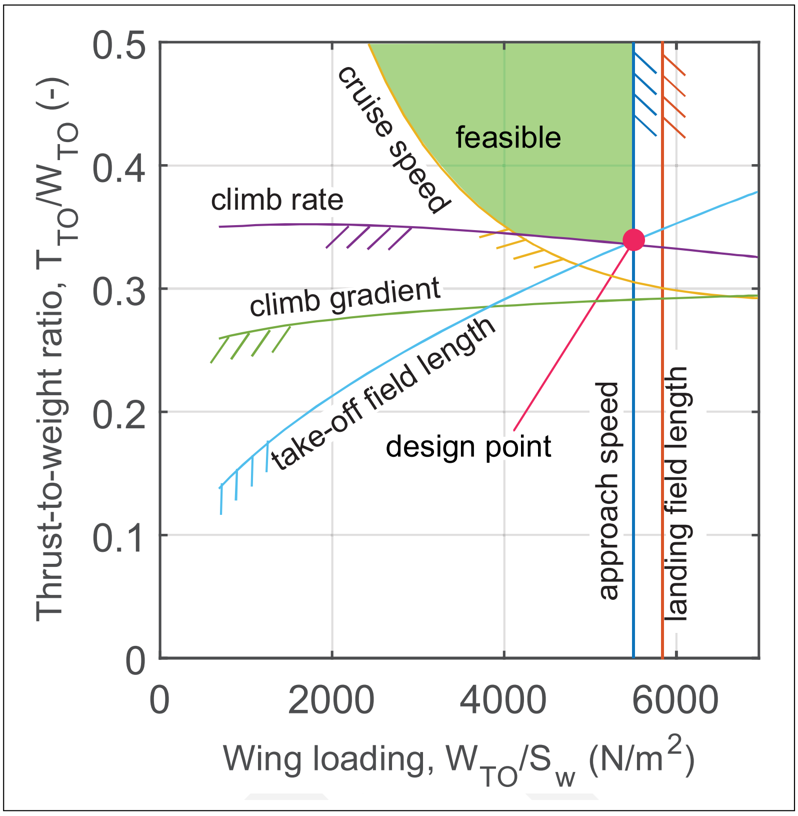

Figure 3.3: Example of a wing-thrust loading diagram [31]

Sizing for take-off requirements

The take-off field length for CS-25 aircraft is the distance taken by an aircraft to reach an altitude of 35 feet, or 10.7 m, at the lift-off speed V_{LOF}, from standstill. It is dependent on the take-off weight, thrust-to-weight ratio or power-to-weight ratio, aerodynamic drag, and rolling friction from the ground [30, 94]. The lift-off speed itself is dependent on the take-off weight, the lift coefficient in take-off configuration, and the altitude at which the aircraft takes off. The required take-off field length, given in the specification data, determines the airport class which the aircraft can perform its design mission from.

The take-off field length is proportional to the take-off parameter, TOP, of which the version for jet powered aircraft is shown in equation (3.10). In this expression, σ is the ratio of air density at the airfield of interest to the sea-level ISA density of $1.225\,\mathrm{kg\,m^{-3}}$.

$$TOP = \frac{W/S}{\sigma C_{L_{max_{TO}}} T/W} \tag{3.10}$$

The proportionality factor between the take-off field length and the take-off parameter is empirically determined and depends on the aircraft class, as illustrated in Figure 3.4.

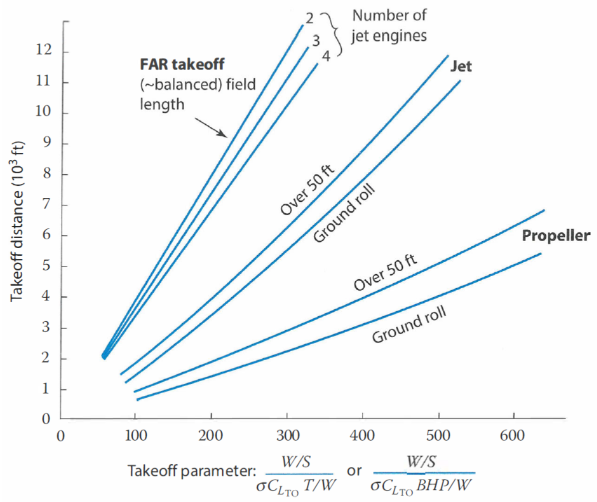

Figure 3.4: Relation between take-off parameter and take-off field length in fps units [28, 130]

At this stage in the design process, values from previous experience are used for $C_{L_{max_{TO}}}$. This has a significant implication on the present study. The replacement, partial or entirely, of conventional trailing edge high lift devices with a compliant morphing trailing edge means that these values can not be readily applied.

Sizing for landing requirements

The landing field length in context of the applicable regulations is defined as the total landing distance divided by a factor of 0.6. This is a safety factor to account for differences in pilot technique. The total landing distance consists of an airborne part, and a ground-based deceleration phase. In the regulations, the landing distance is defined as the horizontal distance required by an aircraft to descend from an altitude of 50 feet, or $15.24\,\mathrm{m}$, touch down, and decelerate to a standstill. Through linear regression of values from experience with existing aircraft, the landing field length in feet is related to the approach speed in knots through the relation shown in equation (3.11). The approach speed is defined as 1.3 times the stall speed in landing configuration [30, 111].

$$S_{FL} = 0.3V_A^2 \tag{3.11}$$

Through the relation between the landing field length to the approach speed, and the relation between the approach speed and the stall speed in landing, the landing field length can be related to the maximum lift coefficient in landing configuration as shown in the expression below.

$$S_{FL} = 0.3(1.3V_{s_L})^2 = 0.507V_{s_L}^2 \tag{3.12}$$

The landing field length can now be related to the wing loading and maximum lift coefficient in landing configuration through equations (3.13) and (3.14).

$$W_L = \frac{1}{2}\rho V_{s_L}^2 S C_{L_{max_L}} \rightarrow V_{s_L} = \sqrt{\frac{2}{\rho C_{L_{max_L}}}\frac{W_L}{S}} \tag{3.13}$$

$$S_{FL} = \frac{1.014}{\rho C_{L_{max_L}}}\frac{W_L}{S} \tag{3.14}$$

In equation (3.14), the landing field length is related to the wing loading during landing. To create a consistent wing-thrust sizing diagram, like in Figure 3.3, the wing loading during landing has to be related to the wing loading at the maximum take-off weight. Roskam [30, 107] presents a number of typical values for the ratio of landing weight to take-off weight for various classes of aircraft. One could also subtract the value for the weight of the fuel used for the design mission, as found in the Class 1 weight estimation, from the take-off weight to find the landing weight. Equation (3.15) presents the final expression relating the landing field length to the wing loading during take-off, and the maximum lift coefficient in landing configuration.

$$S_{FL} = \frac{1.014}{\rho C_{L_{max_L}}} \frac{W_{TO}}{S} \frac{W_L}{W_{TO}} \tag{3.15}$$

Unlike the take-off field length, the landing field length is not dependent on the thrust-, or power-loading. The similarity between the two lies in the dependence on the maximum lift coefficient in the respective configurations. As for the take-off sizing, replacing conventional high-lift devices with compliant morphing trailing edges has implications for the landing performance. This will be put into further context at the end of this chapter.

Sizing for climb gradient requirements

In the applicable regulations, multiple conditions in which an aircraft must meet certain climb gradient requirements are given. At first, these are divided over two critical flight phases: take-off and aborted landings. They are subsequently divided over a number of aircraft configurations. These configurations specify whether the landing gear is retracted or not, the velocity, altitude, and weight of the aircraft, the position of the high-lift devices, and the atmospheric conditions [30, 141]. An enumeration of the requirements and the conditions under which they must be met falls outside the scope of the present section. Instead, the focus is on the methodology used in assessing the climb performance of the aircraft. To size the climb performance of an aircraft, an estimate for the drag polar is required. For low-speed conditions, a parabolic drag polar, shown in equation (3.16), can be assumed [30, 118].

$$C_D = C_{D_0} + \frac{C_L^2}{\pi A e} \tag{3.16}$$

The term C_{D_0} in the expression above is the zero-lift drag, or lift-independent drag. This term can be expressed as the ratio of the equivalent parasite area, f to the wing area S, as shown in equation (3.17).

$$C_{D_0} = \frac{f}{S} \tag{3.17}$$

Through linear regression in logarithmic space, the equivalent parasite area can be related to the aircraft wetted area, which can subsequently be related to the take-off weight, as show in equations (3.18) and (3.19). The constants a, b, c, and d are determined empirically [30, 121].

$$\log_{10} f = a + b \log_{10} S_{wet} \tag{3.18}$$

$$\log_{10} S_{wet} = c + d \log_{10} W_{TO} \tag{3.19}$$

For the deployment of high-lift devices and for the landing gear in take-off and landing configuration, correction factors for the zero-lift drag coefficient and for the Oswald efficiency factor are given [30, 127]. With these factors, the drag polar of the aircraft in the respective conditions can be constructed.

The requirements are specified in climb gradients. The climb gradient (CGR) is equal to the sine of the flight path angle γ. Given that the climb gradients required are small, the small angle approximation is used. The climb gradient can subsequently be found for All-Engines-Operative (AEO) and One-Engine-Inoperative (OEI) conditions using equations (3.20) and (3.21) respectively. In the latter, the parameter N represents the number of engines on the aircraft.

$$\frac{T}{W} = \frac{C_D}{C_L} + CGR \tag{3.20}$$

$$\frac{T}{W} = \frac{N}{N-1}\left(\frac{C_D}{C_L} + CGR\right) \tag{3.21}$$

The final step composes of relating the lift coefficient and drag coefficient in the expressions above to the aircraft weight. Using the small angle approximation, the required lift can be related to the weight by realizing $L = W \cos\gamma \approx W$. Now the lift coefficient can be found, which can be used in expression (3.16) to find the drag.

Given the requirements apply in take-off and landing configurations, the effect of the high-lift devices on the zero-lift drag and the Oswald efficiency factor must be taken into account. As discussed, Roskam [30, 127] presents first estimates for correction factors to be applied to these parameters for various aircraft classes. Like for the sizing to take-off and landing requirements, however, the replacement of conventional high-lift devices with compliant morphing trailing edges means that the applicability of these correction factors must be assessed. Of the conventional high-lift devices, morphing trailing edges are most similar to plain flaps, as these both produce single-element high-lift configurations. Plain flaps generate a larger increase in drag than multi-element high-lift configurations for the same increase in lift coefficient [30, 127]. The Oswald efficiency factor may improve with the use of compliant morphing trailing edges, as the spanwise discontinuities on the wing from deflected high-lift devices may be reduced in severity.

Sizing for time-to-climb and ceiling requirements

The time-to-climb requirements and ceiling requirements are usually given in the initial specification for the aircraft. Both are related to the climb rate, where the ceiling is defined as the altitude at which the climb rate becomes zero. The instantaneous climb rate of an aircraft is given by equation (3.22) [30, 152].

$$ROC = V \sin\gamma = V\left(\frac{T}{W} - \frac{C_D}{C_L}\right) \tag{3.22}$$

The equation above shows that, in order to maximize the climb rate, the lift-to-drag ratio should be maximized. As morphing wings are expected to improve the lift-to-drag ratio relative to conventional designs, the climb rate requirement is anticipated to be less stringent for morphing wing aircraft than for their conventional counterparts. To keep the information provided in this section aligned with the effect of morphing wings on the wing area and thrust sizing, this requirement will not be further detailed.

Sizing for cruise speed requirements

The cruise speed requirement is usually given as a combination of a cruise Mach number at a certain cruise altitude. In steady, level, and straight flight, the required thrust can be found by setting it equal to the drag, as in equation (3.23).

$$T_{req} = D = \frac{1}{2}\rho V^2 S C_D \tag{3.23}$$

For the determination of C_D in the expression above at Mach numbers where compressibility effects are not negligible, a correction to the zero-lift drag in the parabolic drag polar is proposed. With this correction, equation (3.23) can now be rewritten to equation (3.24), relating the thrust-to-weight ratio to the wing loading in cruise. In this equation q is the dynamic pressure, given by $q = \frac{1}{2}\rho V^2$ [30, 167].

$$\frac{T_{req}}{W} = q C_{D_0}\frac{S}{W} + \frac{W}{qS\pi Ae} \tag{3.24}$$

The equation above shows that the zero-lift drag is dependent on the inverse of the wing loading, while the lift-induced part of the drag is dependent on the wing loading itself. For a given dynamic pressure and weight, larger wings are operating at a lower C_L, reducing the lift-induced part of the drag. However, they also have a larger surface area, increasing lift-independent drag components.

Conclusion on design point selection

The present section has shown that the sizing of the wing is subject to numerous assumptions. Some of these cannot be readily applied to morphing wing aircraft, such as the values for the maximum lift coefficient in take-off and landing configuration. It will therefore be necessary to obtain a motivated estimate for the performance of compliant morphing trailing edge wings in high-lift configuration. This estimation is further detailed in subsection 3.1.3. Most likely, the achievable maximum lift coefficients of compliant morphing trailing edge wings are lower than that of wings with conventional slotted high-lift devices. When subjected to the same requirements, this will result in larger wing areas being required to meet take-off and landing distance constraints. This has implications on the sizing of the wing for cruise performance. The benefits of morphing wings in terms of aerodynamic efficiency must therefore be weighed against the required wing size.

3.1.3. High-lift system sizing

The present section will detail a Class 1 method for the sizing of the high-lift system. Normally, this method relates the maximum lift coefficient of the wing in take-off and landing configuration to required sectional lift increases on the wing. When performed in reverse, however, sectional maximum lift properties of morphing wing sections can be translated to the maximum lifting capabilities of morphing wings. The procedure will first be described as presented in literature, followed by the application and required parameters for performing it in reverse. An important note for the method presented is that it is valid for wings with sweep angles up to $\pm 35°$ [32, 167].

Three key parameters form the basis of this method. These are the maximum lift coefficients in clean, take-off, and landing configuration; $C_{L_{max}}$, $C_{L_{max_{TO}}}$, and $C_{L_{max_L}}$ respectively. In the selection of the design point, as described in subsection 3.1.2, values for these parameters have been selected. These must now be used for consistency. First, the maximum lift coefficient in clean configuration must be verified. According to Roskam [30, 168], the maximum lift coefficient of the wing should be between 1.05 and 1.1 times the maximum lift coefficient of the overall aircraft. This factor is introduced to account for negative lift on the horizontal stabilizers for the aircraft to be in a trimmed state. He also presents a rapid method for verifying the maximum lift coefficient of the wing in clean configuration. However, as more accurate methods are available as part of the Initiator, which will be detailed in section 3.2, the rapid method will not be detailed here. After the verification of the clean maximum lift coefficient, the required increments in maximum lift coefficient for the take-off and landing configuration can be found according to equations (3.25) and (3.26) respectively. The factors 1.05 account for the additional negative load on the horizontal tail required for trim.

$$\Delta C_{L_{max_{TO}}} = 1.05 \left(C_{L_{max_{TO}}} - C_{L_{max}} \right) \tag{3.25}$$

$$\Delta C_{L_{max_L}} = 1.05 \left(C_{L_{max_L}} - C_{L_{max}} \right) \tag{3.26}$$

The required increases in maximum lift coefficient computed are subsequently related to two-dimensional airfoil maximum lift coefficients through equation (3.27) [30, 170]. The fraction $\frac{S}{S_{wf}}$ represents the ratio of the wing area to the flapped area, which is visualized in Figure 3.5. The term on the right in equation (3.27) is a correction factor for the quarter-chord sweep angle $\Lambda_{c/4}$

$$\Delta C_{l_{max}} = \Delta C_{L_{max}} \frac{S}{S_{wf}} \frac{1}{\left(1 - 0.08 \cos^2 \Lambda_{c/4}\right) \cos^{\frac{3}{4}} \Lambda_{c/4}} \tag{3.27}$$

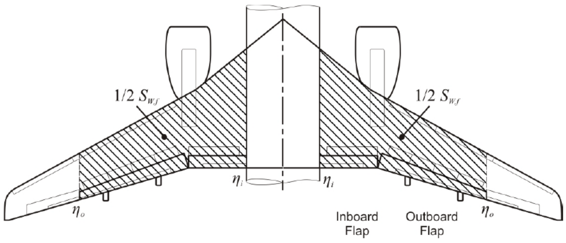

Figure 3.5: Definition of flapped area [33]

The reason for relating the wing maximum lift coefficient increase to two-dimensional values is that the effect of high-lift devices can be generalized more easily in airfoil space. Conceptual relationships exist for determining the sectional lift coefficient increase due to trailing edge high-lift devices based on the type of device, flap-to-chord ratio, and deflection angle. The relationship for plain flaps is shown in equation (3.28) [32, 171]. In this relationship, ΔC_l represents the lift coefficient increase at $0°$ angle of attack, and $\Delta C_{l_{max}}$ represents the maximum lift coefficient increase. The parameters $C_{l_{\delta_f}}$, K, and K' can be found from graphs presented by Roskam [32].

$$\Delta C_l = C_{l_{\delta_f}} \delta_f K' = \frac{\Delta C_{l_{max}}}{K} \tag{3.28}$$

The effect of leading edge high-lift devices in airfoil space can be found according to equation (3.29) [32, 175]. The definition of the chord with the leading edge device extended, c'', is shown in Figure 3.6.

$$\left(C_{l_{max}}\right)_{with\ LE\ device} = \left(C_{l_{max}}\right)_{no\ LE\ device} \frac{c''}{c} \tag{3.29}$$

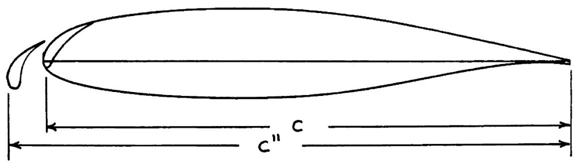

Figure 3.6: Definition of c'' [32, 174]

By reversing the order of the method detailed in this section, it is possible to convert the sectional maximum lift coefficients of morphing aircraft to a motivated estimate for the maximum lift coefficient of compliant morphing trailing edge wings. There is limited literature available on the topic of high-lift performance of morphing trailing edge airfoils [34, 35]. Aside from that, the exportability bottleneck introduced in chapter 1 applies here as well. Because the shapes that can be generated by morphing airfoils are endless in theory, it is less straightforward to define a lift coefficient increase as a function of the flap-to-chord ratio and the flap deflection. Therefore, the present study will cover an investigation into the performance of two-degree-of-freedom camber morphing airfoils in high-lift configuration.

3.1.4. Class 2 weight estimation

After the sizing of the wing and propulsion system, as described in subsection 3.1.2, a first estimate of the aircraft's geometry can be made. The weight of various components can now be estimated based on their geometry, offering more accuracy than the Class 1 method discussed in subsection 3.1.1. The present section will illustrate the Class 2 approach to weight estimation, and the assumptions made in the process, along with their application to aircraft with morphing wings. The preliminary details taken into account are listed below [36, 25].

1. Take-off gross weight
2. Wing and empennage design parameters
3. Limit or ultimate load factor

4. Design cruise and/or dive speed
5. Fuselage configuration
6. Powerplant installation
7. Landing gear design and location
8. Requirements on systems
9. Preliminary structural architecture

At its basis, the Class 2 weight estimation uses the same breakdown of the take-off weight as the Class 1 weight estimation [36, 26], namely:

$$W_{TO} = W_{OE} + W_F + W_{PL} = W_E + W_{crew} + W_{tfo} + W_F + W_{PL} \tag{3.30}$$

Instead of relating the empty weight to the take-off weight through an empirical relationship, the Class 2 weight estimation focuses on estimating geometry and/or requirements informed estimates for component weights. The empty weight W_E in equation (3.30) is broken down further into three components, as shown in equation (3.31). The components are the structural weight, weight of the powerplant(s), and the systems weight, also referred to as fixed equipment weight [36, 26].

$$W_E = W_{struct} + W_{pwr} + W_{syst} \tag{3.31}$$

In order to estimate the structural weight of the aircraft, a preliminary value for the loads on the structure must first be determined. The loads are expressed in terms of the load factor n, which is defined as the ratio of the overall lift to the aircraft weight. To determine the applicable load factors, use is made of the V-n diagram. Distinction is made between maneuvering loads and gust loads. The maneuvering diagram and the gust diagram are shown in Figure 3.7a and Figure 3.7b respectively.

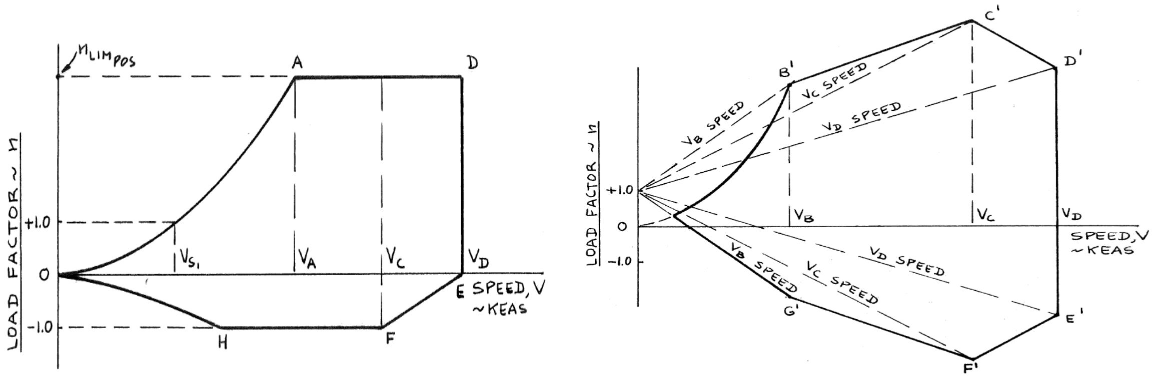

(a) Maneuvering diagram

(b) Gust diagram

Figure 3.7: Maneuvering and gust loading diagrams for CS-25 aircraft [36, 36]

The diagrams above show five key velocities, V_{S_1}, and V_A through V_D. The first is the 1-g stall speed, which is the minimum steady flight speed. The latter four are the design maneuvering speed, design speed for maximum gust intensity, design cruise speed, and design dive speed respectively. The values of these characteristic speeds are determined according to definitions in the relevant regulations. The maneuvering diagram contains the relationship between load factor and velocity by maneuvers carried out by the pilots. These are maneuvers such as a pull up, or a sustained turn. The curved lines connecting the origin of the diagram with points A and H are defined by the maximum lift coefficient. In the regime below V_A, the aircraft will stall before the positive limit load factor n_{lim_+} is reached. This relieves the load on the airframe, meaning it cannot be overstressed by maneuvers below V_A. The value of the positive limit load factor is subject to constraints in the regulations as well. These define a hard minimum, a minimum depending on the take-off weight, and a value that need not be exceeded. Aircraft designers do retain some freedom in selecting this value within the bounds of the regulations.

The dashed lines in Figure 3.7b, labeled V_B speed through V_D speed, represent characteristic vertical gust velocities that induce loads on the aircraft through a change in angle of attack seen by the wing, altering the magnitude of the lift. The gust velocities are defined in relevant regulations. The load factor due to gusts is calculated according to equation (3.32), in which K_g is given by expression (3.33). The factor mu_g in (3.33) is given by equation (3.34) [36, 34].

$$n_{lim} = 1 + \frac{K_g U_{de} V C_{l\alpha}}{498 W/S} \tag{3.32}$$

$$K_g = \frac{0.88\mu_g}{5.3 + \mu_g} \tag{3.33}$$

$$\mu_g = \frac{2W/S}{\rho \bar{c} g C_{l\alpha}} \tag{3.34}$$

Ultimately, the maneuvering and gust load diagram are overlaid, yielding the design limit, and design ultimate load factor which are subsequently used as input to the weight estimations of the aircraft's components. As discussed at the beginning of this subsection, the class 2 weight estimation accounts for the geometric characteristics of various parts. This will be exemplified with the estimation of the wing structural weight. Torenbeek [11, 451-455] proposes the division shown in equation (3.35). In this expression, $W_{W_{basic}}$ is the weight of the wing group without the high-lift devices and spoilers, which are added through the terms W_{hld} and W_{sp} respectively.

$$W_W = W_{W_{basic}} + 1.2\left(W_{hld} + W_{sp}\right) \tag{3.35}$$

To indicate the empirical nature of the relations used in the Class 2 weight estimation, the basic weight of the wing group is presented in expression (3.36). Key geometric and operational parameters in this equation are the wing span b, half-chord sweep angle $\Lambda_{1/2}$, the thickness-to-chord ratio at the wing root $(t/c)_r$, and the ultimate load factor n_{ult}, found using the V-n diagram. The k terms in the expression are correction factors for various design decisions and requirements. A full definition of these terms is provided by Torenbeek [11, 451-455].

$$\begin{aligned} W_{W_{basic}} = 8.94 \times 10^{-4} \times k_{no} k_\lambda k_e k_{uc} k_{st} \times \left[k_b n_{ult}\left(W_{des} - 0.8 W_W\right)\right]^{0.55} \times \\ b^{1.675} (t/c)_r^{-0.45} \left(\cos\Lambda_{1/2}\right)^{-1.325} \end{aligned} \tag{3.36}$$

The relations governing the weight estimation of remaining components follow the same empirical structure as the expression above and will not be further detailed here. The basic wing structural weight estimation has been presented as a representative example, illustrating the dependence on key system characteristics as well as its reliance on previous experience. A number of considerations are to be made in applying the relations to morphing wing aircraft, which shall now be discussed. As presented in chapter 1, camber- and twist-morphing wings can be employed to reduce maneuvering and gust loads on the airframe. A study by Fujiwara *et al.* [24] showed that an 11.8% wing structural weight reduction could be achieved on the NASA CRM[1] by employing morphing to shift maneuvering loads inwards, reducing the bending moment at the wing root. This is illustrated in Figure 3.8.

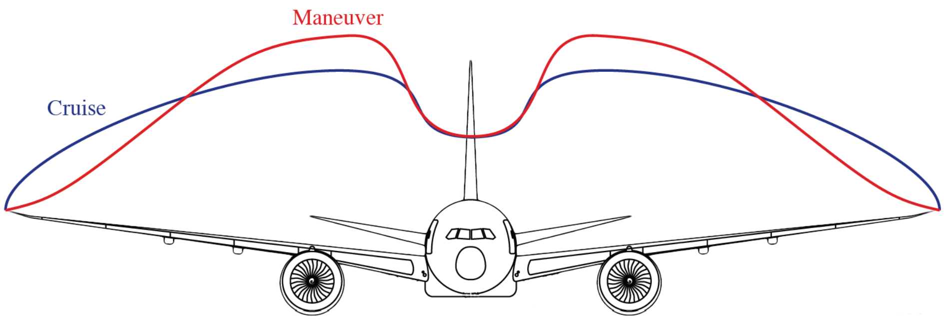

Figure 3.8: Maneuvering load redistribution for wing structural weight reduction [16]

[1]NASA Common Research Model https://commonresearchmodel.larc.nasa.gov/

Upon examination of equation (3.36), the shape of the lift distribution is not taken into account in the wing group weight estimation. The only load-related parameter influencing the wing weight in this equation is the ultimate load factor n_{ult}. The relations in the Class 2 weight estimation do not reflect the full capabilities of morphing wings, as they have been empirically derived from experience with conventional-wing-aircraft. There are physics-based estimation tools available in the Initiator, which will be detailed in section 3.2. These are called Class 2.5 methods as they combine first-principles-based calculations with empirical relations. They could offer a solution to the challenge described above, but do require more input such as the load distribution on the wing, material choice, and preliminary structural layout. Aside from the applicability of Class 2 methods on morphing wings, data on the weight of full-scale morphing wings for transport aircraft is lacking, given that they have not yet been implemented in practice. The approach adopted to mitigate this is to treat the weight of the morphing system as a parameter which can be used to investigate the sensitivity of the design results and fuel consumption to this system weight. A similar approach for the effect of morphing wings on the basic structural weight of the aircraft will be taken, as this provides boundary conditions for future studies, indicating when morphing wings would be economically viable.

3.2. Initiator

The Initiator is a conceptual aircraft design tool that has been in development at the Faculty of Aerospace Engineering of Delft University of Technology since 2014 [26]. The Initiator automates conceptual aircraft design by implementing the sizing and analysis steps that make it up digitally, making use of the iterative nature of the process. The inputs to the program consist of top-level requirements and aircraft configuration settings. These are converted to a coherently sized aircraft design through a workflow called '*convergeWeights*'. A graphical interpretation of this workflow is shown in Figure 3.9. An additional advantage of automation is that physics-based analysis methods may be integrated in the workflow automatically. In Figure 3.9 for example, the 'aerodynamic analysis' block employs AVL[2] at an early stage for performance estimation, reducing the reliance on empirical data.

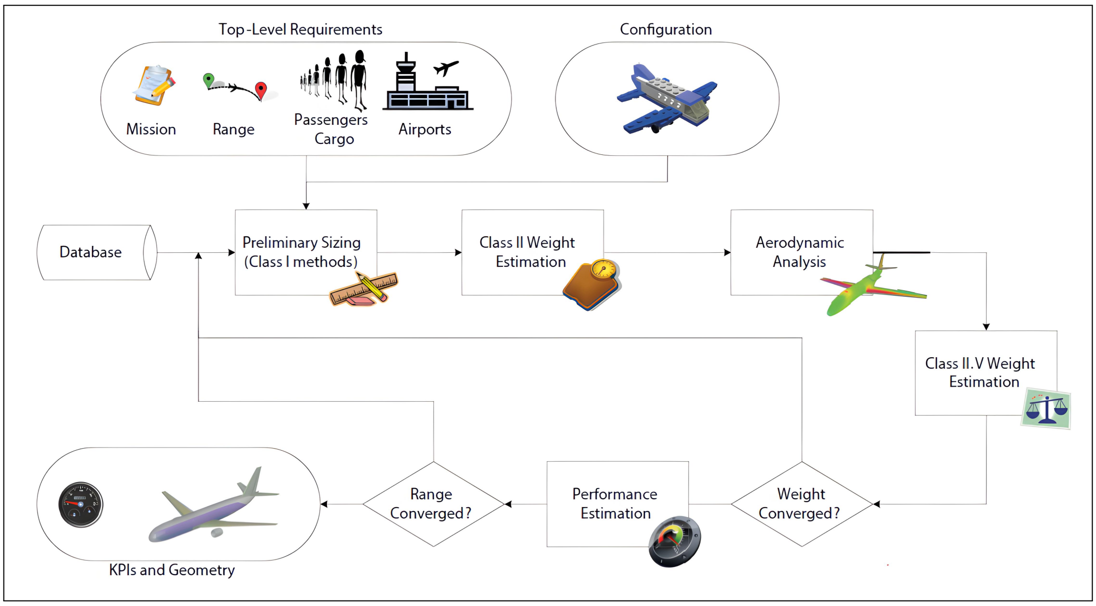

Figure 3.9: Abstract overview of the Initiator '*convergeWeights*' workflow [26, 15]

Elmendorp [26] verified the original implementation of the Initiator by comparing high-level design parameters of resulting aircraft designs to those of the aircraft they were based on. One of these comparisons is shown in Table 3.1, for which the Airbus 320-200 is the reference aircraft. Most parameters match well, with a notable exception in those for the engine pods. Since the initial version, however, more accurate engine modeling has been integrated in the Initiator [37]. Furthermore, the horizontal

[2] https://web.mit.edu/drela/Public/web/avl/, accessed: 08-06-2025

tail area was significantly under-predicted in the original implementation. Since then, however, a more sophisticated, physics based horizontal stability estimation module has been implemented. Key for the present study is that the parameters for the main wing match reality closely. Outside of this, Elmendorp [26] demonstrated that the prediction accuracy for the maximum take-off mass of the A320-200 was within 5%.

Table 3.1: Verification of Initiator results for Airbus 320-200, reproduced from [26, 35]

Dimension	Description	Unit	Reference	Initiator	Error [%]
Wing					
S	Planform area	m^2	122.4	122.8	$+0.33\%$
b	Wingspan	m	33.9	34.1	$+0.59\%$
λ	Taper ratio	-	0.25	0.21	-16%
$\Lambda_{0.25c}$	quarter-chord sweep angle	deg	25	24.5	-2%
Fuselage					
L_f	Length	m	37.6	40.7	$+8.24\%$
D_f	Diameter	m	4.1	4.2	$+2.4\%$
Horizontal Tail					
S	Planform area	m^2	31.0	26.0	-16.13%
b	Wingspan	m	12.5	11.5	-8%
λ	Taper ratio	-	0.33	0.35	$+6.06\%$
$\Lambda_{0.25c}$	Quarter-chord sweep angle	deg	28.0	27.4	$+2.19\%$
Engine pods					
L_e	Length	m	4.4	2.9	-34.1%
D_e	Diameter	m	2.4	1.8	-25%
η_e	Spanwise position	-	34.0	35.0	$+2.9\%$

The motivation for using the Initiator over other conceptual aircraft design tools like DLR's openAD [38], is the availability of the source code of the Initiator, meaning it can be adapted to allow the sizing of aircraft with morphing wings. The required adaptations flow down from the observations made in the present chapter. For clarity, a summary of these observations will be presented in section 3.3.

3.3. Summary on conceptual aircraft design

The present chapter has primarily shown that conceptual aircraft design is substantially reliant on previous experience. This is necessary due to the limited information available at the start of the design process. This does, however, mean that the applicability of these methods to aircraft that incorporate revolutionary technologies can not be assumed. subsection 3.1.1 and subsection 3.1.4 discussed the uncertainty in weight estimation introduced by compliant morphing trailing edge wings. The uncertainty stems from the lack of data on the weight of full-scale morphing wings for transport aircraft, the effect of implementing morphing wings on the sizing of various aircraft parts, and the effect of morphing wings on the fuel consumption of the aircraft. Regarding the fuel consumption, it became clear that the deformed shape of a morphing wing is an optimization problem with the lift-to-drag ratio as an objective function. Furthermore, subsection 3.1.2 showed that the performance of compliant morphing trailing edge wings in take-off and landing configuration has a significant impact on the wing sizing, necessitating an investigation into the high-lift performance of these wings.

To summarize, the optimization problem introduced by morphing wings requires an aerodynamic analysis tool that resolves the key effects of compliant morphing trailing edge wings, as introduced in chapter 1, while remaining computationally efficient for the use in optimization loops. Both solvers and optimization techniques that may be considered for this will be introduced in chapter 4. An estimation of the high-lift performance is likely to require high-fidelity aerodynamic analysis methods. These will be introduced in chapter 5.

4

Wing shape optimization

The present chapter will provide a review of aerodynamic solvers and optimization techniques that may be used in optimizing the deformed shapes of morphing wings. The aerodynamic solvers to be considered will be introduced first in section 4.1, which will also synthesize a list of requirements the analysis methods will be assessed against in the context of the present study. Section 4.2 will introduce a number of numerical optimization techniques for the morphed shape optimization, along with their strengths and weaknesses.

4.1. Aerodynamic solvers

As introduced in chapter 1, the mechanisms through which 2-DoF compliant camber-twist morphing trailing edge wings may reduce aircraft drag are the reduction of trim drag, induced drag, pressure drag, wave drag, and viscous drag. These therefore represent the drag components the aerodynamic solver must resolve. If any of these components are absent from the model, the numerical optimizer may exploit the unmodeled physics, steering the design into a state that appears optimal in the model but is not in reality. In literature, these drag components are often grouped under umbrella terms, as illustrated in Figure 4.1. They will be treated separately here because of the differing mechanisms from which they originate.

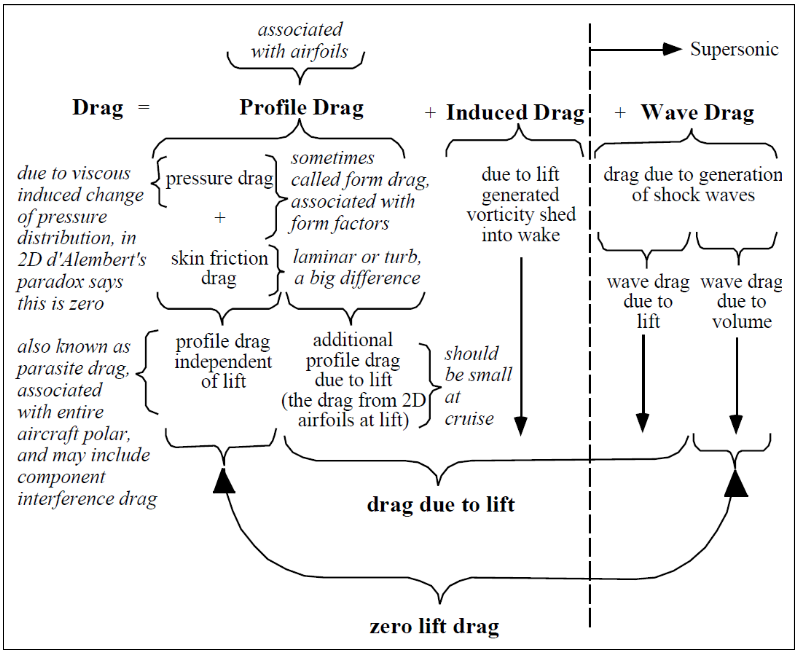

Figure 4.1: Broadbrush categorization of drag [39]

To formalize the comments made about the mechanisms having to be resolved, the set of requirements shown below is adopted for the assessment of available solvers. Requirement R6 is added to formalize the suitability of the solver for optimization problems within practical time constraints for the present study.

R1. The aerodynamic solver shall assess aerodynamic forces and moments on an aircraft in trimmed flight condition

R2. The aerodynamic solver shall resolve induced drag

R3. The aerodynamic solver shall resolve viscous drag

R4. The aerodynamic solver shall resolve pressure drag, according to the definition in Figure 4.1

R5. The aerodynamic solver shall capture wave drag effects for aircraft operating above their critical Mach number

R6. The aerodynamic solver shall have a runtime in the order of seconds to a minute per evaluation

With the requirements established, the aerodynamic solvers considered for adoption in this study are introduced and assessed against these criteria. High-fidelity CFD methods such as Reynolds Averaged Navier Stokes (RANS), and Large Eddy Simulation (LES) or Detached Eddy Simulations (DES) are not considered based on constraint R6. The solvers that are considered are listed below.

- Athena Vortex Lattice (AVL) [1]
- OpenVSP VSPaero [2]
- VSAERO [3]
- Cmarc [4]
- TranAir [40]
- Matrics-V [41]
- Q3D [42]

The first two of the solvers mentioned above, AVL and VSPaero, are based on the vortex lattice method. The vortex lattice method is a surface singularity method that assumes inviscid and irrotational flow [43, 206], and models three-dimensional lifting surfaces as having zero thickness [43, 341]. These underlying assumptions mean that they fail to adhere to requirements R3, R4, and R5. Because of this, they will not be detailed further. Cmarc is also an inviscid flow solver, meaning it also cannot adhere to requirement R3. VSAERO, TranAir, and Matrics-V are all three full potential flow solvers which can capture thickness effects, compressibility effects, and viscous effects through integral boundary layer modeling. The drawback of these programs is that they are older and less widely available than others. Furthermore, the reported runtimes of these programs exceed requirement R6. VSAERO and Matrics-V have a runtime of five minutes and upwards at low-speed conditions [42], expected to increase for transonic conditions. TranAir can take up to 2 hours CPU time in transonic conditions [40].

Q3D is a quasi-three-dimensional aerodynamic solver that was developed specifically for wing shape optimization. It is based on a combination of the vortex lattice method, strip theory, and taper-adjusted simple sweep theory. The program calculates the lift distribution over an arbitrary wing by employing the vortex lattice method in AVL, after which the local lift coefficients at a given number of strips placed equidistantly along the wingspan are transformed to sweep-normal values. Two-dimensional airfoil aerodynamic analysis tools like Xfoil[5], or VGK[6] are then used to find the viscous drag, pressure

[1] https://web.mit.edu/drela/Public/web/avl/, accessed: 4-5-2026
[2] https://openvsp.org/, accessed: 4-5-2026
[3] https://www.am-inc.com/VSAERO.html, accessed: 4-5-2026
[4] http://www.aerologic.com/cmarc.html, accessed: 4-5-2026
[5] https://web.mit.edu/drela/Public/web/xfoil/, accessed 5-5-2026
[6] https://beta.esdu.com/toolbox/docviewer/vgkuserguide?sess=unlicensed_1241229195640wgh, accessed 5-5-2026

drag, and wave drag if applicable. These values are subsequently transformed back to streamwise values, after which pressure drag, viscous drag, and the wave drag can be found by integrating the drag values at the strips along the span. This approach makes Q3D significantly quicker than methods like VSAERO and Matrics-V. For low-speed cases with the same geometry and freestream conditions, Q3D had a runtime of twenty to fifty seconds. VSAERO and Matrics-V took upward of four minutes [42]. Yet, Q3D produces similar results for both low- and high-speed cases, as shown in Figure 4.2.

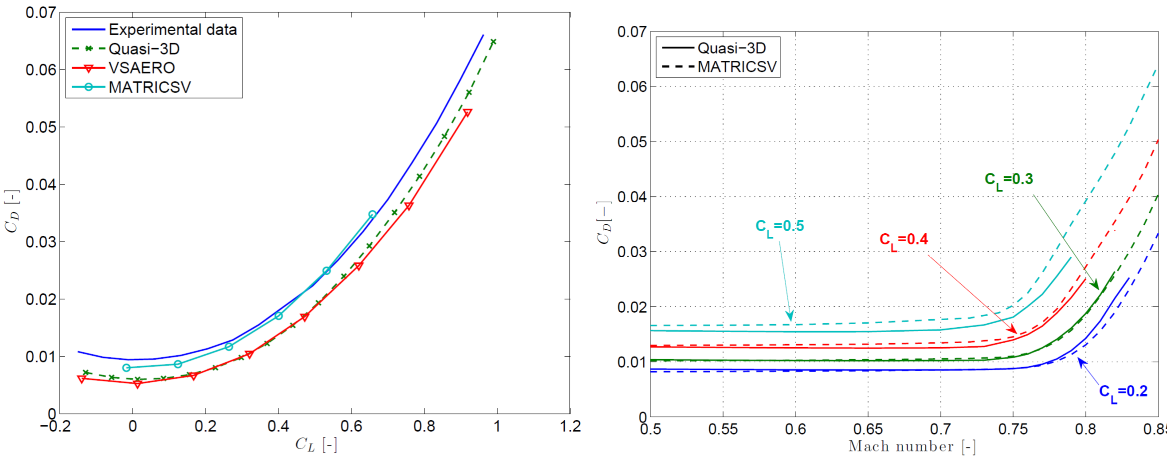

(a) Low-speed C_D-C_L curve of NACA-24-30-0 wing

(b) C_D-M curve of Fokker 100 wing, h = 37000 ft

Figure 4.2: Q3D low- and high-speed validation cases against experimental data, VSAERO, and Matrics-V [42]

When compared to the requirements on the aerodynamic solver presented above, Q3D meets all except requirement R1. In its current form, Q3D is suited to calculating the drag of a wing only, and does not impose a trimming condition. Nevertheless, Q3D employs AVL for its three-dimensional calculations, which has a trim module. Furthermore, the source code of Q3D is available, meaning it can be used as a basis for a quasi-three-dimensional trimmed performance analysis tool.

4.2. Optimization techniques

In this section, a number of numerical optimization techniques will be introduced. Focus will be on those typically applied within the context of engineering (design) optimization. In general, optimization problems are formulated as stated below [44, 15], meaning the goal is to minimize an objective function $f(x)$ by varying the elements of the vector of design variables x within their bounds, possibly subject to inequality constraints $g(x)$ and equality constraints $h(x)$.

$$\begin{array}{lll} \text{minimize} & f(x) & \\ \text{where} & x = [x_1, x_2, ..., x_{n_x}] \quad \text{vector of design variables} & (4.1) \\ \text{by varying} & \underline{x}_i \leq x_i \leq \bar{x}_i, \quad i = 1, \dots, n_x & \\ \text{subject to*} & g_j(x) \leq 0, \quad j = 1, \dots, n_g & \\ & h_l(x) = 0, \quad l = 1, \dots, n_h & \end{array} \tag{4.2}$$

At a high level, optimization techniques can be divided into two groups: gradient-based and gradient-free. Gradient-based methods, as the name suggests, use the gradient of the objective function $\nabla f(x)$ with respect to x to navigate the design space and find an optimum value. According to Martins and Ning [44, 96], line-search algorithms are most commonly applied in general non-linear gradient-based optimization. At each iteration, these algorithms determine a search direction p_k within the design space, along with a step length α_k. The vector of design variables is then updated with this information. Typically, the convergence criteria for gradient-based optimization are the magnitude of the gradient vector falling below a threshold, or the step length α_k being so small that no significant progress is made [44, 93]. A graphical illustration of gradient-based optimization using line-search algorithms is shown in Figure 4.3.

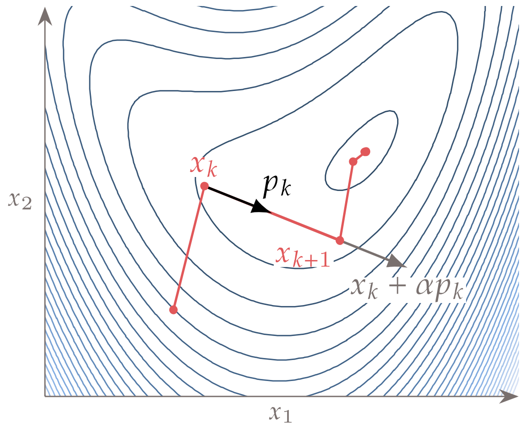

Figure 4.3: Graphical representation of unconstrained gradient-based optimization using the line search approach [44, 97]

A key advantage of gradient-based algorithms is that they remain efficient, in terms of total number of function evaluations, when the number of design variables increases [44, 22]. There is a prerequisite to this, however, and that is that the gradient of the value of the objective function with respect to the design variables is available. When this information is not available, the gradient of the objective function has to be approximated through finite differences. If this is the case, the required number of function evaluations per major optimizer iteration goes up significantly, and scales with the number of design variables. Furthermore, there may be significant inaccuracies in the estimated gradient [44, 281]. Whether the gradient information is available or not depends on the type of solver being used. Solvers that do provide gradient information are typically called adjoint solvers, while solvers that only output the objective function value are called black-box solvers.

Gradient-free optimization algorithms are generally more flexible than gradient-based approaches. A substantial benefit, for example, is that gradient-free optimizers do not require function smoothness to function correctly [44, 282]. Furthermore, they are better at finding global optima within the design space. Gradient-based methods converge to minima of the objective function, whether these are local or global. The biggest limitation of gradient-free optimization algorithms, as stated by Martins and Ning [44, 283] is the scaling of the required number of function evaluations with the number of design variables. This is illustrated for the cost optimization of the n-dimensional Rosenbrock function. The gradient-based method uses analytical gradients in this case [44, 283].

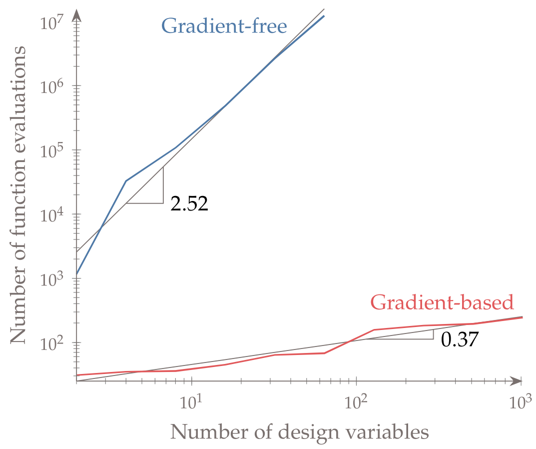

Figure 4.4: Number of function evaluations for cost optimization of n-dimensional Rosenbrock function for gradient-based and gradient-free optimization algorithms [44, 283]

As discussed in section 4.1, Q3D may be used as a basis for a new aerodynamic analysis tool that adheres to all requirements that were set. The reported runtimes of Q3D are twenty to fifty seconds. For repeated function evaluations in optimization context, this would still make it expensive to run. Furthermore, the version of Q3D of which the source code was made available operates as a black box solver. One of the gradient-free optimization algorithms that is particularly well suited at optimizing expensive black-box objective functions is Bayesian optimization. In Bayesian optimization, a surrogate model for the objective function is built. The uncertainty in this surrogate model is subsequently quantified using Gaussian process regression, a Bayesian machine learning technique. The optimizer determines where to sample next based on an acquisition function defined from the surrogate [45]. This is illustrated in Figure 4.5.

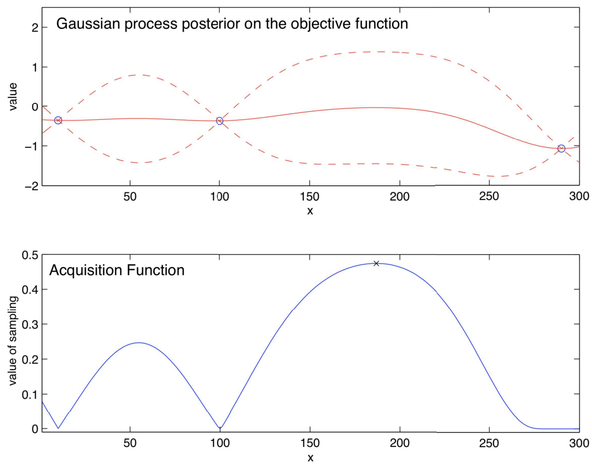

Figure 4.5: Illustration of how Bayesian optimization determines next sample. Top figure shows 3 noise free observations of the objective function f, an estimate of $f(x)$ in solid red, and Bayesian credible intervals for $f(x)$ obtained through Gaussian process regression. Bayesian optimization samples next where the acquisition function is maximum [45]

As for other gradient-free optimization techniques, the computational cost of Bayesian optimization scales poorly with an increasing number of design variables. Frazier [45] outlines that it works best when the domain has less than twenty dimensions. There are techniques to mitigate this problem, which are presented by Maathuis [46], but these fall outside of the scope of the present study.

Summarizing, gradient-based optimization is most efficient in high-dimensional spaces, provided that the optimizer is provided with information about the gradient. The use of finite differences for estimating the gradient introduces errors, as well as increasing computational cost significantly. Of the gradient-free methods, Bayesian optimization is the most promising as it is particularly well suited to expensive black-box solvers for the objective function. It may be used as long as the number of design variables remains limited to twenty or less. Regardless of the optimization technique that will be used, minimizing the number of design variables will reduce the cost of the wing shape optimization, and should be adopted as an objective for the parametrization of wing morphing.

5

Airfoil maximum lift estimation

The present chapter will discuss aerodynamic analysis methods for the estimation airfoil maximum lift coefficients. As presented in subsection 3.1.3, high-lift performance in conceptual aircraft design is commonly generalized in airfoil space, and subsequently transformed to three-dimensional wing performance. Therefore, the maximum lift coefficients of morphing airfoils are of interest to estimate the high-lift performance of compliant morphing trailing edge wings. The methods considered for investigating the high-lift performance of morphing airfoils are listed below.

- Xfoil[1]
- MSES[2]
- Reynolds-Averaged Navier-Stokes (RANS) solvers
- Large Eddy Simulation (LES)
- Detached Eddy Simulation (DES)

To correctly assess the suitability of the solvers listed above for the task of estimating airfoil maximum lift coefficients, relevant operating conditions will first be defined in terms of chord-based Reynolds number and freestream Mach number. Considering this study focuses on high-lift performance, the relevant flight phases to be studied are take-off and landing. The aircraft category of interest in the present study are large turbine powered aircraft [8]. The aircraft that fall in this category range from regional turboprop aircraft to long-range wide-body jet transport aircraft. Given the differences in wing planform geometry, and take-off and landing speed across this category, the representative Mach- and Reynolds numbers span a considerable spectrum of values. To establish a well-founded order of magnitude for the operating conditions, the effective chord-based Reynolds number and freestream Mach number in approach configuration will be calculated for two aircraft that sit on either end of the spectrum: the ATR 72-600, representing the regional turboprops, and the Airbus 380-800, representing the long-range wide-body jet transports. The atmospheric parameters required for the calculations are found using the International Standard Atmosphere[3] (ISA), for an altitude of 1000 feet, or $304.8\,\mathrm{m}$. Provided the objective is to motivate an order of magnitude to be considered, the effect of the altitude is small, as the variation in atmospheric parameters is modest between sea-level and 1000 feet. The atmospheric parameters are listed below.

- Air density, ρ: $1.1859\,\mathrm{kg\,m^{-3}}$
- Air dynamic viscosity, μ: $1.7798 \times 10^{-5}\,\mathrm{kg\,m^{-1}\,s^{-1}}$
- Speed of sound, a: $339.12\,\mathrm{m\,s^{-1}}$

[1] https://web.mit.edu/drela/Public/web/xfoil/, accessed 5-5-2026
[2] https://web.mit.edu/drela/Public/web/mses/, accessed 5-5-2026
[3] https://www.pdas.com/atmoscalculator.html, accessed: 5-5-2026

As the high-lift study is carried out on airfoils, the operating conditions have to be defined normal to the representative sweep line. Considering aircraft take-off and land at subsonic speeds, the quarter-chord sweep line is adopted as being representative [42]. Equations (5.1) and (5.2) are used to perform the transformations [42, 41]. The effective Mach number can also be found by using equation (5.1), noting that the speed of sound stays constant.

$$V_{\perp} = V_{\infty} \cos \Lambda_{c/4} \tag{5.1}$$

$$c_{\perp} = c_{stream} \cos \Lambda_{c/4} \tag{5.2}$$

The required parameters for the calculations, along with their results are presented in Table 5.1. Considering the effective Mach number for both aircraft is well below 0.3, incompressible flow can be assumed [47, 235]. The order of magnitude for the Reynolds numbers to be expected is 10^7.

Table 5.1: Computation of effective Reynolds and Mach numbers in approach configuration for ATR 72-600 and Airbus 380-800

Aircraft	V_{app} [kts]	$\Lambda_{c/4}$	MAC [m]	$Re_{eff} \times 10^6$ [-]	M_{eff} [-]
ATR 72-600 [48, 49]	113	$0°$	2.2345	8.655	0.17
Airbus 380-800 [50, 51]	138	$33.5°$	12.3	40.46	0.1745

At the Reynolds numbers in the order presented, Xfoil and MSES have been shown to frequently overpredict the maximum lift coefficients of airfoils [52]. Furthermore, Xfoil is not fit for modeling flows with a high degree of separation due to the fact that it is a surface panel method, meaning flow physics away from the airfoil are not resolved. Since significant separation is expected over the trailing edge portion of morphing airfoils in high-lift configuration, Xfoil is not suitable for the high-lift study. Maughmer and Coder [52] compared the results generated by the Reynolds-Averaged Navier-Stokes (RANS) solver Ansys Fluent[4], using the Langtry-Menter extension of the $k - \omega$ SST turbulence model, to experimental results, showing a better agreement. An additional advantage of RANS solvers is that flow physics in separated regions are modeled better.

Dong *et al.* [53] compared the accuracy of RANS solvers to Detached Eddy Simulations (DES). DES is a hybrid version of RANS and Large Eddy Simulation (LES), in which the area near walls are modeled using the RANS equations while LES is used to model the outer flow. This approach is taken as capturing boundary layer effects in LES requires very fine meshes, as the turbulent eddies in the boundary layer are small. Using RANS in the boundary layer relaxes the requirement on the mesh density near walls, while large, energy containing eddies in the outer flow can be captured. A key result of the work by Dong *et al.* [53] is that DES does not produce significantly more accurate results than RANS for airfoils that exhibit trailing edge stall. They showed this using a comparison between the experimental lift polar and predicted lift polars by RANS and DES of the NACA 63_3-018 airfoil, as shown in Figure 5.1. The Reynolds number and Mach number for this study are 5.8×10^6 and 0.3 respectively.

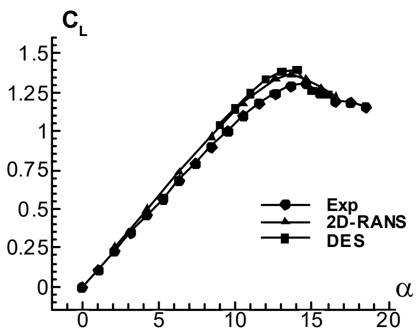

Figure 5.1: Comparison of experimental lift polar and predicted lift polars by RANS and DES for NACA 63_3-018 at $Re = 5.8 \times 10^6$ and $M = 0.3$ [53]

[4] https://www.ansys.com/products/fluids/ansys-fluent, accessed: 10-06-2026

The use of RANS solvers over DES or LES has an additional advantage: the flow can be treated as (quasi-) two-dimensional. Eddy structures are inherently three-dimensional, requiring a three-dimensionally refined grid to resolve them. This increases the required cell count significantly. LES is therefore outside the scope of the present study, requiring both three-dimensionally refined meshes and prohibitively fine meshes near walls.

In the RANS equations, flow quantities are expressed as the sum of their mean and fluctuating parts. When the terms in the Navier-Stokes equations are expressed in terms of a mean and fluctuating part, momentum fluxes appear due to the non-linearity of the equations, which act as apparent stresses. The derivation of equations for these stresses results in more unknown quantities. With more unknowns than equations, the problem can not be closed [54, 33]. Turbulence models are used to mitigate this closure problem. Two of the most commonly used turbulence models for external aerodynamics are the two-equation $k-\omega$ SST model and the one-equation Spalart-Allmaras (SA) model [55], which were specifically developed for use in aeronautical context [56, 57]. Rumsey and Ying [55] showed that both turbulence models produce similar results in high-lift conditions.

Even though the results produced are similar, both models overpredicted the stall angle and maximum lift coefficient when tested on the NHLP-2D three-element airfoil at a Reynolds number of 3.52×10^6 and a Mach number of 0.2. Matyushenko and Garbaruk [58] found that the overprediction of the maximum lift coefficient and stall angle of airfoils by RANS CFD using semi-empirical turbulence models, which the SST and SA model are, is systemic. For the SST model, he found that this is due to an overestimation of turbulent eddy viscosity in boundary layers under and adverse pressure gradient. In the incompressible version of the SST model, the turbulent eddy viscosity is found according to equation (5.3) [58]. The standard value of a_1 in the SST model is 0.31, which has been calibrated on a set of standard turbulent flows.

$$\mu_t = \frac{a_1 k}{\max\left(a_1 \omega, SF_2\right)} \tag{5.3}$$

In the work by Matyushenko and Garbaruk [58], he re-calibrated the a_1 constant to obtain more realistic results for moderately thick to thick airfoils for Reynolds numbers in the order 1×10^6 to 1×10^7. The a_1 constant that gave the most accurate results for the airfoils tested was 0.28. The author does note that the recalibration of the constant did make the model less accurate for other turbulent flows, highlighting that semi-empirical turbulence models are not universally correct.

In its standard form, the SST model assumes a fully turbulent boundary layer. Langtry and Menter [59] proposed an extension of the model to model laminar to turbulent transition. To do this, they introduced two new transport equations, solving for the transition momentum thickness Reynolds number Re_θ and an intermittency factor γ_{int}. The model was calibrated for Reynolds numbers up to 1×10^7, with the notion that laminar flow over conventional airfoils above this Reynolds number is limited to the very front of the airfoil, yielding no significant improvement over the standard version.

Summarizing, this chapter has laid out methods that can be used for estimating the maximum lift coefficients of airfoils, which can be used for estimating the high-lift performance of morphing wings. The importance of generating a well-founded estimate for this was detailed in chapter 3. The use of high-fidelity CFD methods over methods such as Xfoil or MSES is necessary due to the high degree of flow separation that is expected for airfoils near stall, and for morphing airfoils in high-lift configuration. RANS solvers emerge as the preferred tool, as these balance accuracy and computational expense, provided that the goal of the high-lift study is to find a motivated $\Delta C_{l_{max}}$ for camber morphing trailing edge airfoils in high-lift configuration over their baseline shapes.

6 Research Questions

In this chapter, a formal set of research questions for the present study will be defined. The research questions flow down from key findings in chapter 3 and chapter 4, and are connected to the research objectives presented in chapter 1. Referring back to these objectives, the main goal of the present study is to investigate, at conceptual design level, how implementing compliant 2-DoF camber-twist morphing trailing edge wings on CS-25 aircraft influences their performance, in terms of fuel consumption, when taking into account the effects on the sizing of the aircraft. The block-fuel consumption is adopted as the primary performance metric because it encompasses the trade between the improved aerodynamic efficiency and possible sizing penalties. The main research question for the present study that follows is presented below.

RQ. *What is the effect of implementing a two-degree-of-freedom camber-twist morphing trailing edge wing on the block-fuel consumption of a CS-25 transport aircraft over a given mission, compared to a reference aircraft with a conventional wing, when assessed at conceptual design level?*

In order to find an answer to the main research question, four supporting sub-questions are identified. The answers to these questions represent methods and results that must be generated before a meaningful answer to the main research question can be found. First, Q1 establishes how the shape of a 2-DoF camber-twist morphing wing can be described efficiently, minimizing the number of design variables and thereby reducing the dimensionality of the wing-shape optimization problem discussed in chapter 4. Next, Q2 addresses the aerodynamic analysis method required for analyzing and optimizing the cruise aerodynamic efficiency of morphing wing aircraft. Q3 focuses on the conceptual sizing of aircraft with morphing wings, for which Q3.1 covers an important part of the sizing methodology itself, and Q3.2 is required for an important input to the sizing process. Finally, Q4 investigates how top-level design requirements govern the sizing and performance of morphing wing aircraft, providing the sensitivity context needed to interpret the answer to the main research question.

Q1. How can chordwise 2-DoF camber-twist morphing be parametrized for wings with arbitrary base airfoils using a minimum amount of variables while sufficiently describing the morphed shape space?

Q2. How can the aerodynamic efficiency in cruise of a CS-25 aircraft with a 2-DoF compliant camber-twist morphing trailing edge wing be assessed at conceptual design level, using a method with a runtime in the order of seconds to a minute that resolves relevant drag components?

Q3. How can a CS-25 transport aircraft with a 2-DoF compliant camber-twist morphing trailing edge wing be sized at conceptual design level?

Q3.1. How can the uncertainty in the structural mass prediction of 2-DoF camber-twist morphing trailing edge wings for transport aircraft at conceptual design level be mitigated, given the absence of validated empirical weight models?

Q3.2. What is the $\Delta C_{l_{max}}$ that a morphing airfoil in high-lift configuration can deliver over its baseline configuration, when assessed with high-fidelity methods?

Q4. What is the effect of implementing a 2-DoF compliant camber-twist morphing trailing edge wing on the conceptual-level sizing of a CS-25 transport aircraft, and how sensitive are these outcomes to the mass of the morphing system and to the top-level design requirements?

II

Methodological contributions

7
Parametrization of wing morphing

The present chapter will detail the parametrization of morphing, which represents the important first step before any analysis on morphing wings can be carried out. As established in chapter 3 and further detailed in chapter 4, finding the wing shape for minimum drag, or maximum aerodynamic efficiency, is an optimization problem. In chapter 4, the objective was set to minimize the number of variables required for describing morphing, as this reduces the dimensionality, and therefore the cost, of the optimization problem. A first important note to make about the parametrization of camber-twist morphing is that they are closely related. Chapter 1 discussed how twist morphing is often achieved by differential camber morphing at different spanwise locations. Hence, this will be used here as well. The problem therefore reduces to how chordwise 2-DoF camber morphing can be described in airfoil space using the least amount of variables. This will be detailed first in section 7.1. As will become clear in this section, the camber- and thickness distributions of airfoils are required to model camber morphing. An important part of Q1 is that the parametrization method should be applicable to wings with arbitrary base airfoils. The camber- and thickness distributions of airfoils are not always known. To retrieve them, the Class Shape Transformation (CST) is used. This will be detailed in section 7.2.

7.1. Modeling chordwise 2-DoF camber morphing in airfoil space

The present section will detail how the shapes of chordwise 2-DoF camber morphing airfoils are generated. Camber morphing, as the name suggests, entails the alteration of the camber distribution of airfoils. Hence, the logical first step is to detail how airfoil shapes follow from the camber distribution. The camber line is defined as the locus of points halfway between the upper and lower surface, measured perpendicular to the camberline itself [60, 290]. The upper- and lower surface coordinates, denoted with u and l respectively, follow from the camber- and thickness distributions according to equation (7.1). The subscripts c and t denote the camber and thickness distributions. The parameter θ is the angle of the camberline with respect to the horizontal, which is equal to the arctangent of the slope of the camberline.

$$x_u = x_c - z_t \sin\theta, \qquad z_u = z_c + z_t \cos\theta \tag{7.1a}$$
$$x_l = x_c + z_t \sin\theta, \qquad z_l = z_c - z_t \cos\theta \tag{7.1b}$$

The present study focuses on trailing edge morphing. Hence, only the rear part of the camber distribution is changed. The morphing part of the airfoil is assumed to run from the rear spar to the trailing edge. The rear spar location is the first input required for generating morphed shapes. It is denoted by x_{rs}, which is in chord normalized coordinates. Next, three control points are placed on the camberline: one at the location of the rear spar, one at the mid-point between the rear spar trailing edge, and one at the trailing edge. These locations will further be referred to as ”rs”, ”mid”, and ”te” respectively for brevity. An example of the control point locations is shown in Figure 7.1.

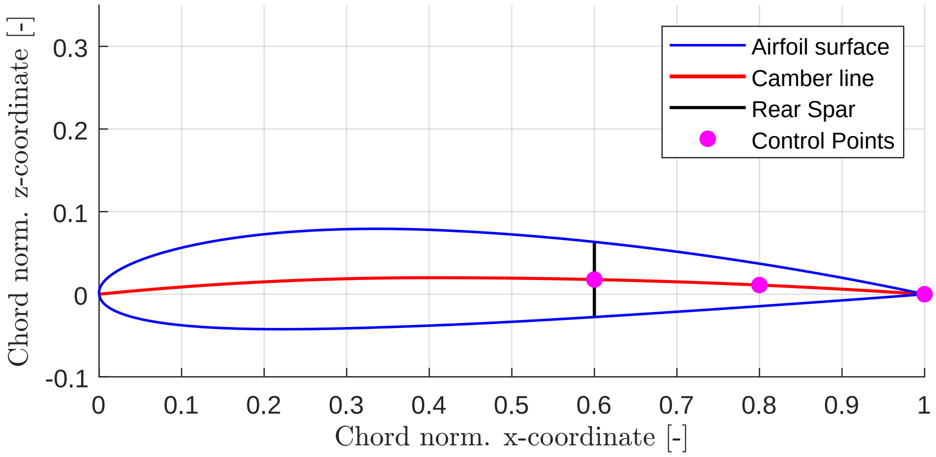

Figure 7.1: Control point locations for NACA 2412 airfoil with $x_{rs} = 0.6$

Two straight line segments are defined next. One between the rs-control point and mid-control point, and one between the mid-control point and te-control point. For both of these segments, their length and angle with respect to the horizontal are calculated. The lengths are referred to as l_1 and l_2, and the angles as θ_{01} and θ_{02}. The other two inputs required for generating the morphed shape are two deflection angles: θ_1 and θ_2. These angles define the deflection of the two line segments from their respective undeflected angles θ_{01} and θ_{02}. The new locations of the mid-control point and te-control point are subsequently found using equations (7.2a) and (7.2b).

$$x_{mid} = x_{rs} + l_1 \cos(\theta_{01} + \theta_1), \qquad z_{mid} = z_{c,rs} - l_1 \sin(\theta_{01} + \theta_1) \tag{7.2a}$$

$$x_{te} = x_{mid} + l_2 \cos(\theta_{02} + \theta_1 + \theta_2), \qquad z_{te} = z_{mid} - l_2 \sin(\theta_{02} + \theta_1 + \theta_2) \tag{7.2b}$$

After displacing the control points, a fourth-order polynomial is fitted that will represent the camberline for $x > x_{rs}$. The conditions used for this polynomial fit are first-order continuity in the rs-control point, that the polynomial passes through the displaced mid- and te-control points, and a specified slope at the trailing edge. The specified slope follows from the original slope of the camber line at the trailing edge, adjusted for the effect of the deflections θ_1 and θ_2, defined as the expression below.

$$\left(\frac{dz_c}{dx}\right)_{te} = \tan\left(\arctan\left(\frac{dz_c}{dx}\right)_{TE} + \theta_1 + \theta_2\right) \tag{7.3}$$

The morphed camber line of the entire airfoil can now be found by combining the part before the rear spar, which remains unchanged, with the fourth order polynomial. In principle, the surfaces of the morphed airfoil can now be found using equation (7.1). However, before finding the final airfoil surface coordinates, the length of the part behind the rear spar is iteratively adjusted so that the arc length of the suction side skin is maintained. This has to be accounted for in the thickness distribution, as the domain of the part behind the rear spar is changing. Hence, the thickness distribution for $x > x_{rs}$ is approximated with a fourth-order polynomial as well. To maintain first-order continuity on the airfoil surface at x_{rs}, the original thickness distribution value and slope are imposed at the rear spar. The thickness at the trailing edge is also maintained. Although not strictly required in physical sense, thickness and thickness slope at the mid-control point are maintained in order to obtain sufficient conditions to fit the polynomial. Maintaining this makes sense because modeling camber morphing is of interest, removing the effect of varying thickness. The iterative scaling of the trailing edge part is presented in pseudo code in Algorithm 1. After the iterative scaling of the trailing edge, the undeformed front part of the airfoil and the morphed trailing edge are combined to obtain the final morphed airfoil shape.

Figure 7.1 shows an example morphed airfoil based on the NACA 2412, illustrating the displacement of the control points and that first-order continuity is maintained in the camberline and on the surfaces at the rear spar.

Algorithm 1 Arc-length-preserving scaling of the morphed trailing-edge segment

Inputs: Morphed camber coordinates $\{\hat{x}_c, \hat{z}_c\}$, camber slope θ, target arc length s^*, thickness BCs, tolerance ε
Outputs: Scaled $\{\hat{x}_c, \hat{z}_c\}$ with suction-side arc length $\approx s^*$

```
Compute suction-side arc length s
while |s* − s| > ε do
    Fit 4th-order polynomial to thickness distribution with BCs at x_RS, x_mid, x_TE
    Compute suction-side surface coordinates
    Compute suction-side arc length s
    λ ← s*/s
    x̂ ← x_RS + λ (x̂ − x_RS)
    Ẑ_c ← ẑ_c,RS + λ (ẑ_c − ẑ_c,RS)
end while
```

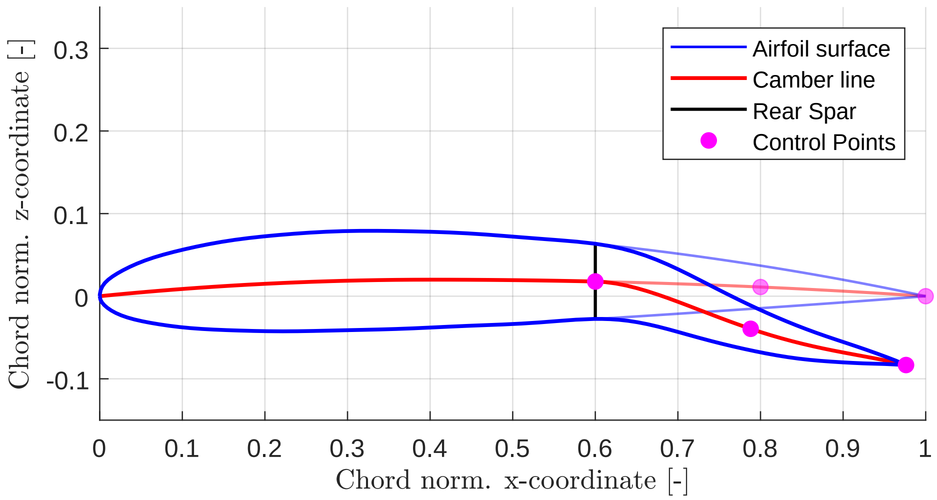

Figure 7.2: Deflected and undeflected NACA 2412 with camberline and control points

7.2. Class Shape Transformation

In the previous section, the methodology used for generating morphed airfoil shapes has been detailed. This methodology requires the camber- and thickness distributions of the baseline airfoil. For the NACA 4 series family of airfoils that was used as an example in section 7.1, analytical definitions for the camber- and thickness distributions exist, but this is not the case for all airfoils. Given that the parametrization technique has to be applicable to arbitrary airfoils, as detailed in Q1, a method is required to retrieve smooth functions for these distributions. The Class-Shape Transformation (CST) parametrization technique is used for this. CST is a shape parametrization method through which a large array of geometries can be described using relatively few variables. The general form of the parametrization is shown in equation (7.4), in which ζ denotes chord normalized z-coordinate, and ψ represents the chord normalized x-coordinate. The variable ζ_T is the normalized z-coordinate at the trailing edge, allowing for the modeling of blunt trailing edges [61].

$$\zeta(\psi) = C_{N2}^{N1}(\psi)\,S(\psi) + \psi\zeta_T \tag{7.4}$$

In the equation above, $C_{N2}^{N1}(\psi)$ is the class function, of which the definition is shown in expression (7.5). The constants $N1$ and $N2$ follow from the class of geometry to be modeled. For airfoils with round noses and sharp trailing edges, the constants are $N1 = 0.5$ and $N2 = 1.0$ respectively [61].

$$C_{N2}^{N1}(\psi) = (\psi)^{N1}(1-\psi)^{N2} \tag{7.5}$$

The function $S(\psi)$ in expression (7.4) is called the shape function. The shape function is a weighted sum of Bernstein polynomials of order n, using coefficients A_i. To match existing airfoil geometries, the coefficients can be determined using a least squares fit [61].

$$S(\psi) = \sum_{i=1}^{n} A_i \binom{n}{i} \psi^i (1-\psi)^{n-i} \tag{7.6}$$

For airfoils that are non-symmetric, the upper and lower surfaces each get their own set of coefficients; A_u and A_l respectively. For symmetric airfoils it holds that $A_l = -A_u$. The coefficients of the shape functions of the camber- and thickness distributions, can be found as the average of and the difference between the upper and lower surface coefficients. Combined with the class function, they yield smooth camber and thickness distributions.

Kulfan [61] reports that CST parametrized airfoils are *statistically identical* to the actual airfoil definition when the order of the Bernstein polynomials in the shape function is six or larger. Furthermore, the slopes and second derivatives of the upper and lower surface z coordinates w.r.t x matched analytical definitions well. To verify this, the parametrization technique was tested using the analytical definition for the NACA 4 series family of airfoils. The camberline, and its gradient, of one such airfoil is defined by equations (7.7) and (7.8) respectively, where m and p are the first and second digit of the airfoil code [62].

$$z_c = \begin{cases} \frac{m}{p^2}\left(2px - x^2\right) & 0 \leq x < p \\ \frac{m}{(1-p)^2}\left(1 - 2p + 2px - x^2\right) & p \leq x \leq 1 \end{cases} \tag{7.7}$$

$$\frac{dz_c}{dx} = \begin{cases} \frac{2m}{p^2}(p - x) & 0 \leq x < p \\ \frac{2m}{(1-p)^2}(p - x) & p \leq x \leq 1 \end{cases} \tag{7.8}$$

The thickness distribution of NACA-4-series airfoils is given by equation (7.9), where the parameter t is equal to the last two digits of the airfoil code divided by 100. The upper and lower surface coordinates can then be found from the camber- and thickness distribution using equation (7.1).

$$z_t = 5t\left(a_0\sqrt{x} + a_1 x + a_2 x^2 + a_3 x^3 + a_4 x^4\right) \tag{7.9}$$

For the comparison between CST and the analytical definition, the NACA 2412 is used. The camberline was discretized using 96 points, divided over the chord-normalized space according to the symmetric cosine spacing in equation (7.10). Increasing the point count beyond 96 was found to give diminishing results in terms of the error of CST with respect to the analytical definition. Moreover, excessively fine discretization can cause the second, and sometimes third, point on the upper surface to be placed in front of what is normally the leading edge at $(x_c, z_c) = (0, 0)$. This is due to the slope, and therefore angle, of the camberline being nonzero at $x = 0$. The rapidly increasing thickness near the leading edge, due to the $\sqrt{x}$ term in the thickness distribution, caused the $z_t \sin\theta$ term in equation (7.1) to exceed x_c in magnitude.

$$x_c = \frac{1}{2}(1 - \cos\phi), \qquad 0 \leq \phi \leq \pi \tag{7.10}$$

The CST parametrization errors for the NACA 2412 airfoil with CST orders of six and ten are shown in Figure 7.3a and Figure 7.3b respectively. The maximum error, in terms of the difference in chord-normalized z-coordinate, is 1.5×10^{-3}, which occurs in the vicinity of the leading edge. Considering the coordinates are chord normalized, the error is 0.15% of the chord. The error of the tenth order CST approximation near the leading edge is slightly higher than that of the sixth order fit, and not significantly more accurate away from the leading edge.

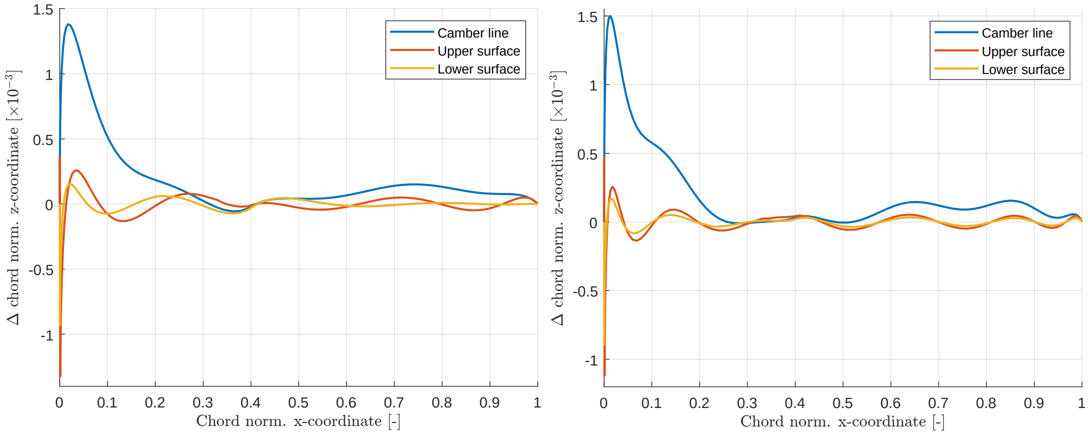

(a) CST order 6 (b) CST order 10

Figure 7.3: NACA 2412 CST parametrization error w.r.t. analytical definition, $n_p = 96$

A comparison between the analytical definition and the CST approximation with an order of six for the NACA 2412 is shown in Figure 7.4. The discrepancy in the camberline, as presented in Figure 7.3, is clearly visible in the leading edge detail shown below. The reason for this discrepancy is that the relation between the surface coordinates and camberline coordinates in equation (7.1) is not strictly followed. As introduced, the CST coefficients of the camber line are found as the average of the upper and lower surface coordinates. This means that the camberline predicted by CST is the line that is equidistant from the upper and lower surface at any point, but not measured perpendicular to the camberline itself. This creates discrepancies in areas of high curvature, which for airfoils is mainly near the leading edge.

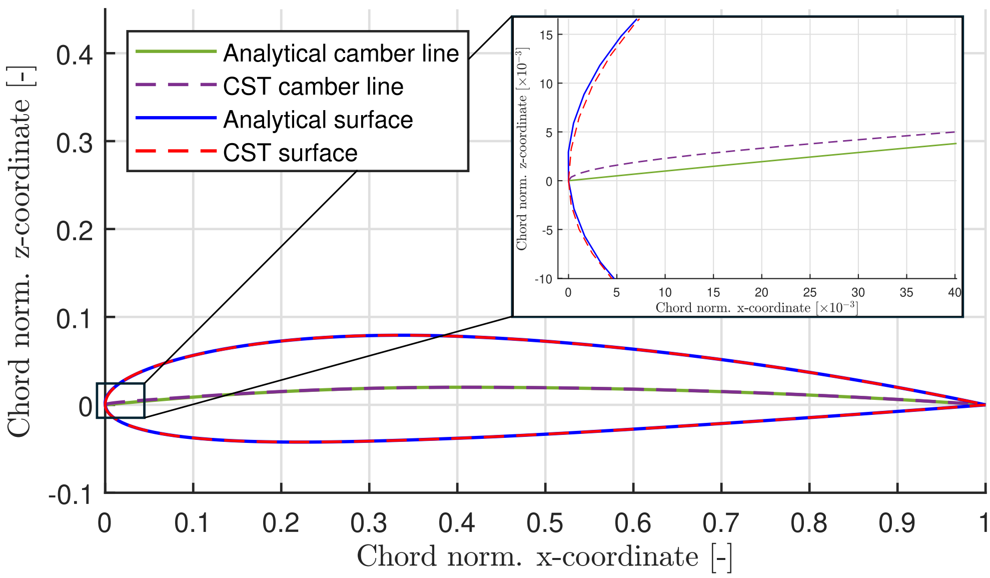

Figure 7.4: Comparison between NACA 2412 analytical definition and CST approximation, including leading edge detail. CST order = 6, $n_p = 96$

Even though the error of the CST approximation is low away from the leading edge, the use of the camberline and thickness distribution in the procedure for generating morphed shapes, introduced in section 7.1, creates slight discrepancies where the undeformed front part of the airfoil and the morphed trailing edge meet. This is illustrated in Figure 7.5.

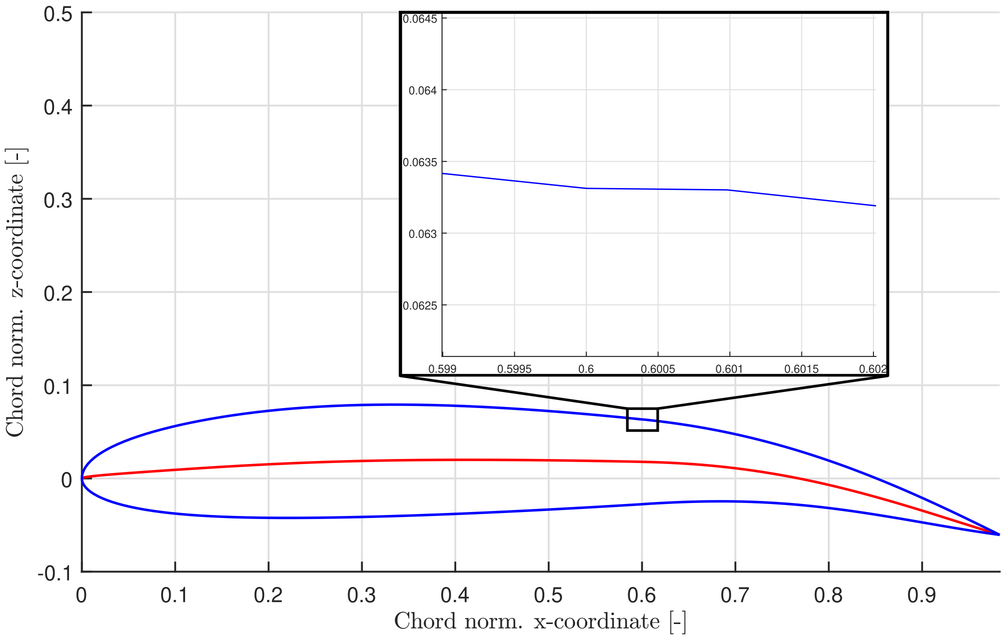

Figure 7.5: Morphing airfoil based on the NACA 2412 using the CST camber line and thickness distribution, the detailed view shows that the undeformed front part and morphed trailing edge do not meet perfectly

Although the discrepancy, in terms of chord normalized z-coordinate, is in the order of 10^{-4} or 0.01%, the effect of the surfaces not meeting perfectly can be seen in the pressure distribution as calculated by Xfoil[1]. This is shown in Figure 7.6. The rear spar location is at 60% of the chord, where a sawtooth is visible in the pressure distribution over the morphed airfoil using the CST camber line and thickness distribution.

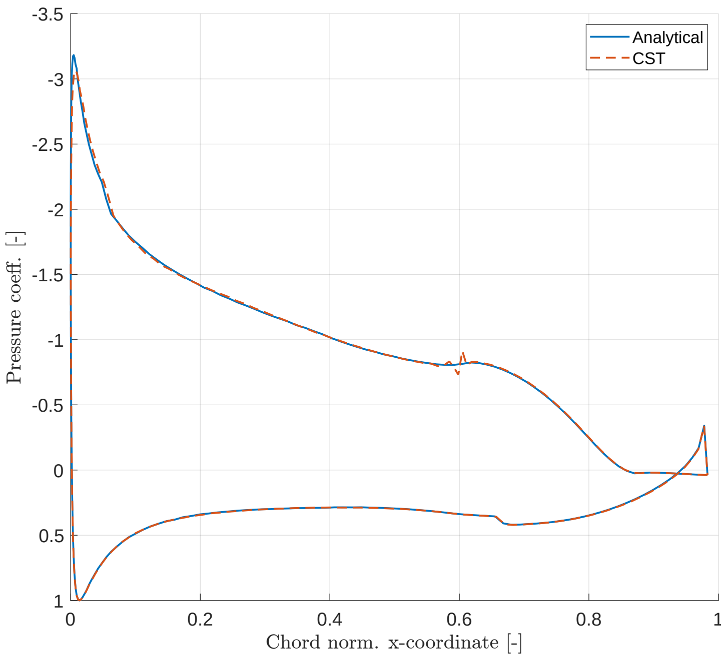

Figure 7.6: Comparison of pressure distributions over morphed airfoils based on the NACA 2412 using the analytical camber- and thickness distributions and the CST approximated ones. $Re = 3\times10^6$, $\alpha = 5°$

To mitigate the problem of the surfaces not meeting exactly, another set of CST coefficients is fit on

[1]https://web.mit.edu/drela/Public/web/xfoil/, accessed: 15-6-2026

to the deformed upper and lower surfaces separately. The order of this CST fit is higher, to allow for more accurate spatial control [61]. To do this, the upper and lower surfaces are scaled such that they span the full chord-normalized space $[0, 1]$. After fitting the CST coefficients to the respective sides, the geometry is re-generated using these CST coefficients, after which both sides get scaled back so that the chord length found after morphing is maintained. The surfaces are now smooth, which can be seen in the pressure distribution in Figure 7.7. Again, the resulting pressure distribution is compared to that of the morphing airfoil generated using the analytical camber line and thickness distributions to verify that the post-smoothing does not introduce significant errors. The largest discrepancy between the two pressure distributions can be seen on the suction side near the leading edge. This can also be seen in the pressure distribution comparison in Figure 7.6, and is a product of the CST approximation not using the exact definition of the camberline, as discussed before. It is not a product of the post-smoothing.

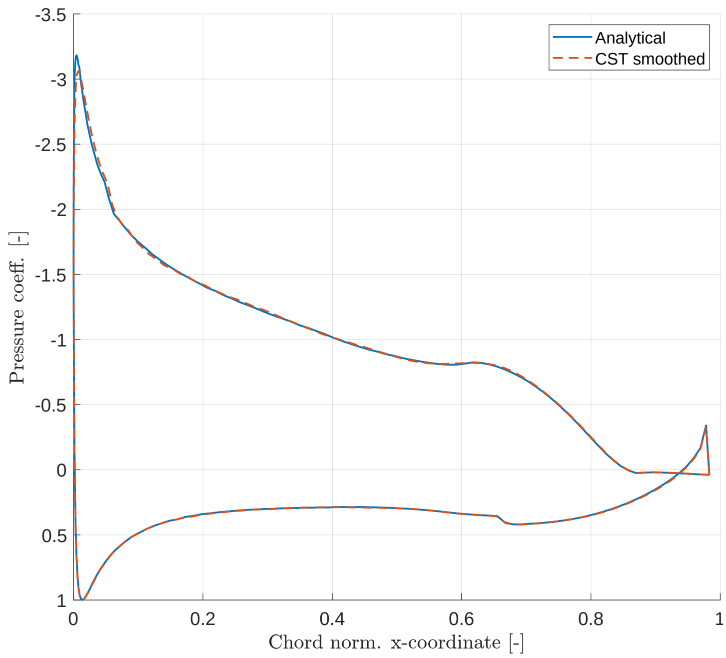

Figure 7.7: Comparison of pressure distribution over morphed airfoils based on the NACA 2412 using the analytical camber- and thickness distributions and the CST approximated ones, where post-smoothing has been applied to the latter. $Re = 3{\times}10^6$, $\alpha = 5°$

Summarizing, this chapter has shown how morphed airfoil shapes can be generated from an airfoil's camber line and thickness distribution based on a rear-spar location, and two pseudo-deflections. Camber- and twist-morphing of a wing can be modeled using morphing in airfoil space at a number of locations. As optimization of the wing structure falls outside the scope of the present thesis, the rear spar location can be assumed constant, meaning morphing can be modeled using $2n$ parameters, where n is the number of spanwise stations where 2-DoF camber morphing is modeled in airfoil space. The CST approximation has been introduced as a method of retrieving smooth functions for the camber line and thickness distributions of arbitrary airfoils. Because it is not exact, slight errors are introduced where the morphed trailing edge and undeformed front part of the airfoil meet. Using the same CST approximation, these discrepancies can be post-smoothed away without introducing a significant error.

8
Aircraft Trimmed Performance Analysis Tool

As introduced in chapter 3, there is a need for analyzing and optimizing the aerodynamic efficiency of aircraft with morphing wings in context of the present study. To do this, an aerodynamic analysis program is required. In chapter 4, a number of requirements were defined for the tool, after which the conclusion was drawn that no existing program meets all of them. Therefore, the present chapter will discuss the methodology behind, and implementation of an Aircraft Trimmed Performance Analysis Tool (ATPAT). Despite not meeting all requirements set in chapter 4, the quasi-three-dimensional (Q3D) wing drag analysis program, developed by Mariëns [42], was identified as a good basis for ATPAT. Hence, the methodology behind Q3D will be introduced first in section 8.1. Next, the methodology behind, and structure of ATPAT will be outlined in section 8.2. Following, the verification and validation of ATPAT will be presented in section 8.3. The integration of the tool in the aircraft design Initiator will be discussed last in section 8.4. Because ATPAT is developed for use in optimizing the deflected shape of morphing wings, the optimization technique employed will be motivated here as well.

8.1. Quasi-Three-Dimensional Aerodynamic Analysis

The present section will detail the methodology behind quasi-three-dimensional aerodynamic analysis of wings. Q3D was developed with the aim of being a fast, yet accurate, solver to calculate the drag of aircraft wings, to be used in multi-disciplinary design optimization (MDO) [42]. Fundamentally, the method behind Q3D divides the wing drag into induced drag and profile drag, which are calculated separately. The profile drag is found using the strip method, accounting for the effects of wing sweep and taper. For the application of the strip method, the lift distribution over a wing configuration must be found first. This is done using a vortex-lattice method (VLM) three-dimensional aerodynamic analysis, which also immediately yields the induced drag. Q3D employs AVL[1], a well known VLM analysis tool, for this first step. Next, a number of evenly spaced spanwise stations are chosen on the wing, representing the locations of the strips. Following, the airfoils normal to the representative sweep line at these locations are derived. For transonic conditions, Mariëns [42] proposes to use the half-chord sweep line. For conditions at a lower freestream Mach number, the quarter-chord sweep line should be used. Figure 8.1 illustrates the derivation of a section perpendicular to the representative sweep line.

[1] https://web.mit.edu/drela/Public/web/avl/, accessed 14-5-2026

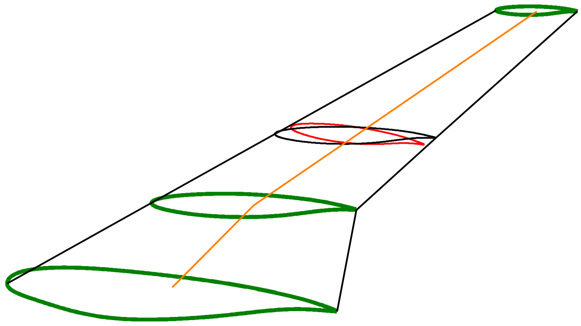

Figure 8.1: Illustration of the derivation of a section perpendicular to the half-chord sweep line at 60% semi-span [23]

After the VLM analysis, the lift coefficients at the spanwise locations of the strips are found through interpolation. Next, simple sweep theory is applied to transform the lift coefficients to sweep-normal values, according to equation (8.1). The effective freestream velocity, Mach number, and Reynolds number at which the perpendicular sections operate are found through equations (8.2), (8.3), and (8.4) respectively [42].

$$C_{l_\perp} = C_{l_{VLM}} \sec^2 \Lambda \tag{8.1}$$

$$V_\perp = V_\infty \cos \Lambda \tag{8.2}$$

$$M_\perp = M_\infty \cos \Lambda \tag{8.3}$$

$$Re_\perp = Re_\infty \frac{V_\perp}{V_\infty} \frac{c_\perp}{\bar{c}} = Re_\infty \cos^2 \Lambda \tag{8.4}$$

After finding the effective operating conditions, the viscous airfoil forces are calculated by employing two-dimensional aerodynamic tools. In the current implementation, these are Xfoil[2] or VGK[3]. Q3D automatically chooses one of these programs based on the effective Mach number at a strip. If it is above 0.55, VGK is used, as it is better suited for modeling compressibility effects. The viscous airfoil forces are calculated in an iterative manner, to transform between the angle of attack found in the VLM analysis, and the effective angle of attack in the two-dimensional aerodynamic analysis tools. The relationships between these angles is illustrated in Figure 8.2. The iteration scheme used for the transformation is presented in Algorithm 2.

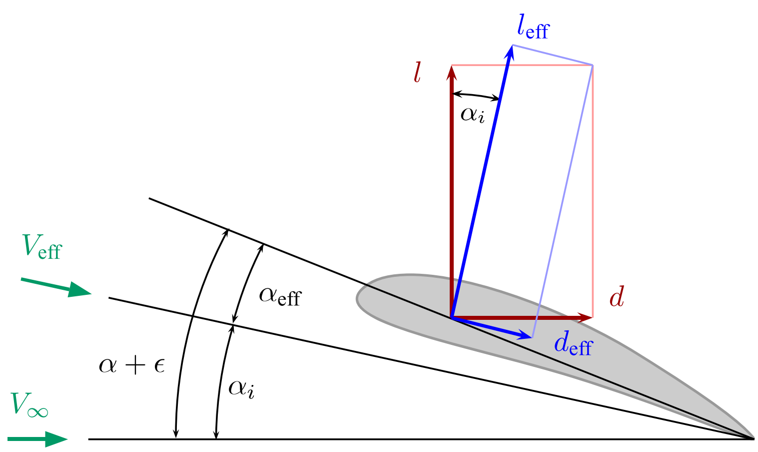

Figure 8.2: Relation between three-dimensional lift (l), three-dimensional drag (d), local lift (l_{eff}), and local drag (d_{eff}) [42, 40]

[2] https://web.mit.edu/drela/Public/web/xfoil/, accessed 14-5-2026
[3] https://www.esdu.com/cgi-bin/ps.pl?t=cdoc&p=cdoc_esduvgk, accessed 14-5-2026

Algorithm 2 Iteration scheme to transform between freestream and effective direction

1: Set $\alpha_i = 0$ and $C_{d_{eff}} = 0$
2: **while** α_i not converged **do**
3: $\quad C_{l_{eff}} = \dfrac{C_{l_\perp} \cos^2 \alpha_i + C_{d_{eff}} \sin \alpha_i}{\cos \alpha_i}$
4: $\quad V_{eff} = \dfrac{V_\infty}{\cos \alpha_i}$, compute effective Reynolds number $Re_{eff} = Re_\perp \dfrac{V_{eff}}{V_\perp}$
5: $\quad$ Find α_{eff}, $C_{d_{eff}}$, $C_{d_{p_{eff}}}$, and $C_{d_{f_{eff}}}$ using two-dimensional aerodynamic analysis tool
6: $\quad \alpha_i = -\alpha_{eff} + (\alpha + \epsilon) \cos \Lambda$
7: **end while**
8: $C_{d_\perp} = C_{d_{eff}} \dfrac{\cos \alpha_i}{\cos^2 \alpha_i} + C_{l_{eff}} \dfrac{\sin \alpha_i}{\cos^2 \alpha_i}$

The second term in step 8 of the iteration scheme above represents the induced drag. This is not further taken into account at this stage as it has already been calculated in the VLM analysis. Step 8 is performed for the pressure-, and friction-drag coefficients separately, as their transformation from sweep-normal to freestream direction is different [42, 45]. This is shown in equation (8.5).

$$\left.\begin{aligned} C_{d_f} &= C_{d_{f_\perp}} \\ C_{d_p} &= C_{d_{p_\perp}} \cos^3 \Lambda \end{aligned}\right\} \qquad C_{d_{\text{prof}}} = C_{d_f} + C_{d_p} \tag{8.5}$$

Finally, the profile drag at the strips is integrated along the span using the trapezoidal rule. The sum of the integrated profile drag and the induced drag, calculated using VLM, yields the total wing drag. The implementation of Q3D introduces a few limitations on the tools applicability to certain cases. First, the use of the vortex lattice method for three-dimensional calculations limits the accuracy of the tool at high subsonic Mach numbers. As VLM is a surface singularity method, flow physics like shockwaves can not be captured. AVL[4] implements the Prandtl-Glauert compressibility correction to adjust lift- and drag values at higher Mach numbers. This correction loses validity for flows at Mach numbers above 0.8, and for flows where shocks are present. As the presence of shocks is more likely at higher freestream Mach numbers, the AVL user manual states that the correction can be expected to be valid for Mach numbers up to 0.7. Between 0.7 and 0.8, transonic flow is likely but not certain, meaning the correction is designated as being "suspect". Above freestream Mach numbers of 0.8 it can not be expected to be valid [63].

Given that the lift coefficients are found through the VLM, and are used as input to the sectional analyses, these lose accuracy as well. Furthermore, the application of the strip method on swept wings leads to three-dimensional boundary layer effects being ignored. On aft-swept wings, the boundary layer tends to move outward, decreasing boundary layer thickness on the inner part of the wing, and increasing boundary layer thickness on the outer part [64, 145]. As this is not taken into account in the two-dimensional aerodynamic analyses at the strips, the resulting force coefficients carry some inaccuracy, which is more pronounced for higher sweep angles. Despite these modeling errors, Mariëns [42] showed that the results of the program are accurate for straight to moderately swept wings, up to Mach numbers of around 0.8, for a fraction of the computational cost.

8.2. Tool Structure & Methodology

The present section will detail the methodology behind the Aircraft Trimmed Performance Analysis Tool, as well as the program's structure. A flowchart of the program is shown in Figure 8.3. This section will present the steps taken in the program in the order in which they appear in this chart. To start, ATPAT requires the user to enter the aircraft's geometry. Where Q3D only requires the wing geometry, a horizontal stabilizer definition and center of mass location should be entered into ATPAT. The horizontal tail definition should include a control surface definition, which is used in the internal trimming module of AVL. Optionally, the user can enter definitions for the location of the engines, and for the geometry of the fuselage. If entered, the effect of the thrust of the engines on the overall moment, and the fuselage

[4] https://web.mit.edu/drela/Public/web/avl/, accessed 14-5-2026

aerodynamic moment- and drag taken into account. ATPAT estimates the aerodynamic characteristics of the fuselage according to the method proposed by Nicolosi *et al.* [65]. An example input file is presented in Appendix A. It is worth noting that ATPAT is also integrated into the Initiator toolbox. In this version, the tool automatically finds the required data from an Aircraft object, omitting the need for manual inputs. Nevertheless, the input file provides a good overview of the data required to run the program.

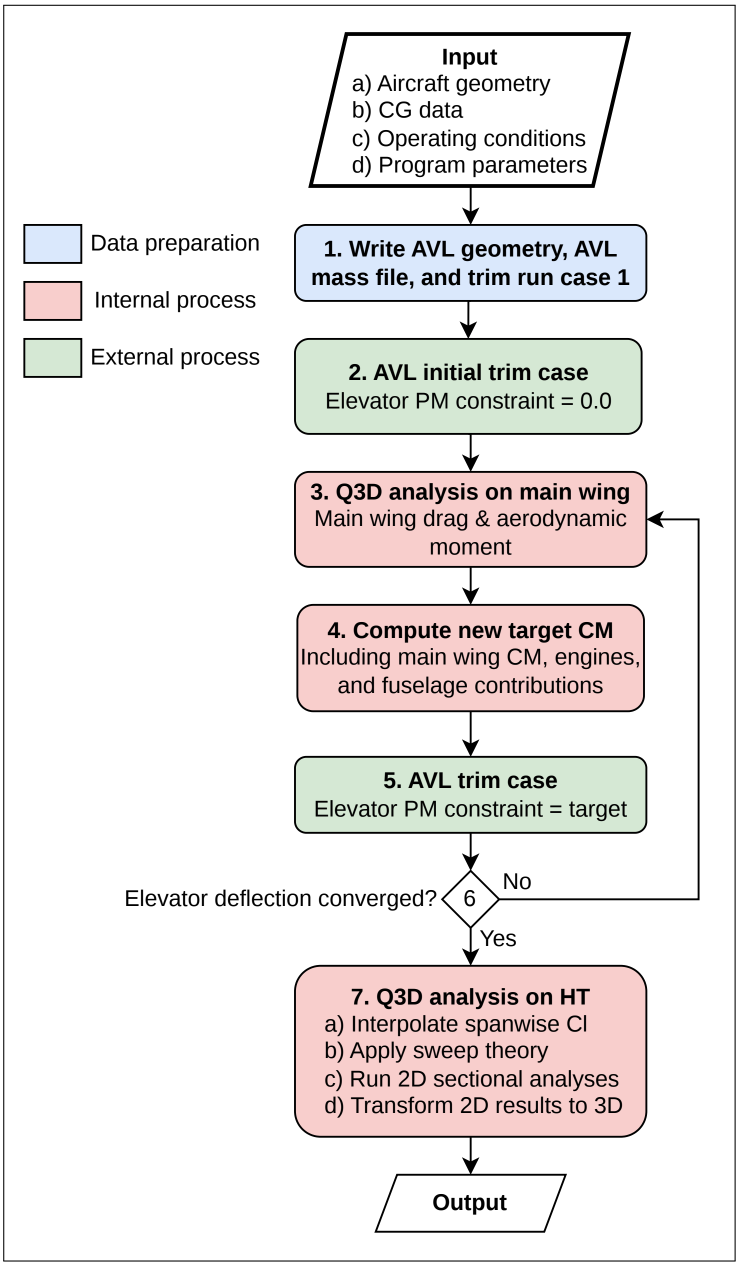

Figure 8.3: Flowchart of ATPAT

Step 1 & 2: AVL setup & analysis

The first step in ATPAT consists of generating the AVL input geometry. This geometry is used in all AVL analyses in the execution of ATPAT. Immediately, there is a big difference in this step compared to Q3D. Since the result of interest in Q3D is the wing drag, only the part of the wing exposed to the flow is modeled. In ATPAT, however, a simplified representation of the entire aircraft is used, meaning the part of the wing that sits inside of the fuselage has to be modeled as well. If this part is included in the input geometry as is, AVL significantly overpredicts the Oswald efficiency factor as the lift distribution is smoothly continues over the part where the fuselage would normally be. This leads to an underprediction of induced drag. Figure 8.4 illustrates the effect of the fuselage on the lift distribution in reality. Some lift is present on the fuselage, and the lift over the wing-fuselage intersection is slightly higher than it would be for a continuous wing.

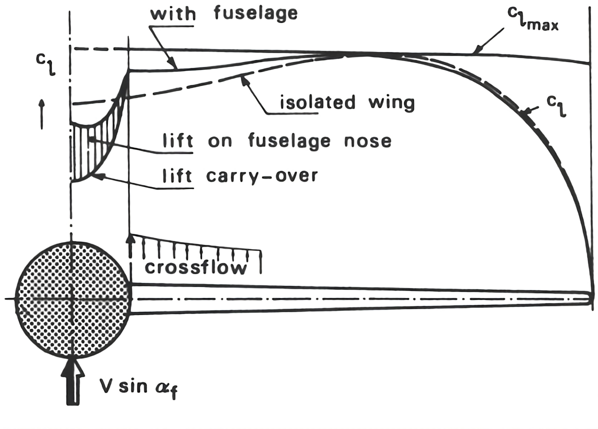

Figure 8.4: Fuselage effect on the lift distribution [11, 478]

ATPAT was found to be most accurate when applying the AVL keyword "**NOLOAD**" to the part of the wing in the fuselage. With the keyword applied, the forces over this part of the wing are not taken into account, meaning the required lift has to be generated over the part of the wing that is exposed to the flow. The lift distribution does behave like it would if the keyword would not be applied, only the effective area of the wing is lower. Using the functionalities within AVL, this is the best approximation for the real situation illustrated above. The implication of this will further be discussed along with the verification and validation of the tool in section 8.3. An illustration of the exclusion of this part of the wing, along with the strip placements, is shown in Figure 8.5. After the wing and horizontal tail geometry are written, the first AVL case is set up. For this initial run, the target total pitching moment coefficient is set to $C_M = 0.0$, for which AVL uses the elevator control surface defined on the horizontal tail in its internal trimming module. If the user defined a fuselage and engines, they are not taken into account in the initial run, as the angle of attack and total drag of the aircraft are required to calculate their contributions to the overall moment.

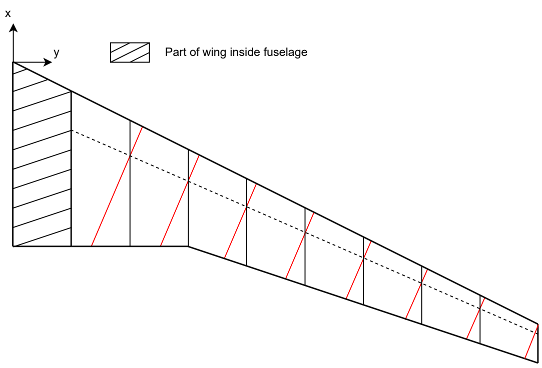

Figure 8.5: Part of the wing inside the fuselage modeled with 'NOLOAD' and strip placement

Step 3: Q3D analysis on Main Wing

In step three, a Q3D analysis is performed on the main wing with the lift distribution found from the initial AVL run. This is done according to the methodology laid out in section 8.1. Aside from calculating the wing drag, the aerodynamic moment generated by the main wing has to be calculated for the next trim iteration. AVL calculates the aerodynamic moment of the main wing internally, but this has to be corrected as VLM works with zero-thickness surfaces and does not model viscous effects. For the calculation of the quasi-three-dimensional aerodynamic moment, it is split up into contributions by sectional aerodynamic moments at the strips, found through the two-dimensional airfoil analyses, and the contributions of lift and drag. As the sectional aerodynamic moments are pure moments, their location with respect to the reference point is of no importance. Therefore, this contribution is calculated using the same trapezoidal integration as for lift and drag in Q3D, after transforming the sectional aerodynamic moments from around the representative sweep line to around the y-axis. This transformation is done using the relation in equation (8.6) [66, 431]. The trapezoidal integration is shown in equation (8.7), in which the subscript j represents the j-th section contained by two strips, where $1 \leq j \leq N_{strips} - 1$.

$$C_{m_{stream}} = \frac{C_{m_\perp}}{\cos^2 \Lambda} \tag{8.6}$$

$$C_{M_{m2d,j}} = \left(C_{m_j}\bar{c}_j^2 + C_{m_{j+1}}\bar{c}_{j+1}^2\right)\frac{y_{j+1} - y_j}{2} \tag{8.7}$$

The contributions of lift and drag are calculated at the mid-point along the sweep line between two strips. This is illustrated in Figure 8.6, where the Xs mark the locations of these mid-points.

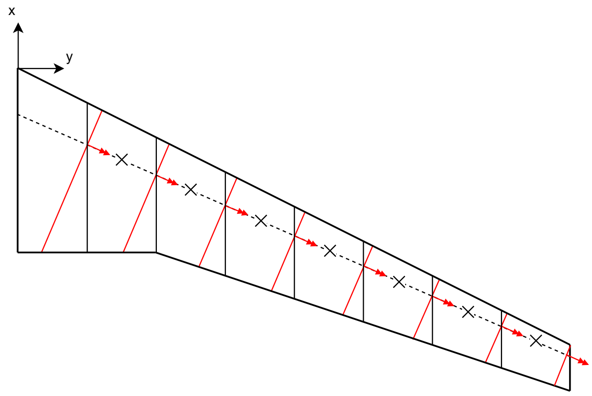

Figure 8.6: Relevant locations for Q3D aerodynamic moment calculation

The quasi-three-dimensional aerodynamic moment generated by the main wing can now be calculated using equation (8.8).

$$C_M = \sum_{j=1}^{N_{strip}-1}\left(C_{M_{m2d,j}} + C_{L_j}\left(x_{ref} - x_{mid,j}\right) - C_{D_j}\left(z_{ref} - z_{mid,j}\right)\right) \tag{8.8}$$

Step 4: Computing a new target moment coefficient

After the quasi-three-dimensional aerodynamic moment generated by the main wing has been determined, a new target pitching moment coefficient can be calculated for use in the next AVL iteration. Using the angle of attack found in the preceding AVL run, as well as the current estimate of the total drag, the contributions of the engines and fuselage to the overall moment can be calculated and are taken into account. For the calculation of the aerodynamic moment generated by the fuselage, the method by Nicolosi *et al.* [65] is used. A linear relationship between the aerodynamic moment and the fuselage angle of attack α_{fus} is assumed, as shown in equation (8.9). For details about the calculation of $C_{M_{0_{fus}}}$ and $C_{M_{\alpha_{fus}}}$, the reader is referred to the original paper.

$$C_{M_{fus}} = C_{M_{0_{fus}}} + \alpha_{fus} C_{M_{\alpha_{fus}}} \tag{8.9}$$

The contribution of the engines to the overall moment is based on the assumption of steady, level, and straight flight. In this flight condition, the overall force balance in equation (8.10) applies. In this equation, α is the aircraft angle of attack and i_e is the incidence angle of the engines w.r.t the aircraft reference frame.

$$\sum F_x \overset{+}{\leftarrow} = T\cos(\alpha + i_e) - D = 0 \tag{8.10a}$$

$$\sum F_z \uparrow^{+} = L + T\sin(\alpha + i_e) - W = 0 \tag{8.10b}$$

According to Raymer [28, 117], the thrust-to-weight ratio for transport aircraft is between 0.25 and 0.4. Furthermore, it is assumed that α in equation (8.10b) is small in the flight conditions of interest. Therefore, the vertical component of the thrust is ignored in the determination of the cruise lift coefficient which is used as input to AVL. The term is included in the horizontal force balance, as this was found to improve the accuracy of the overall moment prediction. The moment coefficient due to the engines is subsequently computed according to equation (8.11), under the assumption that the total thrust is divided equally over all engines. The total thrust is found through equation (8.12).

$$C_{M_e} = \frac{2T_{tot}}{\rho V_\infty^2 S_{ref} c_{ref}} \sum_{j=1}^{n_e} \left(\cos i_{e,j}\left(z_{ref} - z_{eng,j}\right) + \sin i_{e,j}\left(x_{ref} - x_{eng,j}\right)\right) \tag{8.11}$$

$$T_{tot} = \frac{D}{\cos(\alpha + i_e)} \tag{8.12}$$

The new target C_M for the next AVL iteration can now be computed. Because AVL computes the aerodynamic moment of the thin surface representation of the wing internally, the difference between the AVL value and the Q3D value found in step three has to be used. At positive angles of attack, thin surface representations are expected to generate stronger and more concentrated suction peaks compared to real surfaces as a result of the flow turning more sharply. Therefore, it is expected that the moment of the main wing computed internally in AVL is more nose-up than the quasi-three-dimensional value. The target moment coefficient compensates for this by instructing AVL to trim for a more positive total moment coefficient. The new target C_M is computed according to equation (8.13).

$$C_{M_{target}} = C_{M_{mw,AVL}} - C_{M_{mw,Q3D}} - C_{M_{fus}} - C_{M_{eng}} \tag{8.13}$$

Step 5, 6 & 7: Iteration and final results

Steps three, four, and five are repeated until the elevator deflection that is returned by AVL in step five converges to within a specified tolerance. After it has converged, a Q3D analysis is run on the horizontal tail. The fact that this happens outside of the iterative loop means that the quasi-three-dimensional drag and aerodynamic moment generated by the horizontal tail are not taken into account. These contributions, however, are small, and are often neglected in stability calculations [11, 308]. The trimmed drag coefficient is now found as the sum of the fuselage drag coefficient, found through the method by Nicolosi *et al.* [65], and the quasi-three-dimensional wing and horizontal tail drag coefficients. If desired, a miscellaneous drag coefficient can be entered before running the program. Using this, the program can account for drag due to excrescences, interference effects, and non-modeled components. The lift-, drag-, and moment-coefficients of the main wing, horizontal tail, and fuselage are outputted as well.

8.3. Verification & Validation

In this section, the verification and validation of ATPAT will be presented. First, the implementation of quasi-three-dimensional aerodynamic analysis is verified by comparing the results of the tool to the output of the original Q3D by Mariëns [42]. The validation of the program consists of a comparison between the results of the tool and experimental data, documented by Obert [64]. The aircraft geometry used in both the verification and validation steps is that of the Fokker 100. This aircraft has been selected due to the ample availability of data for validation, and the fact that Mariëns [42] used this geometry to validate Q3D at high speeds. The external dimensions of the aircraft[5] and the wing-planform

[5] https://fokkerservicesgroup.com/media/emccsdnm/fsg_fokker-100.pdf, accessed 15-5-2026

geometry used as input are shown in Figure 8.7 and Figure 8.8 respectively. Small deviations from reality may occur due to measurement errors as a result of the limited availability of geometry data. The verification will be documented in subsection 8.3.1, followed by the validation in subsection 8.3.2.

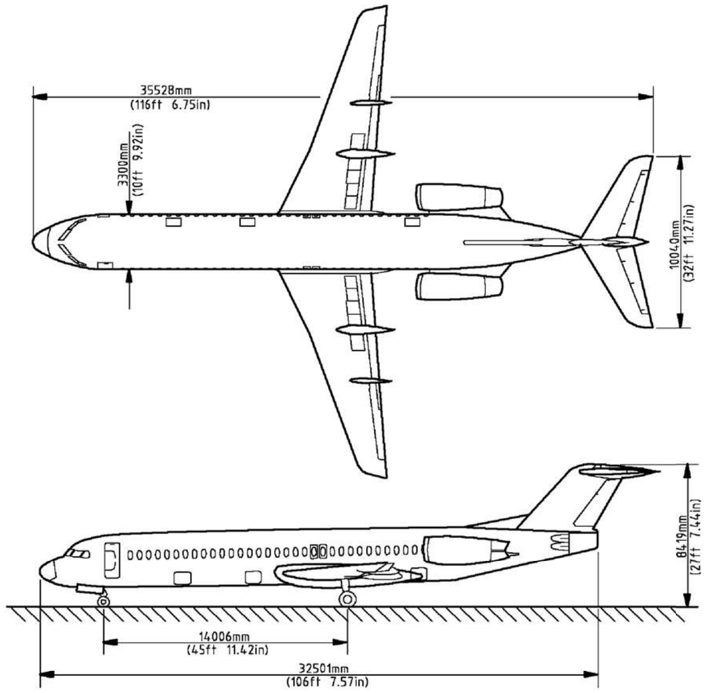

Figure 8.7: Fokker 100 external dimensions

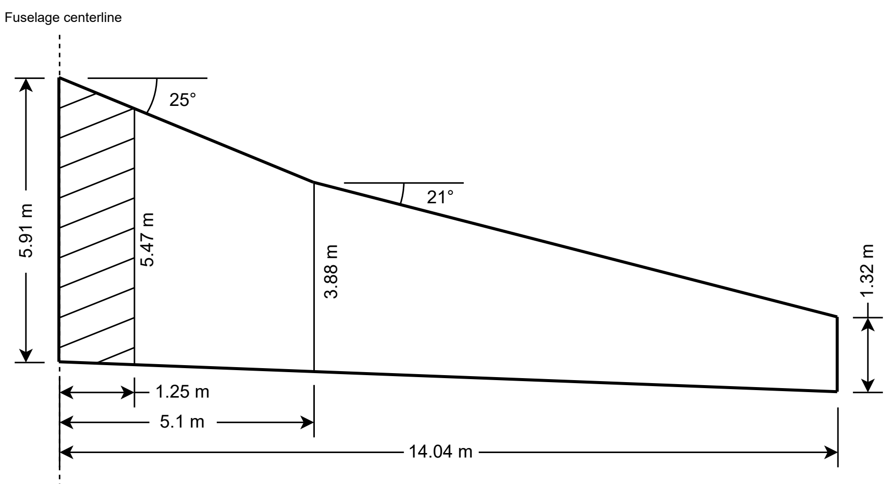

Figure 8.8: Fokker 100 wing planform geometry

8.3.1. Verification

The present subsection will present three cases for verifying the correct implementation of quasi-three-dimensional aerodynamic analysis in ATPAT. The results generated for the main wing by ATPAT will be compared against results from Q3D. Importantly, ATPAT takes the trimmed overall lift coefficient as an input, where Q3D takes the wing lift coefficient. The verification cases are defined for trimmed lift coefficients, which are first used as input to ATPAT, after which the resulting main wing lift coefficient from ATPAT is used as input to Q3D. The verification cases are summarized in Table 8.1.

Table 8.1: ATPAT verification cases - Fokker 100 geometry

Case nr.	**h** [m]	$\mathbf{M_\infty}$ [-]	$\mathbf{C_{L_{trim}}}$ [-]	**Verification data**
1	3048.0	0.38	$0.05 \leq C_{L_{trim}} \leq 1.0$	Drag polar
2	10972.8	0.7	0.45	Lift distribution
3	10972.8	$0.5 \leq M_\infty \leq 0.77$	0.45	Drag versus Mach number

Case 1

The low-speed main wing drag polars for the Fokker 100 geometry calculated by both ATPAT and Q3D are shown in Figure 8.9. The solvers are in good agreement. At high lift coefficients, ATPAT predicts a slightly lower drag coefficient. The reason for this will be discussed with the high-speed verification case, as the effect is more noticeable there.

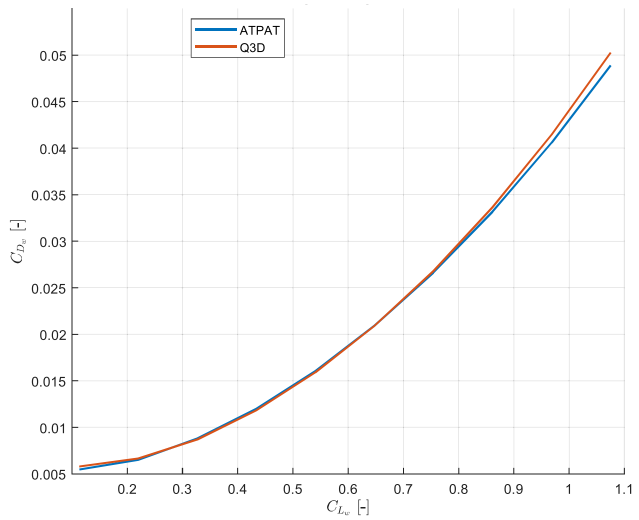

Figure 8.9: Fokker 100 main wing lift-drag polar, $M = 0.38$, $h = 3048.0\,\mathrm{m}$

Case 2

The lift distributions over the main wing predicted by both tools at a trimmed lift coefficient of 0.45, resulting in a main wing lift coefficient of 0.5677, are shown in Figure 8.10.

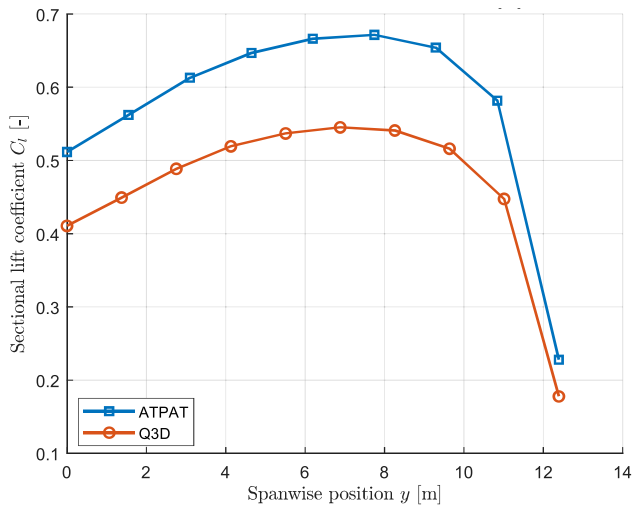

Figure 8.10: Comparison of lift distribution over Fokker 100 wing $M = 0.7$, $h = 10\,972.8\,\mathrm{m}$, fuselage modeling turned on

The sectional lift coefficients found in the trimmed performance analysis tool are consistently higher than those calculated in Q3D. This is due to the exclusion of the part of the wing in the fuselage from the overall forces. Given that the wings produce the same lift coefficient, and that the wing reference area is the same, more lift has to be generated on the part with loads in ATPAT. When the option for fuselage modeling is turned off, the lift distributions returned by both programs are in good agreement. This is shown in Figure 8.11. The difference in results is hence a product of differing modeling techniques. For the overall aircraft level, the best results were found with the fuselage modeling, as will be detailed in subsection 8.3.2.

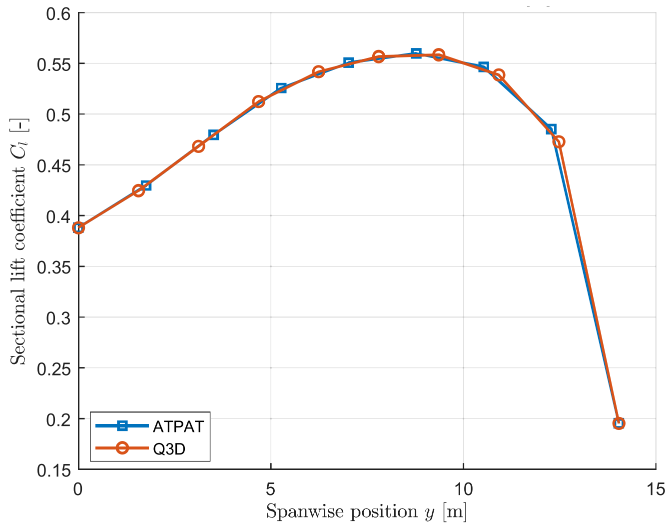

Figure 8.11: Comparison of lift distribution over Fokker 100 wing $M = 0.7$, $h = 10\,972.8\,\mathrm{m}$, fuselage modeling turned off

Case 3

In Figure 8.12, the main wing drag coefficient is plotted as a function of the freestream Mach number. The decrease in drag coefficient between $M_\infty = 0.75$ and $M_\infty = 0.77$ for both solvers is due to VGK not converging for all of the strips. Q3D and ATPAT both fall back to interpolation of the values at the strips that did converge, but this introduces an error.

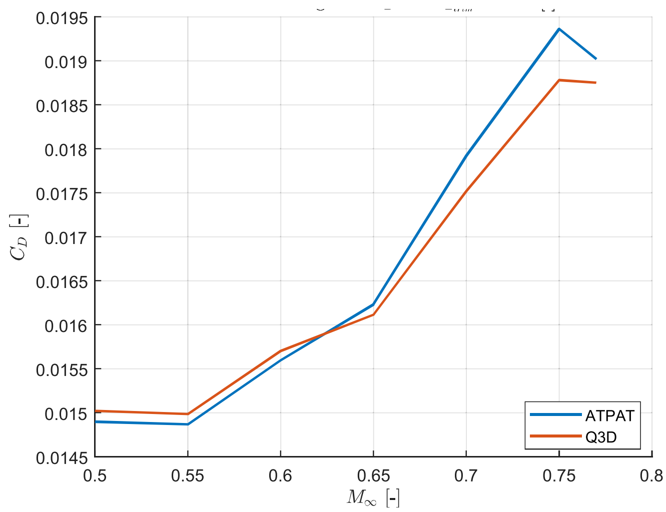

Figure 8.12: Fokker 100 main wing C_D versus M_∞, $h = 10\,972.8\,\mathrm{m}$

For the high-speed case, both solvers agree reasonably well, but less so than for the other two verification cases. Analysis of the Q3D source code revealed that the wing twist distribution is not taken into account when deriving the sections perpendicular to the sweep line. ATPAT corrects for this. Therefore, slight differences in airfoil sections throughout the wing arise. For the high-speed case, this is more noticeable in the results. At high speeds, VGK is used as the two-dimensional solver. At low speeds, Xfoil is used. VGK was found to be more sensitive than Xfoil for changes in geometry and operating conditions. The derived perpendicular sections of both solvers are shown in Figure 8.13.

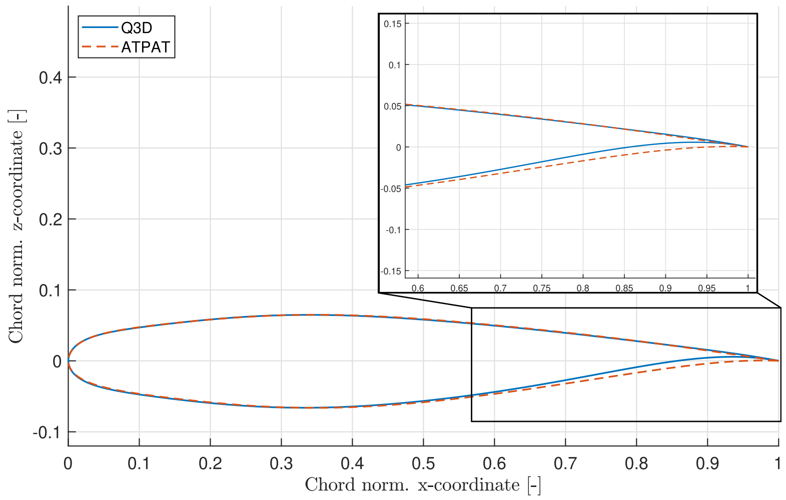

Figure 8.13: Comparison of derived section on strip 2 of 8 on Fokker 100 wing

Concluding this subsection on the verification of the implementation of quasi-three-dimensional aerodynamic analysis in ATPAT, it was shown that both solvers are in good agreement on three distinct cases. The differences in results between the two solvers can be attributed to modeling choices, and improvements over the original code, meaning the correct implementation of quasi-three-dimensional aerodynamic analysis is verified.

8.3.2. Validation

In this subsection, the validation of ATPAT against data on the Fokker 100 will be documented. The data is sourced from Obert [64], who collected data from Fokker reports in his book "Aerodynamic Design of Transport Aircraft". The cases considered in the validation of the tool are summarized in Table 8.2.

Table 8.2: Trimmed performance analysis tool validation cases - Fokker 100 geometry

Case	h [m]	M_∞ [-]	C_L [-]	C.G. position	Validation data
1	1828.8	0.3	$0.0 \leq C_L \leq 1.0$	7% MAC	Drag polar, Tail-off moment curve
2	1828.8	0.3	$0.0 \leq C_L \leq 1.0$	30% MAC	Tail-off moment curve
3	9144.0	$0.6 \leq M_\infty \leq 0.77$	0.3, 0.4, 0.5	7% MAC	Drag versus Mach number

Because the data of the solver is compared to experimental data, forced boundary layer transition at 5% of the chord was used in the two-dimensional solvers to model the effect of surface imperfections on the actual wing on boundary layer transitions. Furthermore, a miscellaneous drag coefficient was included to account for parts not present in the ATPAT analysis. The computation of this value is presented in Table 8.3, and is based on data by Obert [64].

Table 8.3: Drag factors unaccounted for in ATPAT, reproduced from Obert [64, 537]

Components	$\mathbf{S_{wet}}$ $[\mathrm{m}^2]$	**Shape factor** λ [-]	$\mathbf{C_f} \times 10^4$ [-]	$\mathbf{C_D} \times 10^4$ [-]
Nacelles	46.18	1.226	27.1	16.4
Stub wings	5.68	1.217	27.1	2.0
Boundary layer fences	1.48	1.000	34.0	0.6
Flap track fairings	7.96	1.104	24.5	2.3
Anti-shock body	0.48	1.126	23.0	0.1
Vertical tailplane	31.56	1.201	27.1	11.0
excrescences:	Size-dependent	0.07×171.5		12.0
	Size-independent	$\Delta D/q = 0.40\,\mathrm{m}^2$		4.3
Total				48.7

Case 1

For the first validation case, the results from ATPAT are compared to the experimental low-speed drag polar and tail-off pitching moment curve for a center of mass position at 7% of the mean aerodynamic chord (MAC). The computed and measured drag polars are presented in Figure 8.14, which shows the polars being in good agreement. The ATPAT result shows a slightly more parabolic drag polar. This is a result of the exclusion of the forces over the part of the wing inside of the fuselage from the overall forces. Because of it, the lift is underpredicted at high angles of attack and overpredicted at low angles of attack, causing AVL to return higher or lower angles of attack respectively, slightly narrowing the drag polar. Nevertheless, the discrepancy between the calculated and measured data remains within 2.5 drag counts over the entirety of the polar.

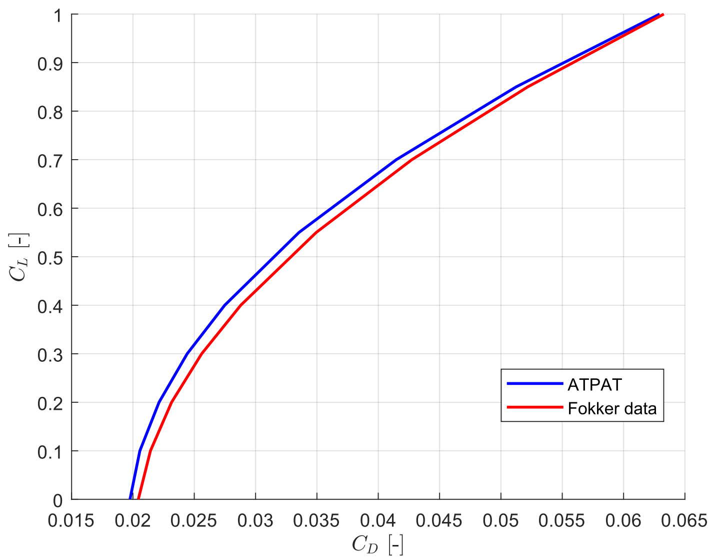

Figure 8.14: Fokker 100 low speed drag polar comparison with flight test data, CG at 7% MAC

Figure 8.15 presents the comparison between the tail-off pitching moment curve computed by ATPAT, and by Fokker's Non-Planar Lifting Surface (NPLS) code. ATPAT predicts a more negative pitching moment coefficient at low lift coefficients, and a more positive pitching moment coefficient at high lift coefficients. Again, this can be attributed to the fuselage modeling method. At low lift coefficients, the overall angle of attack is more negative than it would be in practice. Because of the linear model for the fuselage pitching moment, the overall pitching moment coefficient is predicted to be more negative. At high angles of attack, this is reversed, causing ATPAT to overestimate the pitching moment coefficient. Furthermore, the curve predicted by ATPAT is not fully straight. This has to do with the moment generated by the engines. The total thrust is corrected for the angle of attack, which causes the contribution of the engines to be non-linear. Nevertheless, the discrepancy between ATPAT and NPLS remains at $\pm 0.2 C_{M_{to}}$ at lift coefficients between 0.2 and 0.6, which represents a realistic band of lift coefficients in cruise.

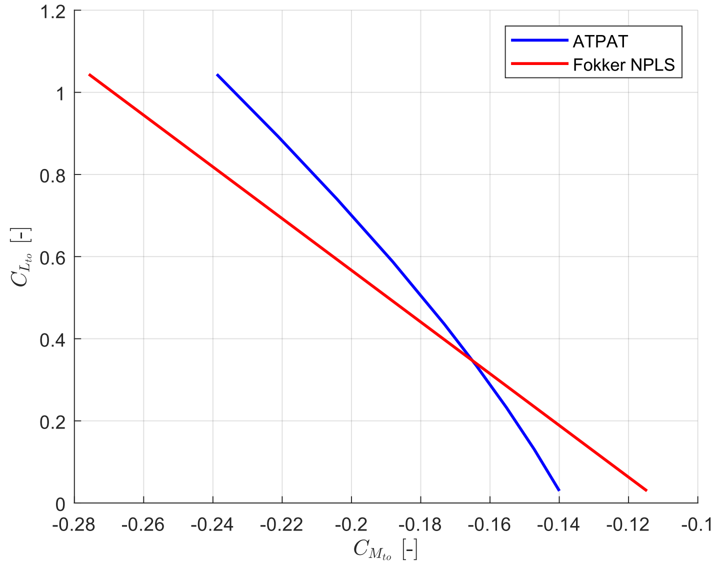

Figure 8.15: Comparison of the prediction of the Fokker 100 tail-off pitching moment curve computed by ATPAT and NPLS

Evidently, some discrepancy is introduced due to the fuselage modeling. Out of the possibilities available, however, this method does give the best results. To further motivate this, the same validation cases were ran where the the part of the wing inside the fuselage was assumed to account for the aerodynamic drag- and moment of the fuselage. This did not yield more accurate results, as shown in Figure 8.16.

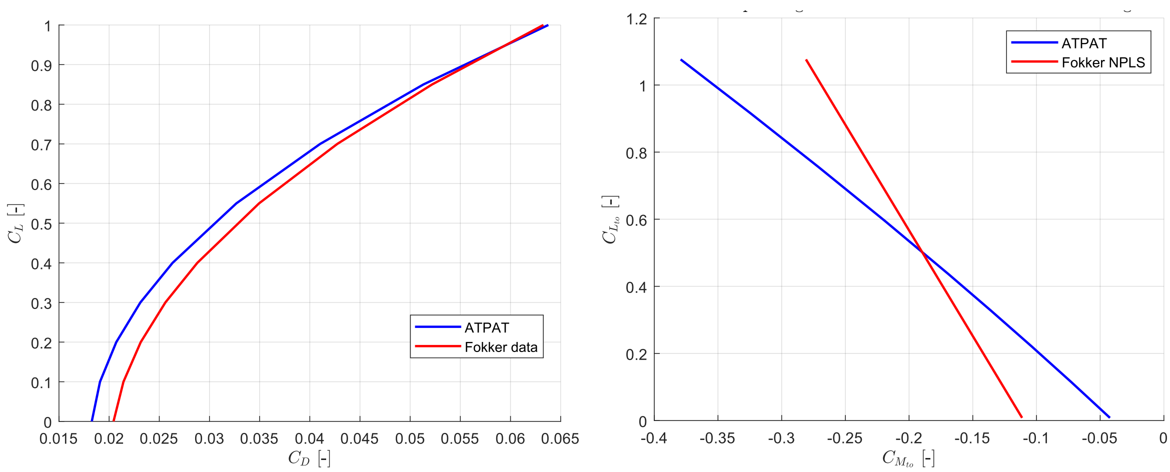

(a) Fokker 100 Low speed drag polar, CG 7% MAC

(b) Fokker 100 tail-off pitching moment curve, CG 7% MAC

Figure 8.16: Drag polar and tail off pitching moment curve for different method of fuselage modeling in ATPAT

Case 2

The tail-off pitching moment curve calculated for a center of mass position at 30% of the mean aerodynamic chord was also compared to Fokker NPLS data. The result of which is shown in Figure 8.17. The same behavior as in validation case 1 is observed, where ATPAT predicts a more nose-down moment at low lift coefficients and a more nose-up moment at high lift coefficients. Within the expected range of cruise lift coefficients, the error remains within $\pm 0.25 C_{m_{to}}$. The results of case 1 and case 2 confirm that ATPAT correctly predicts the sign of the derivative of the pitching moment coefficient with respect to the lift coefficient. No drag data was found for comparison for which the center of gravity location is 30% of the mean aerodynamic chord.

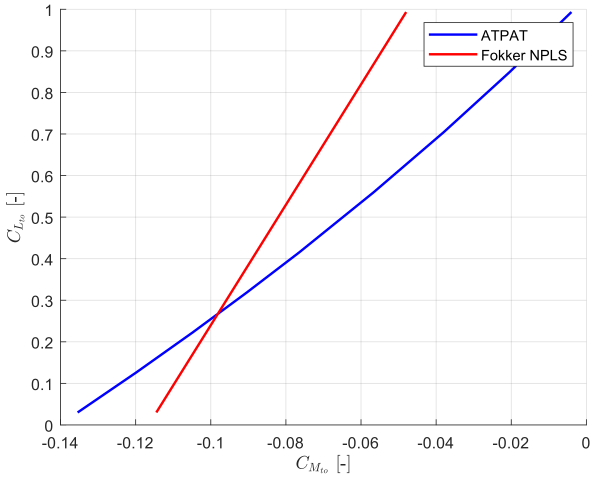

Figure 8.17: Comparison of predicted Fokker 100 tail-off pitching moment curves with the CG at 30% MAC by ATPAT and NPLS

Case 3

Validation case 3 consists a comparison of the high speed drag prediction of ATPAT with experimental data. The results of the comparison are shown in Figure 8.18. The ATPAT results are generally in good agreement with the experimental data. At the highest Mach numbers tested, ATPAT overpredicts drag. As discussed in section 8.1, the Prandtl-Glauert compressibility correction is only valid in flows where shocks are not present. For the lower two lift coefficients, the maximum Mach number tested is the maximum operating Mach number of the Fokker 100, for the highest lift coefficient, it is the buffet onset Mach number. Since shocks are very likely to be present in these conditions, the correction is no longer valid. As the AVL results are used as input to the sectional analyses, these results also carry some error. On top of this, the experimental data includes effects of surface flexibility, which is not present in the ATPAT results.

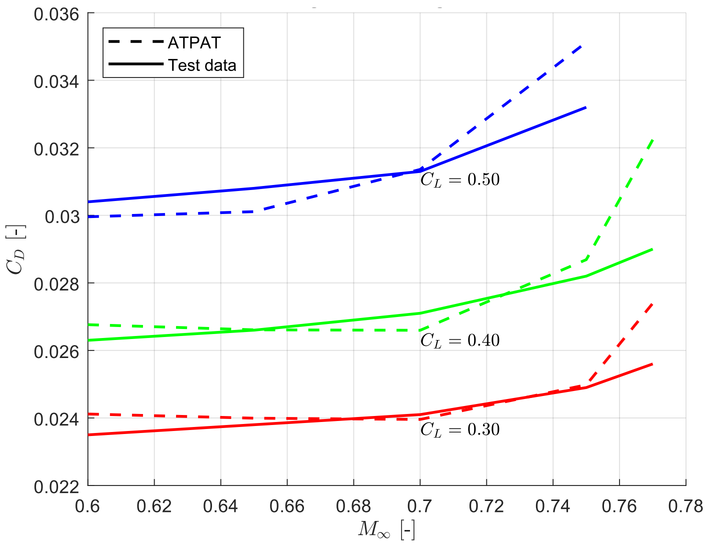

Figure 8.18: Fokker 100 C_D as a function of M_∞, CG 7% MAC, comparison of ATPAT to test data

This section has shown that ATPAT produces accurate enough results to be used within the context of conceptual design, and that discrepancies between higher-order methods and reality can be explained due to modeling choices. The runtime of the program is 30 seconds or less when run in MATLAB R2024b on an HP ZBook Studio G5 from 2020, with an Intel i7-9750H CPU, making its use within optimization loops feasible. The requirements that were laid out in chapter 4 are therefore all met.

8.4. Integration in Initiator

Since the first version of ATPAT, the tool has been fully integrated into the aircraft design Initiator toolbox, which was introduced in section 3.2, as an analysis module. It can be employed for conventional aircraft as a rapid but accurate drag estimation tool, and it can be used for the optimization of the shape of morphing wings in the cruise condition. Two optimization techniques have been incorporated in the ATPAT analysis module: Bayesian optimization, using MATLAB's **bayesopt**, and gradient-based optimization using **fminunc**. As introduced in section 4.2, Bayesian optimization works well for expensive black-box solvers if the dimensionality of the design space is low, preferably twenty design variables or less. The parametrization technique used for morphing, introduced in chapter 7, can model wing morphing using two pseudo-deflections per spanwise station. Therefore, up to 10 spanwise stations can be defined while adhering to the twenty variables.

Even though an adjoint formulation of Q3D, upon which ATPAT is based, has been developed [67], this was not considered for ATPAT due to time constraints. Therefore, gradient-based optimization using ATPAT requires finite differences to estimate the gradient of the overall aircraft drag with respect to the pseudo-deflections at the spanwise stations. As introduced in section 4.2, this is both expensive and prone to error. Hence, Bayesian optimization is the preferred method for the morphed wing shape optimization. The use of Bayesian optimization has the additional advantage that it is a global optimization method, and thus not susceptible to getting caught in local minima.

9

Sizing of aircraft with morphing wings

The present chapter will detail the adopted sizing methodology for aircraft with compliant morphing trailing edge wings. Various steps of the conceptual aircraft design process, along with their applicability to aircraft with morphing wings, were discussed in chapter 3. The uncertainty in the weight prediction of morphing wings due to the absence of empirical data on full-size structures of this type was one of the findings in that chapter. Therefore, section 9.1 will present an estimation method for the structural weight of morphing wings. The aircraft design Initiator is used as the primary tool for the sizing studies. The extension of the toolbox to enable the sizing of morphing wing aircraft will therefore be detailed in section 9.2. The sizing workflow that is adopted using these extensions is motivated in section 9.3.

9.1. Weight estimation of morphing wing aircraft

The present section will introduce a method for estimating the structural mass of morphing wings based on a parametric specific morphing system mass in $\mathrm{kg\,m^{-2}}$. An important first note to make is that mass estimation is usually referred to as weight estimation in literature. To align the relations presented in this section with those in literature, weight estimation refers to mass estimation throughout this section. The estimation method is designed to be integrated with the Class 2 weight estimation, and is based on the structural wing weight estimation by Torenbeek [11]. In this method, the structural weight is split up into a basic wing weight, which is the weight of the structure required to resist the bending moment due to lift at a critical flight condition, and the contribution of high-lift devices and spoilers. The same approach will be taken in the morphing wing weight estimation, only now the weight of trailing edge high-lift devices is replaced with the weight of the morphing system. This breakdown is shown in equation (9.1). The 1.2 factor for the leading edge high-lift devices and spoilers is adapted from Torenbeek [11]. This is not applied to the morphing system, as it is an integral part of the wing structure, not a separate surface.

$$W_W = W_{W_{basic}} + W_{morphing} + 1.2\left(W_{hld,LE} + W_{sp}\right) \tag{9.1}$$

The basic wing weight is found according to equation (9.2), shown here for completeness despite being introduced in subsection 3.1.4. For the definition of the terms in this equation, the reader is referred to Torenbeek [11].

$$\begin{aligned} W_{W_{basic}} = 8.94 \times 10^{-4} \times k_{no}k_{\lambda}k_{e}k_{uc}k_{st} \times \left[k_b n_{ult}\left(W_{des} - 0.8W_W\right)\right]^{0.55} \times \\ b^{1.675}(t/c)_r^{-0.45}\left(\cos\Lambda_{1/2}\right)^{-1.325} \end{aligned} \tag{9.2}$$

Importantly, the calculation of the basic wing mass requires an initial estimate for the total wing weight W_W, as can be seen above. Torenbeek [11] suggests to use the relation in equation (9.3).

$$\frac{W_W}{W_G} = k_W b_s^{0.75}\left(1+\sqrt{\frac{b_{ref}}{b_s}}\right) n_{ult}^{0.55}\left(\frac{b_s S}{W_G t_r}\right)^{0.30} \tag{9.3}$$

The estimation for the wing structural weight presented above includes the weight of high-lift devices and spoilers. This introduces a problem, as that is exactly what this method tries to avoid. In the absence of alternatives, however, it is used as a starting point for an iterative estimation, which is illustrated in Figure 9.1. The weights of the leading edge high-lift devices and spoilers are estimated using specific weights, similar to the morphing system weight. For the leading edge high-lift devices, Torenbeek [11, 454] presents a relation between the specific mass of these devices and the maximum take-off weight in logarithmic space. For the spoilers, he proposes a value of $12.2\,\mathrm{kg\,m^{-2}}$. The areas of the leading edge devices and spoilers are assumed to be 15% and 6% of the planform area respectively, in line with assumptions made in the Class 2.5 method for wing weight estimation integrated in the Initiator.

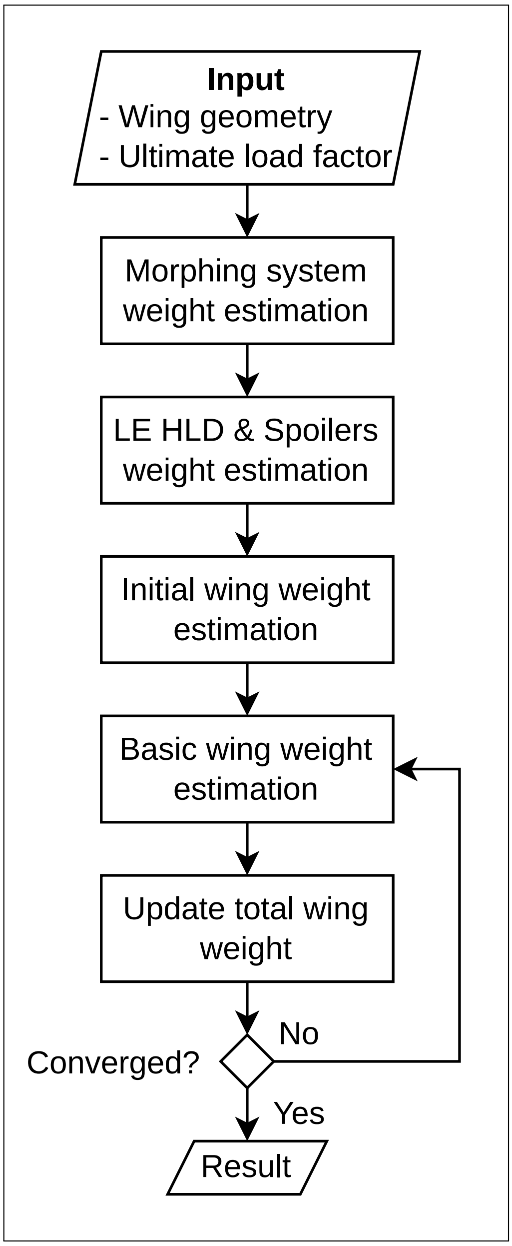

Figure 9.1: Iterative Class 2 method for morphing wing structural weight estimation

9.2. Integration of morphing wings in the Initiator

This section will detail the integration of morphing wings into the aircraft design Initiator, which was introduced in section 3.2. The tool has been developed using object-oriented programming (OOP), which means that the code is organized around objects that encapsulate both data storage and functionality. Each of these objects is an instance of a class, which acts as a blueprint defining what data and functionalities are shared by its instances. In the Initiator, all information pertaining to aircraft geometry, requirements, performance parameters, and configuration parameters is stored in an instance of the **Aircraft** class. The geometry information is captured in objects that are held in the 'Parts' attribute of the aircraft class. The objects populating this attribute are all instances of classes which are specializations of the abstract superclass ***Part***. Examples of these objects are the main wing and horizontal tail, which are both instances of the **Wing** class, and the engines which are all instances of the **Engine** class. For the work in this thesis, the classes **MorphingAirfoil** and **MorphingWing** have been added to the Initiator as specializations of **Airfoil** and **Wing** respectively. In this manner, morphing-specific logic is contained in the specialized classes while general logic pertaining to the airfoil and wing can be used in both the standard and morphing variants. Examples of general logic are the calculation of the chord for airfoils, and the calculation of the planform area for wings. The sections property of the wing class holds a number of airfoil instances. The airfoils, positioned along the span, together model the three-dimensional wing geometry. This is the same for the morphing wing class, only now the sections property is populated with morphing airfoil instances, which matches the parametrization method introduced in chapter 7. The relations between the various classes are shown in the class diagram in Figure 9.2.

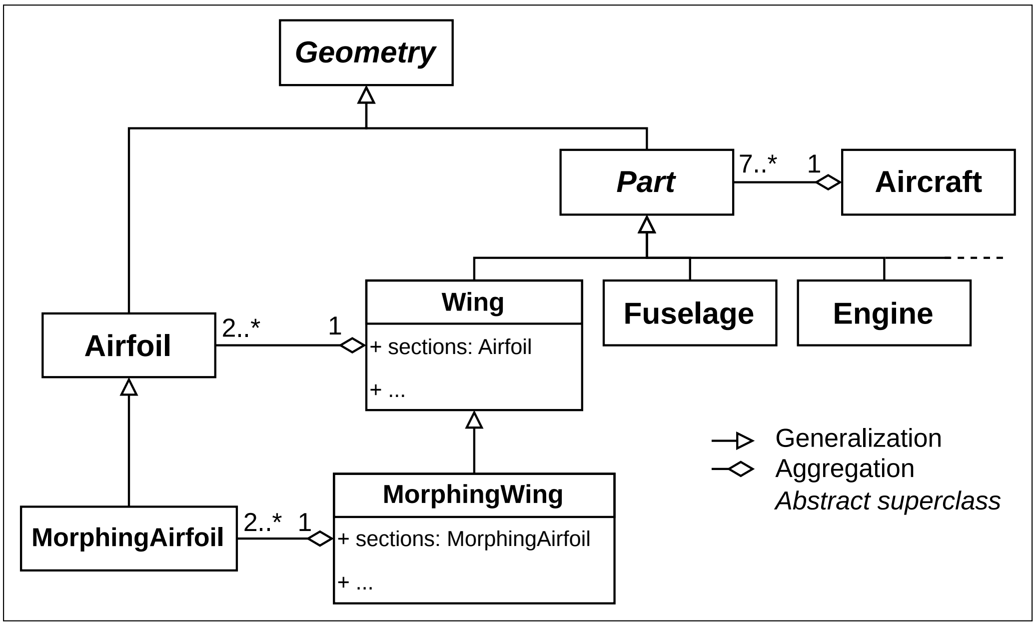

Figure 9.2: UML diagram illustrating the integration of the classes **MorphingAirfoil** and **MorphingWing** in the Initiator. The dashed line connected to ***Part*** indicates that there are more specializations of the abstract superclass which are not all shown here.

9.3. Sizing workflow in Initiator

The standard sizing workflow in the Initiator is called 'DesignConvergence', which takes geometry inputs, regulations, and program settings as input and iteratively generates an aircraft design. The core of this workflow is the 'ConvergeWeights' function, which consists of three core loops, as illustrated in Figure 9.3. The inner loop comprises of the Class 1 and Class 2 weight and performance estimations, and the wing area and thrust sizing. Once this converges, the program enters the middle loop, which contains the high-lift system sizing, horizontal stability estimation and tail sizing, and the mission analysis modules. Upon convergence of the inner and middle loop, the outer loop is run. This contains Class 2.5 methods, which combine empirical estimations with physics based methods.

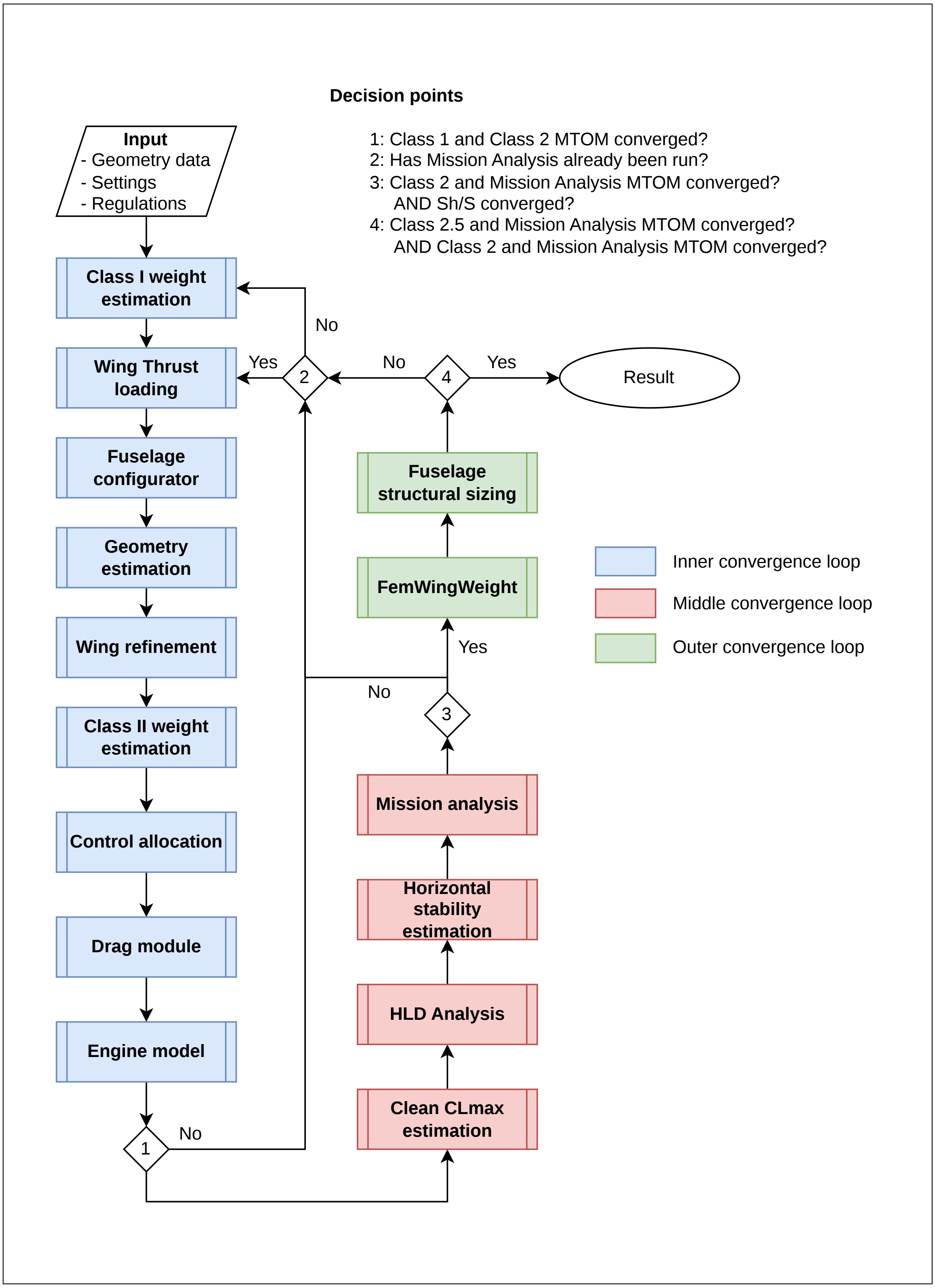

Figure 9.3: Flowchart of the 'ConvergeWeights' function in the Initiator

The sizing studies in the present thesis primarily use the inner loop in the 'ConvergeWeights' function. During preliminary testing, the Class 2.5 methods in the outer loop were found to produce inconsistent results compared to the Class 1 and 2 methods in the inner loop. Although some discrepancy is to be expected, the difference between the inner and outer loop weight estimations was in the order of metric tons when tested on a regional turboprop similar to the ATR 72-600.

The integration of morphing wings into the middle loop was found to be challenging due to the reliance of the clean maximum lift coefficient estimation and the horizontal stability estimation on externally defined processes, much of which come from ESDU[1]. Furthermore, the high-lift device (HLD) analysis in the middle loop is not applicable to morphing wings. This module checks whether there is sufficient space available on the trailing edge for a high-lift system that enables the aircraft to generate the take-off and landing maximum lift coefficients used as input to the program. The high-lift study in combination with the relations presented in chapter 3 provide a physically motivated estimate for the input maximum lift coefficients, rendering this step redundant. On top of this, the results of the Initiator with inclusion of the middle loop are reasonably close to those of the inner loop only. This is illustrated in Figure 9.4, in which the inner loop converges for the first time after four iterations. The change in MTOM after this point can be mostly attributed to the mission analysis predicting a different fuel weight, rather than the structural weight changing significantly.

Finally, the present study is concerned with comparing the sizing results and performance of aircraft with morphing wings to conventional counterparts. Discrepancies with reality in the results due to the use of the inner loop only will be present in the results for both aircraft, meaning the comparison is still valuable.

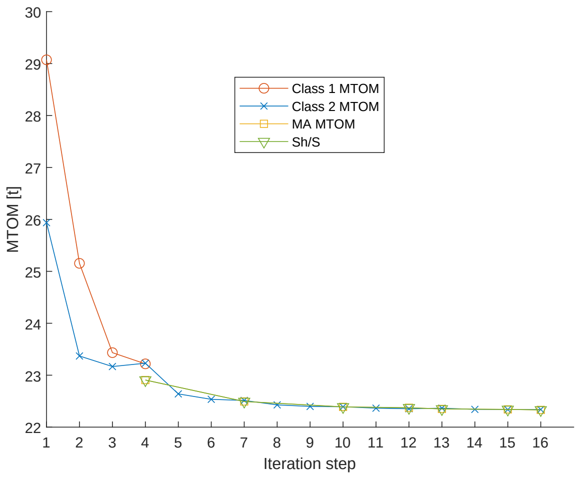

Figure 9.4: Initiator maximum take-off mass convergence for an aircraft based on the ATR 72-600

[1] https://www.esdu.com/cgi-bin/ps.pl?sess=unlicensed_1260621140113gpp&t=gen&p=home, accessed: 21-06-2026

III

Results

10
High Lift Study

As established in chapter 3, the maximum lift coefficients in take-off and landing configuration are key parameters for the sizing of the wing area and required thrust in conceptual aircraft design. In conceptual design, these values are often estimated using values from previous experience. This is not possible for aircraft with compliant morphing trailing edge wings due to the absence of validated empirical data. The effect of high-lift devices is often generalized in airfoil space at conceptual design level, prompting the need for an investigation into the lifting capabilities of morphing airfoils in high-lift configurations. The airfoils considered in this high-lift study will be presented in section 10.1. In chapter 5, the use of RANS based CFD was identified as being most appropriate for this study. The computational setup, including selected solver, computational mesh, and boundary conditions, will be detailed in section 10.2. Following, the results of the high-lift study will be presented in section 10.3. Finally, the results will be interpreted in context of the central research in this thesis in section 10.4.

10.1. High-lift morphing airfoils

The morphing airfoils considered in this maximum lift study are based on the NACA 43015 and the NACA 63412. These baseline airfoils were chosen based on their application on two reference aircraft in the regional turboprop class of aircraft: the ATR 72-600 [48] and the Fokker 50[1]. Two high-lift configurations were defined per baseline airfoil: one with a moderate trailing edge deflection and one with a high trailing edge deflection. The rear spar location for both configurations is at 60% of the chord. The moderately deflected configuration was generated using pseudo-deflection angles $\theta_1 = 5.0°$ and $\theta_2 = 10.0°$. Those for the highly deflected configuration are $\theta_1 = 10.0°$ and $\theta_2 = 20.0°$. The airfoil geometries for the NACA 63412 and NACA 43015 based airfoils are shown in Figure 10.1a and Figure 10.1b respectively.

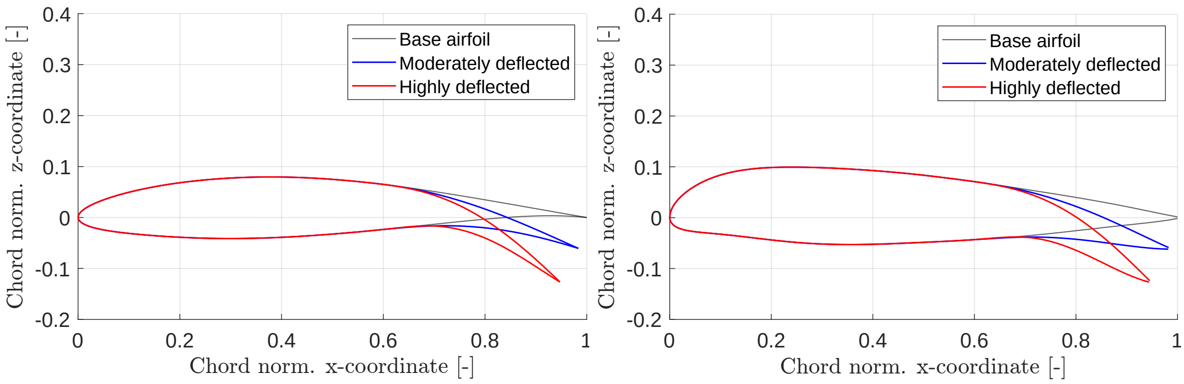

(a) NACA 63412 based airfoils

(b) NACA 43015 based airfoils

Figure 10.1: Morphing airfoil configurations for high-lift study

[1] https://m-selig.ae.illinois.edu/ads/aircraft.html, accessed 22-5-2026

10.2. Computational setup

For the CFD analyses, a C-type computational domain was adopted to ensure a uniform upstream distance of the domain inlet to the airfoil, and sufficient space for wake development. The inlet was placed at a distance of 20 chords from the airfoil, and the outlet was placed at 45 chords distance from the trailing edge. The computational domain is shown in Figure 10.2.

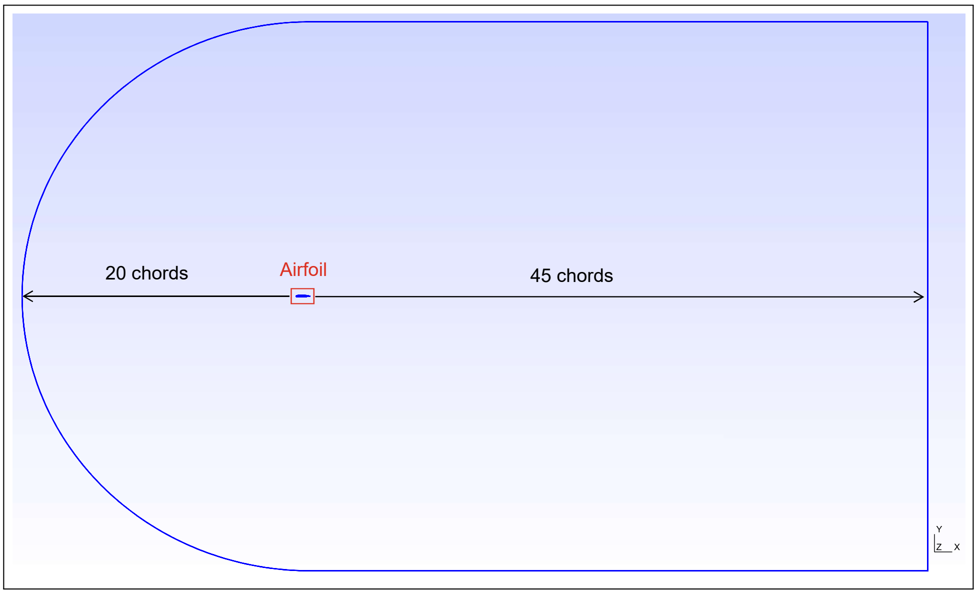

Figure 10.2: Computational domain for maximum lift studies

The mesh topology chosen is an unstructured tetrahedral mesh with a structured hexahedral inflation layer around the airfoil. This topology is adopted so that the same mesh setup can be used on all airfoils. The generation of structured meshes of sufficient quality around the morphed configurations was found to be impractical due to the high curvature of the trailing edge. The number of cells in the domain for the adopted meshes is around 275,000. An overview of the mesh is shown in Figure 10.3. The area around the airfoil, and the wake are refined in order to capture the steeper velocity gradients.

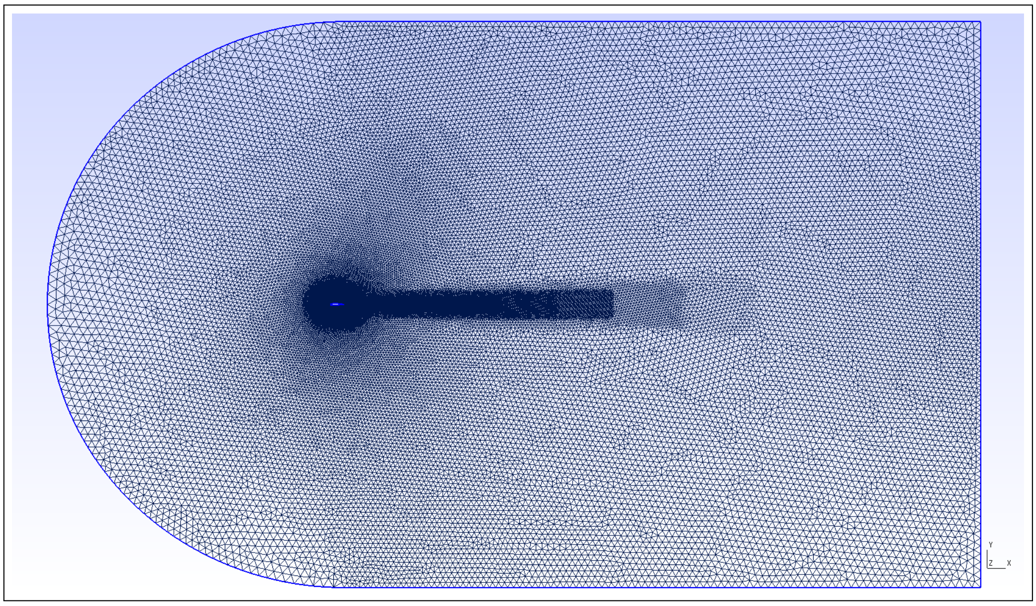

Figure 10.3: Overview of quasi-two-dimensional tetrahedral mesh

The structured hexahedral inflation layer is placed around the airfoil in order to model the boundary layer more accurately and efficiently. The alignment of the cells with the wall-normal direction enables accurate resolving of the steep velocity gradients around the airfoil. Furthermore, this approach allows for more consistent control over the first cell height. The meshes are wall resolved to avoid the use of wall functions, which are based on assumptions that break down near flow separation. The mesh was refined such that $y^+ \approx 1$ around the airfoil. The structured inflation layer is illustrated for the NACA 63412 baseline airfoil in Figure 10.4.

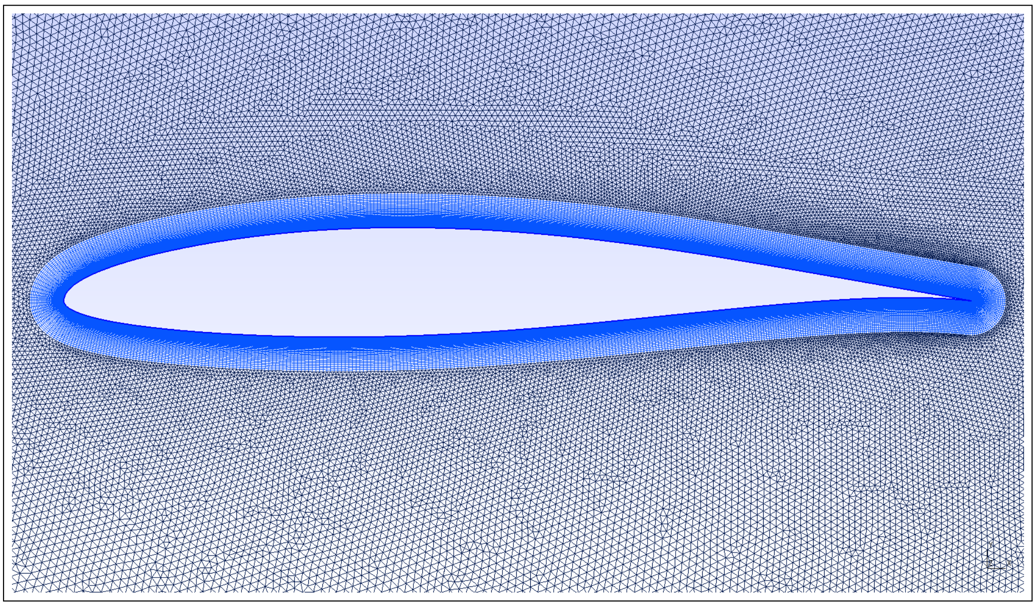

Figure 10.4: Structured hexahedral inflation layer around the airfoil for boundary layer resolution

The operating conditions considered for this high-lift study were introduced in chapter 5, and represent the lower end of the spectrum to be considered for CS-25 aircraft in terms of Reynolds and Mach number. The Reynolds number at which the simulations are run is 8.655×10^6, and the Mach number is 0.17. Because the Mach number is below 0.3, the flow may be considered to be incompressible, and OpenFOAM's incompressible solvers simpleFoam and pimpleFoam are used. The steady-state solver simpleFoam is preferred for its lower computational cost. In cases with significant flow separation, expected near stall, simpleFoam may not find a steady state solution. In these cases, the transient solver pimpleFoam is used. A key advantage of using pimpleFoam is that it is a pressure-based implicit solver, this allows it to handle local Courant–Friedrichs–Lewy (CFL) numbers larger than 1. Explicit solvers are limited to CFL numbers of 1 so that fluid does not travel more than one cell in a single timestep.

The simulations are set up as normalized, meaning $|U| = 1$. This was found to improve solver stability in early iterations from uniform initial conditions. Therefore, the velocity vector at the domain boundary follows from equation (10.1). Given that this is a (quasi-) two-dimensional simulation, the component w is always 0.

$$\vec{U} = \begin{pmatrix} u \\ v \\ w \end{pmatrix} = \begin{pmatrix} \cos\alpha \\ \sin\alpha \\ 0 \end{pmatrix} \tag{10.1}$$

To maintain the Reynolds number stated earlier, the kinematic viscosity ν is computed according to equation (10.2). Note that the chord remains in the equation, as the chords of the morphing configurations are not always equal to one. This is due to the arc-length of the suction side skin being maintained, as detailed in chapter 7. To maintain the chord-based Reynolds number, the kinematic viscosity has to account for the difference in chord.

$$\nu = \frac{|U|c}{Re} = \frac{c}{8.655 \times 10^6} \tag{10.2}$$

The value of the turbulent eddy viscosity, ν_t, is set based on a recommended range for the turbulent viscosity ratio for external aerodynamics, which is $1 \leq \frac{\nu_t}{\nu} \leq 10$ [68]. For the NACA 63412 case, ν_t was set to ten times the kinematic viscosity, to counteract turbulence decay in the freestream. The Langtry-Menter extension of the $k-\omega$ SST model was found to overpredict the portion of laminar flow over the airfoil when the turbulence intensity arriving at the airfoil was too low. For the NACA 43015 case, the turbulent eddy viscosity was set equal to the kinematic viscosity, as recommended by Spalart and Rumsey [69]. They also recommended a freestream turbulence level of 0.1% for external aerodynamics, adopted for both the NACA 63412 and NACA 43015 based airfoils. The resulting boundary value for the turbulent kinetic energy is computed according to expression (10.3) [56].

$$k = \frac{3}{2}\left(I|U_{ref}|\right)^2 = \frac{3}{2}\left(0.001 \cdot 1\right)^2 = 1.5 \times 10^{-6}\,\mathrm{m}^2\,\mathrm{s}^{-2} \tag{10.3}$$

The inflow condition for the specific turbulence dissipation rate ω is computed according to equation (10.4) [56]. Due to the appearance of the kinematic viscosity, the specific dissipation rate slightly differs between the baseline airfoil simulations and those for the morphing airfoils.

$$\omega = \frac{k}{\nu_t} = \frac{k}{\nu}\frac{\nu}{\nu_t} \tag{10.4}$$

The types of boundary conditions applied to the boundaries of the computational domain, the airfoil, and the side planes are summarized in Appendix B. Mixed inflow-outflow conditions on the domain boundary were applied, in the form of 'freestream' and 'inletOutlet' in OpenFOAM. This was done to minimize the effect of the boundary conditions on the solution. For the airfoil, low Reynolds number formulations of the ω and ν_t wall functions were used. Importantly, these do not model the behavior of the viscous sub-layer, but they ensure a smooth transition between this layer and the outer boundary layer.

The numerical schemes used in the simulations are summarized in Table B.1. All of these are second order accurate. The simulations were deemed converged upon plateau convergence of the lift-, and drag-coefficient for steady cases, or when oscillation around a steady mean was observed in transient cases.

A formal mesh convergence study was not performed. The conceptual focus of this study means absolute accuracy of the predicted coefficients is not the primary objective; the relative differences between baseline and morphed configurations are of interest, for which consistent discretization across cases is deemed sufficient. Nevertheless, mesh quality was verified against established best-practice criteria. The y^+ value at the airfoil wall was verified to remain near 1 or smaller in all simulations, and the wall-normal cell growth rate in the boundary layer is 1.1, below the values recommended by Casey and Wintergerste [70]. The wall-tangential discretization along the airfoil contains between 600 and 900 points, with denser local refinement in regions of high curvature. This is finer than the meshes used by Matyushenko and Garbaruk [58] in their high-lift study. Figure 10.4 shows the smooth transition between the structured boundary layer and the unstructured outer mesh.

10.2.1. Turbulence modeling

As motivated in chapter 5, the $k-\omega$ SST turbulence model is employed in the simulations. For the NACA 63412 based airfoils, the four-equation Langtry-Menter version is used to model boundary layer transition, as the NACA 6-series airfoils are laminar-flow airfoils [47]. The standard version of this model was used, as it was shown by Maughmer and Coder [52] to produce accurate results in high-lift conditions. This can be attributed to the model solving for the transition momentum thickness Reynolds number, which is linked to the momentum deficit in the boundary layer. This, in its turn, is linked to flow separation.

For the NACA 43015 baseline airfoil, the standard $k-\omega$ SST model was found to significantly overpredict the stall angle, and therefore the maximum lift coefficient. This phenomenon was introduced in chapter 5, and can be attributed to an overprediction of turbulent eddy viscosity in the boundary layer in adverse pressure gradient regions. This causes excessive turbulent momentum exchange from the outer boundary layer to the lower layers, keeping the boundary layer artificially attached. Experimental data was found on the NACA 43015 at a Reynolds number of 8.31×10^6 [71], which nearly matches the conditions considered. Following the work by Matyushenko and Garbaruk [58], the a_1 constant in the shear stress limiter in equation (5.3) was varied to match the experimental data. In the standard model, this constant has a value of 0.31. The maximum lift coefficient and stall angle from the experiments, 1.76 and 16.9°, were most closely matched when the constant was given a value of 0.287. In this case, the CFD results showed a maximum lift coefficient of 1.758 and a stall angle of 16°. The effect of changing the constant can be seen clearly in the velocity fields around the airfoil, as illustrated in Figure 10.5. The velocity field with the standard a_1 constant in Figure 10.5a shows a very uniform boundary layer which is indicative of the excessive mixing. The velocity field for the modified constant in Figure 10.5b clearly shows a separated region with recirculation over the trailing edge.

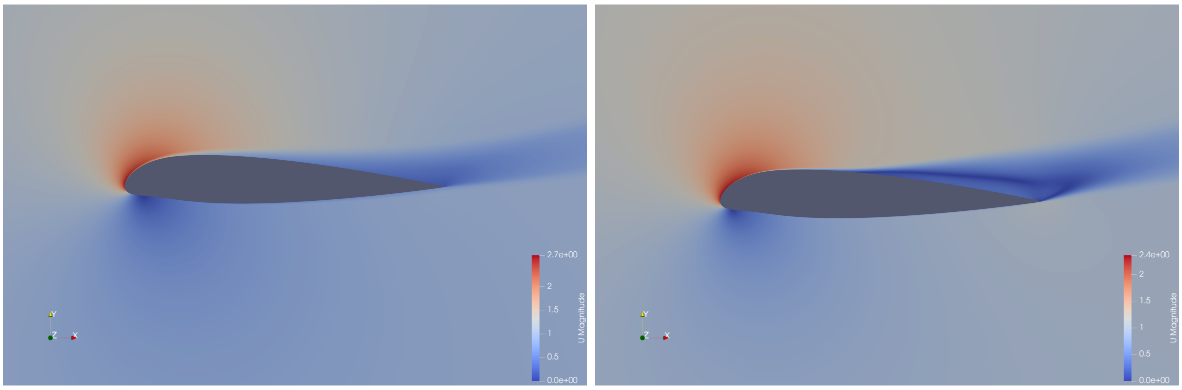

(a) Angle of attack 18°, $a_1 = 0.31$

(b) Angle of attack 17°, $a_1 = 0.287$

Figure 10.5: RANS $k-\omega$ SST predictions of velocity field around NACA 43015 airfoil at $Re = 8.655 \times 10^6$

A comparison of the lift polars for both model constants and the experimental results is shown in Figure 10.6. The experimental data shown was corrected for infinite aspect ratio.

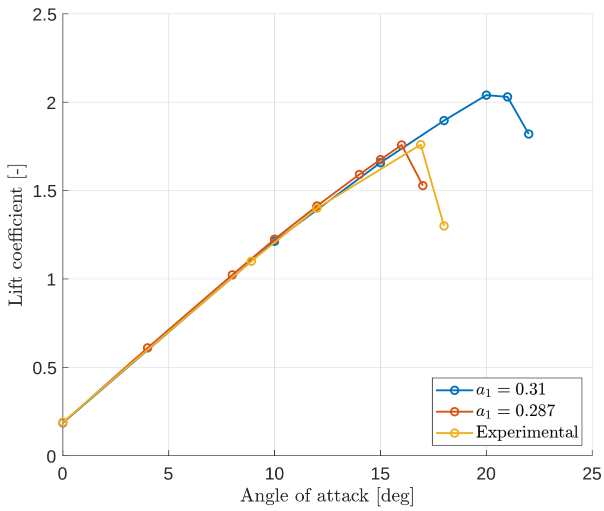

Figure 10.6: Comparison between RANS predicted lift polars using the $k-\omega$ SST turbulence model with varying a_1 model constants and experimental data [71]

The results for the baseline airfoil were significantly improved by tuning the a_1 constant. When using this in the simulations for the morphed configurations, however, the degree of flow separation was significantly overpredicted, predicting stall at an angle of attack of 8° for the moderate trailing edge deflection airfoil. Moreover, the maximum predicted lift coefficient was 1.5, which is worse than the baseline airfoil. These results were therefore discarded, as they are unlikely to be physically meaningful. This results in a dilemma: the standard $k-\omega$ SST model overpredicts the maximum lift coefficient of the baseline airfoil, and the modified model underpredicts the lifting capabilities of the morphing configurations. Tuning the a_1 constant to match the experimental data changes the model to fit a certain adverse pressure distribution. Since this changes between the baseline and morphing configurations, these are not cross-compatible. Matyushenko and Garbaruk [58] notes this as a fundamental limitation of semi-empirical turbulence models that are calibrated based on a set of standard turbulence flows.

10.3. Results

The primary results of this high-lift study are the lift curves of the airfoils, which will be presented for the NACA 63412 based airfoils first, followed by those for the NACA 43015. The computed lift polars of the baseline airfoil, and morphing configurations are shown in Figure 10.7. No experimental data on the NACA 63412 at Reynolds numbers near the one considered were found. The lift polar for the baseline airfoil, as computed with Xfoil, is therefore included for validation of the numerical setup. At angles of attack below $10°$, away from significant flow separation, the $k-\omega$ SST-LM model and Xfoil agree well, which is a good indication of the validity of the CFD results.

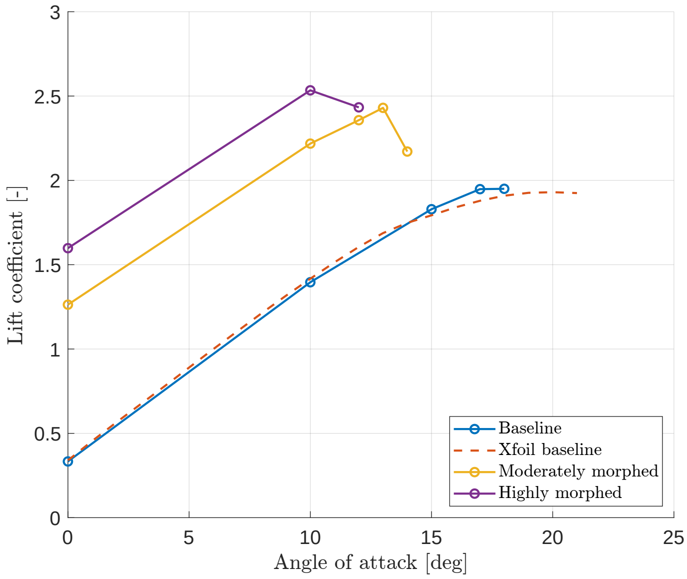

Figure 10.7: Computed lift polars for NACA 63412 base airfoil and morphing configurations

The general behavior of the lift curves is as expected: an increase in deflection shifts the curve upwards and reduces the stall angle. The morphing lift curves are not significantly shallower than the baseline, which is somewhat surprising given the expected separation over the deflected trailing edge. Separation is in fact observed over the highly deflected morphing trailing edge, as illustrated in Figure 10.8, but it does not appear to flatten the lift curve as much as anticipated.

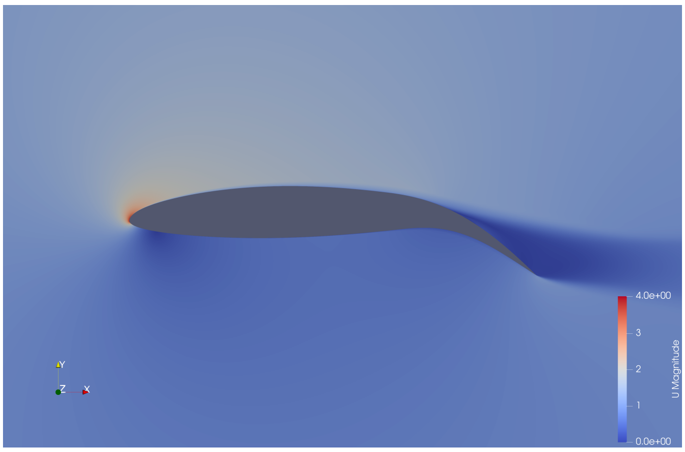

Figure 10.8: NACA 63412 morphing configuration at an angle of attack of $10°$ showing significant separation over the trailing edge

The lift curve for the baseline airfoil in Figure 10.7 shows that the airfoil stalls gradually, indicating that trailing edge stall is the stall mechanism. Data from Obert [64, 119] supports that the NACA 63412 indeed exhibits trailing edge stall at the Reynolds number considered. The trailing edge separated region can indeed be seen for the baseline airfoil, as illustrated in Figure 10.9.

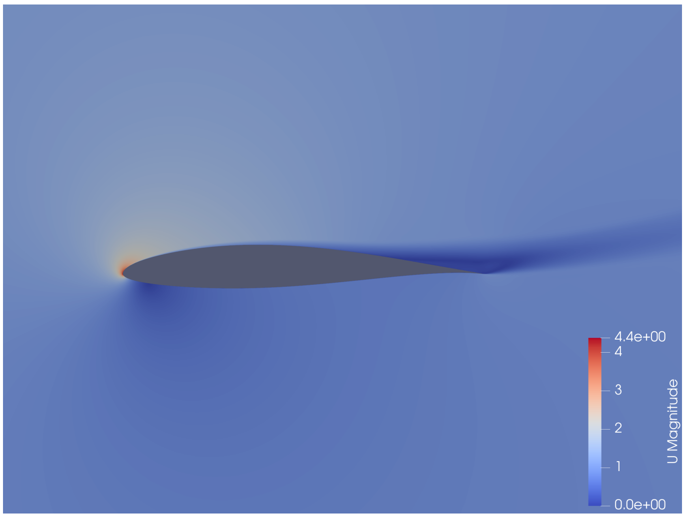

Figure 10.9: NACA 63412 airfoil at $\alpha = 18°$, exhibiting trailing edge stall

The computed lift polars for the NACA 43015 are shown in Figure 10.10. The lift curve of the baseline airfoil shown is the one computed with the modified a_1 constant, while the morphing lift curves shown have been computed with the standard formulation of the turbulence model. The motivation for this is that, for the baseline airfoil, the CFD results did not predict any separation at angles of attack where it should be present, as shown in Figure 10.5a. Rather, the model predicts a very thick, but attached boundary layer in which excessive mixing keeps the boundary layer attached artificially. The standard formulation of the model was able to predict separation over the morphed configurations due to the additional camber near the trailing edge, as illustrated in Figure 10.11. The standard model is therefore used for the morphed configurations, because it predicts separation where it can reasonably be expected. This decision is further supported by the modified model predicting stall at an $8°$ angle of attack for the moderately morphed configuration. The stall angle decreases excessively for the amount of camber added by the moderately morphed deflection.

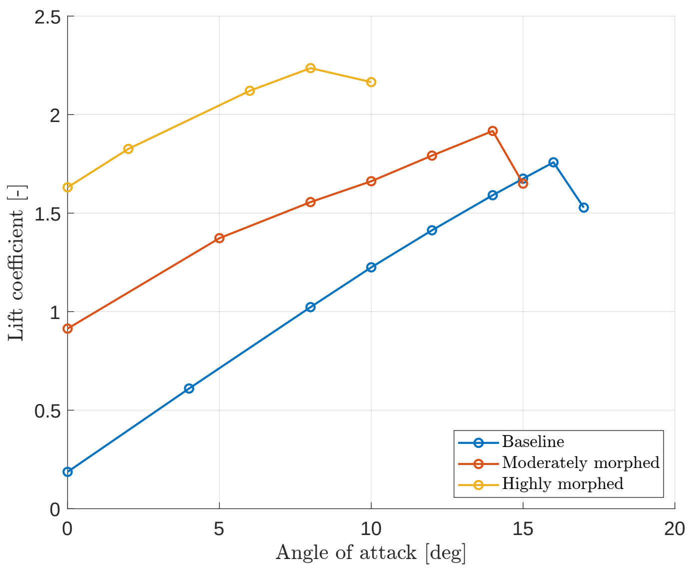

Figure 10.10: Computed lift polars for NACA 43015 base airfoil and morphing configurations

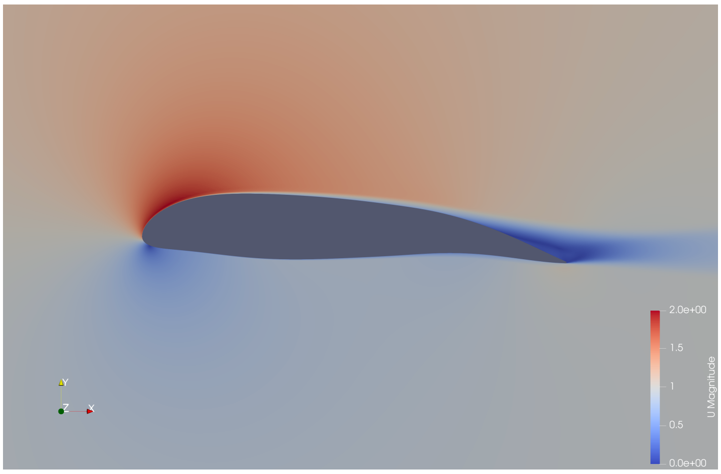

Figure 10.11: Standard $k-\omega$ SST predicted velocity field around moderately morphed airfoil based on the NACA 43015 at an angle $8°$, showing clear evidence of separation over the trailing edge

10.4. Interpretation of results

In this section, the results obtained in the high-lift study will be discussed and interpreted, with the aim of synthesizing the implications of the study in light of the overall research in this thesis. The high-lift study is based on two airfoils due to time constraints. To generalize the results beyond the airfoils considered, they will be compared to the expected performance of plain flaps, which are the most similar conventional trailing-edge high-lift devices to morphing airfoils. Conceptual relationships exist to predict the lift increments due to plain flaps based on the flap-to-chord-ratio, airfoil thickness-to-chord-ratio, and flap deflection angle, as shown in equation (10.5). The values of $C_{l_{\delta_f}}$, K, and K' are obtained from graphs presented by Roskam [32]. In this expression, ΔC_l represents the lift increase at $0°$ angle of attack with respect to the undeflected airfoil. $\Delta C_{l_{max}}$ represents the increase in the maximum lift coefficient.

$$\Delta C_l = C_{l_{\delta_f}} \delta_f K' = \frac{\Delta C_{l_{max}}}{K} \tag{10.5}$$

To compare the morphing results to these predictions, equivalent plain flap deflection angles are determined to match the morphing airfoil deflections. The similarity parameters used for this matching are the hinge location, set equal to the rear spar location of the morphing airfoil, and the trailing edge deflection angle. For both baseline airfoils, the equivalent plain flap deflection angles for the moderately and highly deflected morphing configurations are $10°$ and $25°$ respectively. The matched geometries are shown in Figure 10.12.

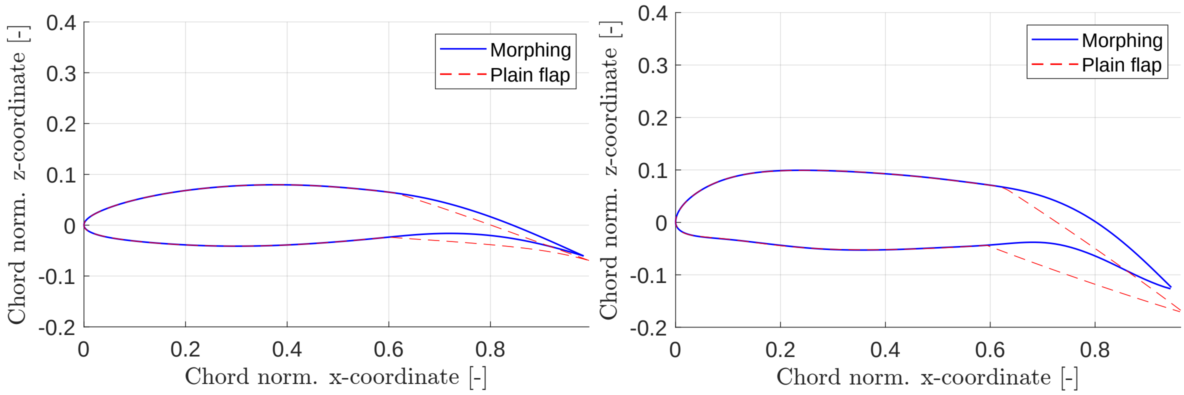

(a) NACA 63412 based moderately morphed airfoil, equivalent plain flap deflection angle $\delta_f = 10°$

(b) NACA 43015 based highly morphed airfoil, equivalent plain flap deflection angle $\delta_f = 25°$

Figure 10.12: Comparison of morphing high-lift configurations with plain flapped airfoils for performance comparison

The comparison between the plain flap predictions and the computed lift increments for the morphing configurations is summarized in Table 10.1.

Table 10.1: Predicted lift coefficient increments from conceptual relations for plain flaps and CFD simulations of morphing airfoils

		NACA 63412 based			NACA 43015 based		
		Plain flap	Morphing	Δ [%]	Plain flap	Morphing	Δ [%]
$\delta_f = 10°$	ΔC_l	0.9076	0.9296	$+2.42$	0.9250	0.7270	-21.41
	$\Delta C_{l_{max}}$	0.4538	0.4800	$+5.77$	0.4625	0.1590	-65.62
$\delta_f = 25°$	ΔC_l	1.4294	1.2646	-11.53	1.4569	1.4440	-0.89
	$\Delta C_{l_{max}}$	0.7147	0.5840	-18.29	0.7285	0.4780	-34.39

The computed lift increments for the morphing airfoils do not follow a consistent trend relative to the plain flap predictions. The moderately morphed NACA 63412 based airfoil outperforms the plain flap prediction by a few percent, while the moderately morphed NACA 43015 based airfoil performs significantly worse. The NACA 43015 based airfoils particularly underperform in terms of the maximum lift coefficient. The plain flap relations do not account for the original camber distribution of the baseline airfoil, however. Combined with the lack of a clear pattern in the results, this prompts skepticism toward applying the plain flap relations directly to morphing airfoils.

What can be stated with certainty is that plain flaps add more camber to an airfoil for an equivalent hinge location and trailing edge deflection angle, as seen in Figure 10.12b. For the highly morphed NACA 43015 based example, the effective angle of attack of the plain flapped section is $2.41°$ higher than that of the morphed section. This difference arises because the first-order continuity of the camberline and surface is preserved at the rear spar for morphing airfoils, while plain flapped airfoils have a sharp corner. The additional smoothness likely explains why the moderately morphed NACA 63412 based configuration outperforms the prediction for its plain flap equivalent. At higher deflection angles, however, the smoothness benefit does not keep the flow attached significantly longer over morphing airfoils, and the additional camber of plain flaps starts to pay off.

A further consideration is the achievability of the high-lift configurations themselves. Plain flaps rely on a simple hinge at the leading edge of the flap, and typically deflect to angles of up to $60°$ in landing configuration. The 2-DoF morphing concept introduced in chapter 1 is actuated by two actuators that connect to the pressure side skin through straight connection rods, as shown in Figure 10.13. This actuation strategy imposes a geometric limit on the achievable deflection, as the connection rods eventually meet the pressure side skin.

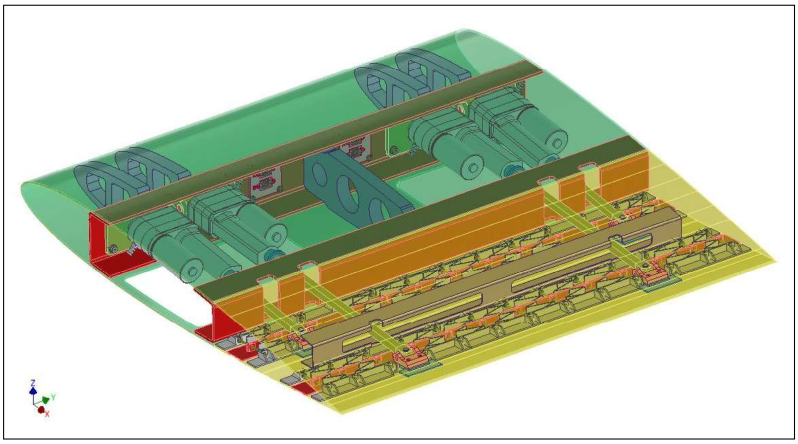

Figure 10.13: Isometric view of 2-DoF morphing trailing edge concept [72]

This geometric limit is specific to the morphing concept under study. One of the challenges identified in chapter 2 is the difficulty of generalizing morphing-wing performance beyond a specific concept, and so the actuation limit is not adopted as a hard constraint in determining the achievable $\Delta C_{l_{max}}$ in the present analysis. It is noted instead as a consideration for the mechanical and structural design of future morphing concepts.

The interpretation is further constrained by the scope of the study. The high-lift performance of a morphing airfoil depends strongly on the baseline geometry, as the contrasting results for the NACA 63412 and NACA 43015 demonstrate. The definition of a high-lift configuration is also less clear for morphing airfoils than for plain flapped airfoils. The same trailing edge deflection can be produced by different combinations of pseudo-deflections, each with a different lift response. Due to time constraints, exploration of these combinations across multiple baseline airfoils was not feasible within the scope of the present study.

Despite these limitations, the available evidence supports a conservative estimate of the achievable $\Delta C_{l_{max}}$ for the 2-DoF morphing trailing edge concept. According to Raymer [28], plain flaps in landing configuration deliver a $\Delta C_{l_{max}}$ of 0.9 at conceptual design level. At the deflection angles tested in this study, the morphing airfoils show a 20% to 30% deficit relative to the corresponding plain flap predictions. Since flow separation can be expected to worsen at higher deflection angles, the upper end of this range is adopted as the design assumption. This yields a conservative estimate of $\Delta C_{l_{max}} = 0.63$ for the morphing trailing edge concept under study.

Partial support for this value comes from the CFD results themselves. The highly morphed NACA 63412 based airfoil already reaches $\Delta C_{l_{max}} = 0.58$ at an equivalent plain flap deflection of $25°$, within 0.05 of the assumed bound. The NACA 43015 based airfoil reaches 0.48 at the same deflection, leaving a larger gap of 0.15, which is considered closable at the higher deflections of full landing configuration. The value $\Delta C_{l_{max}} = 0.63$ is carried forward into chapter 9, where it is translated into the wing-level lift performance of the aircraft.

11

Sizing studies & performance comparison

This chapter presents two case studies comparing the conceptual-level sizing and performance of aircraft designs with chordwise 2-DoF morphing trailing edge wings to reference designs with conventional wings. The ATR 72-600 and Fokker 100 are selected as the reference aircraft for the case studies, which are presented in section 11.1 and section 11.2 respectively. These aircraft were chosen because of the expected deficit in high-lift performance of compliant MTE wings compared to wings with conventional high-lift devices, though the specific reason differs between the two. The ATR 72-600 is capable of operating from short runways, while it frequently serves airports with larger runway lengths available. This leaves margin for a meaningful sensitivity study on the field-length requirements. The Fokker 100 is the only CS-25 aircraft certified to take off without deployment of high-lift devices [64], suggesting that its sizing is less sensitive to high-lift performance.

Both case studies follow the same structure. First, the high-lift performance of the aircraft is estimated using the relations presented in chapter 3 together with the airfoil-level results presented in chapter 10. The resulting estimates serve as inputs to the sizing process. The sizing results for the morphing wing aircraft are then compared to those of the reference design in the form of sensitivity studies. Where the original top-level aircraft requirements lead to an infeasible design, they are relaxed, after which the block-fuel performance is quantified over the design mission and a set of off-design missions.

11.1. ATR 72-600 case study

The ATR 72-600 is a regional turboprop aircraft which seats up to 72 passengers in a standard configuration, with a design range of 758 nautical miles. It cruises at 275 knots true air speed and has a maximum take-off weight of 22 800 kg [73]. The aircraft is configured with a high wing, wing-mounted engines, and a T-tail, as illustrated in Figure 11.1.

Figure 11.1: ATR 72-600[1]

11.1.1. High-lift performance estimation

As stated in the introduction of this chapter, the ATR 72-600 is capable of operating from short runways and challenging airfield profiles, as described by ATR themselves[2]. This is reflected in its take-off and landing field lengths of $1279\,\mathrm{m}$ and $915\,\mathrm{m}$ respectively [49]. These short field lengths can partly be attributed to the wing-mounted propellers, of which the slipstream amplifies the high-lift performance of the wing. This propeller contribution must be accounted for on the morphing wing as well, otherwise the high-lift deficit of the morphing wing relative to the reference would be overestimated.

Using the relations presented in subsection 3.1.2, the maximum lift coefficients in take-off and landing configuration for the reference aircraft are derived from the field lengths, yielding values of 2.4 and 3.0 respectively. To isolate the flap contribution from the propeller contribution, the high-lift performance is first estimated without propeller effects, using the conceptual relationships that generalize high-lift performance in airfoil space, and translate it to the wing. No data was found on the exact type of high-lift devices used on the ATR 72-600. From visual inspection, these are single-slotted flaps with a degree of Fowler motion, as illustrated in Figure 11.2. The conceptual relationships for Fowler flaps are therefore adopted.

Figure 11.2: Illustration for visual derivation of the type of trailing edge high-lift devices on the ATR 72-600[3]

The prediction for the lift increase due to Fowler flap deployment is given in equation (11.1). The flapped-section lift-curve slope $C_{l_{\alpha_f}}$ follows from equation (11.2), in which the base section lift-curve slope is scaled by a factor of $1+c_f/c$. The parameter α_{δ_f} is obtained from graphs presented by Roskam [32].

$$\Delta C_l = C_{l_{\alpha_f}} \alpha_{\delta_f} \delta_f = \frac{\Delta C_{l_{max}}}{K} \tag{11.1}$$

$$C_{l_{\alpha_f}} = C_{l_\alpha} \left(1 + \frac{c_f}{c}\right) \tag{11.2}$$

The airfoils in the wing of the ATR 72-600 are NACA 430XX airfoils, in which XX denotes the thickness-to-chord ratio. This ratio varies in the spanwise direction, with values of 18%, 16%, and 13% at the root, kink, and tip respectively [48]. The lift-curve slopes required in equation (11.2) are taken from experimental data at Reynolds numbers around 8.3×10^6, close to the mean-aerodynamic-chord-based Reynolds number for the ATR 72-600 at its approach speed of 113 knots [73]. For the kink and tip, the lift-curve slopes of the NACA 43015 and 43012 are substituted, as no data for the 43016 and 43013 were available. The flap deflections for take-off and landing are $15°$ and $30°$ respectively, and the flap-to-chord ratio is visually estimated to be 0.25 from Figure 11.2. The resulting sectional lift increases are summarized in Table 11.1.

[2] https://www.atr-aircraft.com/aircraft-services/aircraft-family/atr-72-600/, accessed 28-06-2026

Table 11.1: Computation of sectional lift increases for NACA 430XX airfoils with Fowler flaps

		C_{l_α} deg^{-1}	$C_{l_{\alpha_f}}$ deg^{-1}	ΔC_l [-]	$\Delta C_{l_{max}}$ [-]
Take-off, $\delta_f = 15°$, $\alpha_{\delta_f} = 0.51$	43018	0.096	0.120	0.918	0.891
	43015	0.101	0.126	0.966	0.937
	43012	0.100	0.125	0.956	0.928
Landing, $\delta_f = 30°$, $\alpha_{\delta_f} = 0.45$	43018	0.096	0.120	1.62	1.57
	43015	0.101	0.126	1.70	1.65
	43012	0.100	0.125	1.69	1.64

To convert the sectional lift increases to wing level, the ratio of flapped area to total wing area must be determined. The wing is divided into spanwise sections, and the contribution of each section to the wing maximum lift increase is computed separately. The section boundaries and areas were derived from three-view drawings of the aircraft [49], as exact geometry data was not available. This introduces some measurement uncertainty in the derived planform. The geometry is illustrated in Figure 11.3.

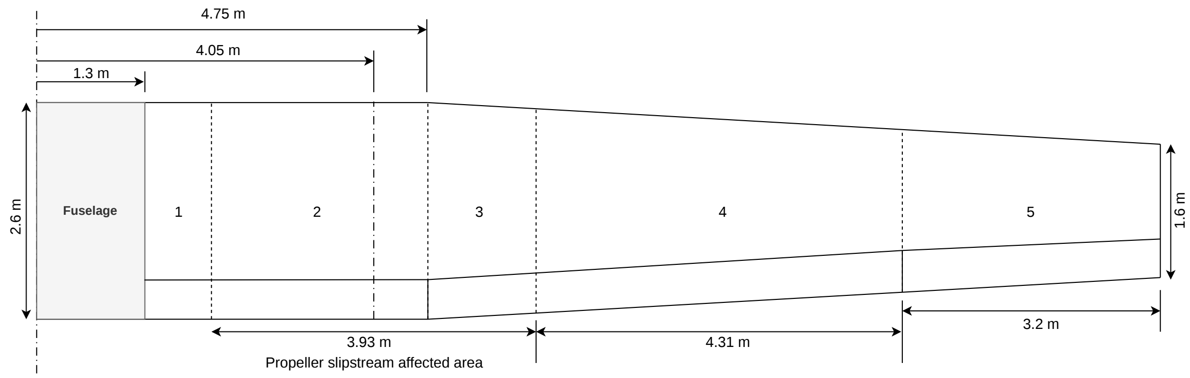

Figure 11.3: Derived wing planform geometry for ATR 72-600, including propeller slipstream affected areas

The computation of the wing lift increase without propeller effects is summarized in Table 11.2. The errors in the bottom row are computed with respect to the target lift increases and a reference wing area of $61.0\,\mathrm{m}^2$. The target lift increases assume a clean maximum lift coefficient of 1.4, taken from the Initiator input file for the ATR 72-600 as no widely available reference value was found. The take-off and landing target lift increases are therefore 1.0 and 1.6 respectively.

Table 11.2: Computation of wing lift increase due to Fowler flaps for the ATR 72-600 wing without including the effects of propellers

Section	$S_w \mathrm{m}^2$	$\Lambda_{c/4}$ [deg]	K_Λ [-]	**Airfoil**	$\Delta C_{l_{max_{TO}}}$ [-]	$\Delta C_{L_{max_{TO}}}$ [-]	$\Delta C_{l_{max_L}}$ [-]	$\Delta C_{L_{max_L}}$ [-]
Fuselage	6.76	0	0.9200	-	0	0	0	0
1	4.08	0	0.9200	43018	0.8905	0.0548	1.5714	0.0967
2	13.86	0	0.9200	43016	0.9368	0.1958	1.6532	0.3455
3	6.39	3	0.9193	43016	0.9368	0.0902	1.6532	0.1592
4	18.96	3	0.9193	43016	0.9368	0.2677	1.6532	0.4725
5	11.36	3	0.9193	43013	0	0	0	0
Total	61.41					0.6086		1.0739
Error	+0.68%					-39.1%		-32.9%

The predicted lift increments fall well short of the targets, with deficits of 39.1 % in take-off and 32.9 % in landing. This is expected, as the propellers have been excluded from the analysis. The propeller slipstream raises the local dynamic pressure over the wing sections aft of the disc and energizes the boundary layer, both of which increase the achievable sectional lift coefficient. To account for this, the sectional lift increases in sections two and three, which lie in the propeller slipstream, are amplified by a blowing factor which is calibrated such that the expected high-lift performance is met. In take-off and landing configuration, these factors are 2.369 and 2.043 respectively. The recomputation with these factors applied is shown in Table 11.3. The wing area, sweep angles, and airfoil sections are unchanged from Table 11.2 and are not repeated.

Table 11.3: Computation of wing lift increase due to Fowler flaps for the ATR 72-600 wing, including the effects of propellers

Section	$\Delta C_{l_{max_{TO}}}$ [-]	$\Delta C_{L_{max_{TO}}}$ [-]	$\Delta C_{l_{max_L}}$ [-]	$\Delta C_{L_{max_L}}$ [-]
Fuselage	0	0	0	0
1	0.8905	0.0548	1.5714	0.0967
2	2.2194	0.4639	3.3776	0.7059
3	2.2194	0.2137	3.3776	0.3252
4	0.9368	0.2677	1.6532	0.4725
5	0	0	0	0
Total		1.0		1.6
Error		±0%		±0%

The calibrated blowing factor is an empirical correction, not a physical model of the propeller-wing interaction. Two consistency checks support its use. First, the resulting propeller contribution to the wing maximum lift coefficient of approximately 0.4 in take-off and 0.6 in landing is of the right order relative to the literature. Gentry *et al.* [74] report that for a double-slotted Fowler system at $\delta_f = 60°$ in moderate power, the propeller-driven lift increase over the power-off case can reach 1.2. The values found here are lower, consistent with the ATR's simpler high-lift system and lower flap deflection in landing. Second, the take-off blowing factor exceeds the landing value, consistent with the higher engine power setting used during take-off.

The blowing factors calibrated above are carried over to the morphing wing high-lift analysis under the assumption that the propeller configuration and the sections lying in the propeller slipstream are unchanged relative to the reference aircraft. This approach is adopted given that the morphing wing aircraft is a redesign of the ATR 72-600 with the same powerplant and a comparable wing planform. The sectional maximum lift coefficient increases used for the morphing wing are 0.63 in landing, as motivated in chapter 10, and 0.5 in take-off, which was shown in that same chapter to be comfortably achievable. The area division is unchanged. The morphing trailing edge on the outboard wing, where the aileron sits on the reference aircraft, is assumed to be responsible for roll control only and not to contribute to the high-lift performance. The resulting wing lift increase is shown in Table 11.4.

Table 11.4: Computation of wing lift increase due to morphing for the ATR 72-600 wing, including the effects of propellers

Section	$\Delta C_{l_{max_{TO}}}$ [-]	$\Delta C_{L_{max_{TO}}}$ [-]	$\Delta C_{l_{max_L}}$ [-]	$\Delta C_{L_{max_L}}$ [-]
Fuselage	0	0	0	0
1	0.50	0.031	0.630	0.039
2	1.18	0.248	1.287	0.269
3	1.18	0.114	1.287	0.124
4	0.50	0.143	0.630	0.18
5	0	0	0	0
Total		0.536		0.612

The morphing wing falls short of the reference aircraft in both configurations, reaching lift increases of only 0.536 against 1.0 in take-off and 0.612 against 1.6 in landing. A possible way to mitigate this deficit is by adding a leading-edge device. The reference ATR 72-600 does not feature slats, so their addition to the morphing wing is examined as part of the sensitivity analysis presented later in this chapter. To support that analysis, the high-lift performance of the morphing wing with slats is estimated here.

As presented in subsection 3.1.3, the maximum lift coefficient of a section with a leading-edge device is estimated as the maximum lift coefficient of the section without the device, multiplied by the ratio of the extended chord to the base chord. The chord increase due to slats is assumed to be 10%. Combining the experimental base sectional maximum lift coefficients with the morphing sectional lift increases, the slatted sectional lift increases are computed as shown in Table 11.5.

Table 11.5: Computation of sectional lift increases with slats for morphing sections in ATR 72-600 wing

	$C_{l_{max}}$ [-]	Configuration	□$C_{l_{max_{MTE}}}$ [-]	$C_{l_{max}}$, MTE [-]	$C_{l_{max}}$, slatted [-]	$\Delta C_{l_{max}}$ [-]
43018	1.63	Take-off	0.5	2.13	2.343	0.713
		Landing	0.63	2.26	2.486	0.856
43015	1.76	Take-off	0.5	2.26	2.486	0.726
		Landing	0.63	2.39	2.629	0.869
43012	1.84	Take-off	0.5	2.34	2.574	0.734
		Landing	0.63	2.47	2.717	0.877

The corresponding wing lift increases are shown in Table 11.6. The blowing factors from the reference analysis are applied to sections two and three in the same manner as before. The outer wing section, in which the morphing trailing edge acts as an aileron, now contributes to the maximum lift increase through the slats alone.

Table 11.6: Computation of wing lift increase due to morphing and slats for the ATR 72-600 wing, including the effects of propellers

Section	$\Delta C_{l_{max_{TO}}}$ [-]	$\Delta C_{L_{max_{TO}}}$ [-]	$\Delta C_{l_{max_{L}}}$ [-]	$\Delta C_{L_{max_{L}}}$ [-]
Fuselage	0	0	0	0
1	0.713	0.044	0.856	0.053
2	1.720	0.360	1.775	0.371
3	1.720	0.166	1.775	0.171
4	0.726	0.208	0.869	0.248
5	0.184	0.032	0.184	0.032
Total		0.810		0.875

11.1.2. Sizing studies

This subsection presents the sizing studies performed using the Initiator. The first study explores the sensitivity of the sized aircraft to the specific mass of the morphing system. As introduced in chapter 3, no empirical data on the mass of full-scale morphing structures is available. The specific mass of the morphing system is therefore treated as parametric. The range adopted for the parameter is between $10\,\mathrm{kg\,m^{-2}}$ and $30\,\mathrm{kg\,m^{-2}}$. The upper bound is set based on the specific weight of Fowler flaps for the maximum take-off mass of the ATR 72-600, found using relations presented by Torenbeek [11]. It is reasoned that this is a conservative upper bound, as Fowler flaps rely on distinct sub-surfaces and mechanisms that a compliant morphing structure does not require. Three dependent variables are examined: the maximum take-off mass, sized wing area, and total sized power. Both the morphing configuration and the morphing configuration with slats are compared against the reference ATR 72-600 conceptual aircraft.

The sensitivity of the MTOM to the specific morphing system mass is shown in Figure 11.4. The morphing wing aircraft is heavier than the reference across the entire range considered, by approximately $900\,\mathrm{kg}$ at the lower bound of the specific mass and $2400\,\mathrm{kg}$ at the upper bound. The MTOM depends approximately linearly on the specific morphing system mass, with a slope of roughly $80\,\mathrm{kg}$ per $\mathrm{kg\,m^{-2}}$ for both configurations. The two configurations produce similar MTOM values throughout the range, despite differing in both high-lift performance and wing structural weight. The reason becomes clear only from the sized wing area and total sized power, which are examined next.

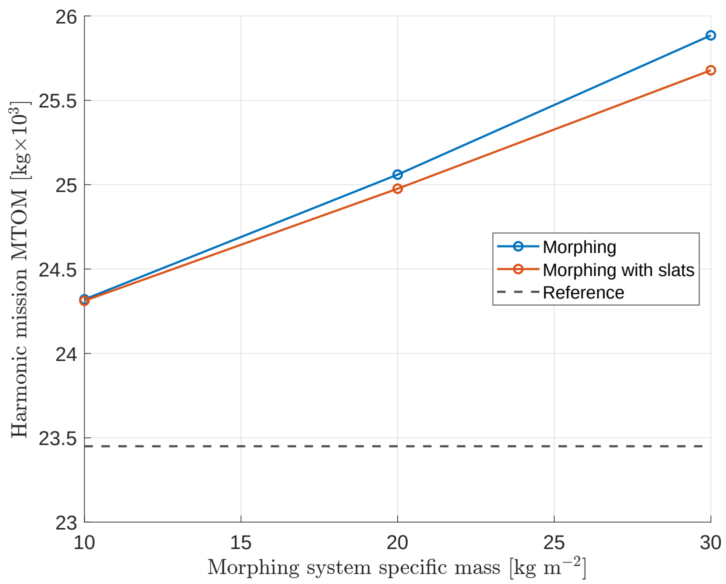

Figure 11.4: Sensitivity of harmonic mission MTOM to the specific mass of the morphing system for an ATR 72-600 based aircraft with a morphing wing

The sensitivity of the sized wing area to the specific morphing system mass is shown in Figure 11.5. Both morphing configurations require a significantly larger wing than the reference conceptual design, which has a wing area of $68.5\,\mathrm{m}^2$. Without slats, the required wing area is between $104\,\mathrm{m}^2$ and $111\,\mathrm{m}^2$, and with slats it is between $94\,\mathrm{m}^2$ and $99\,\mathrm{m}^2$. This is a direct consequence of the high-lift deficit reported in subsection 11.1.1. The lower $\Delta C_{L_{max}}$ in landing configuration forces a larger wing to satisfy the same landing distance requirement. Adding slats reduces the wing area by approximately $10\,\mathrm{m}^2$ across the range, in line with the increase in high-lift performance.

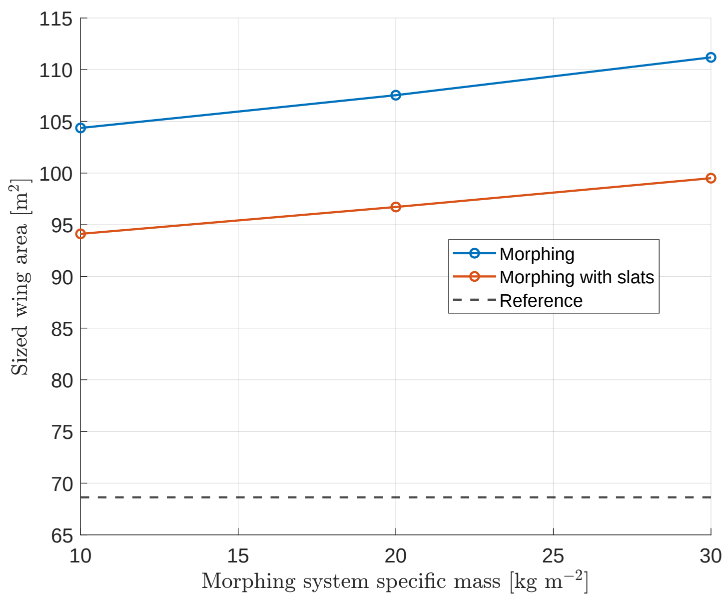

Figure 11.5: Sensitivity of the sized wing area to the specific mass of the morphing system for an ATR 72-600 based aircraft with a morphing wing

The reduction in wing area with slats does not translate directly into a lower MTOM. The leading-edge device carries a structural weight penalty of its own, which partly cancels the structural weight saving from the smaller wing. A second effect is at play through the total sized power, shown in Figure 11.6. Both morphing configurations require more power than the reference. The slatted configuration requires approximately $200\,\mathrm{HP}$ less power than the non-slatted configuration across the range. The smaller wing of the slatted configuration requires less power in cruise, which was found to be the limiting constraint for the power sizing. Since the Initiator applies rubberized engine sizing, the lower power requirement produces a lighter engine, which further compensates for the added structural weight of the slats. The two compensating effects together explain why the MTOM curves in Figure 11.4 lie close to one another.

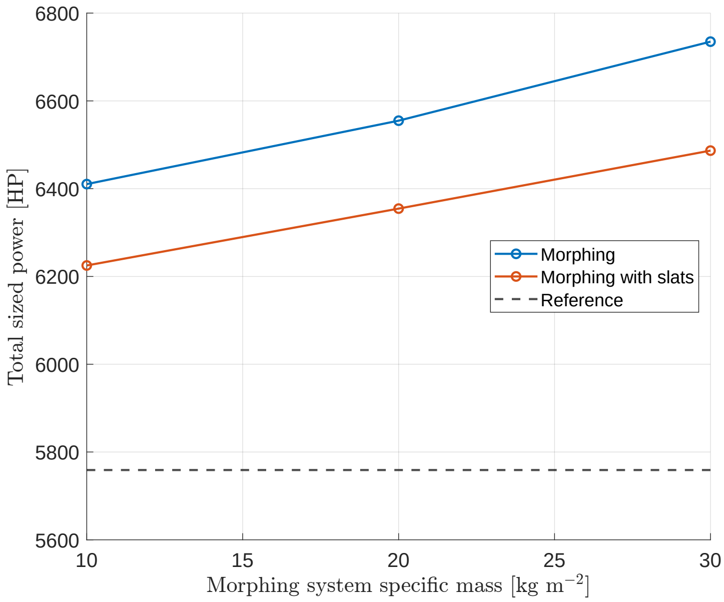

Figure 11.6: Sensitivity of the total sized power to the specific mass of the morphing system for an ATR 72-600 based aircraft with a morphing wing

The activity of the sizing constraints is illustrated in Figure 11.7, which shows the wing-thrust loading diagram for the morphing-plus-slats configuration at $30\,\mathrm{kg\,m^{-2}}$. The design point sits at the intersection of the landing constraint and the cruise constraint. The landing constraint drives the sized wing area, and the cruise constraint drives the sized total power. This constraint split explains the entire sizing result: the high-lift deficit from chapter 10 forces a larger wing to meet the landing distance, and the larger wing in turn forces more installed power to meet the cruise requirement. The morphing wing pays for its high-lift deficit twice in the sizing.

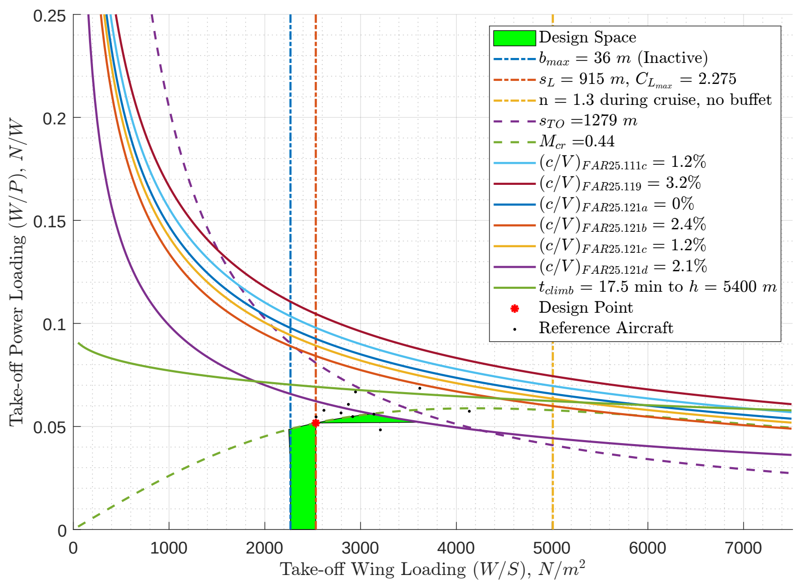

Figure 11.7: Wing-thrust loading diagram for ATR 72-600 based aircraft with morphing wing and slats showing that the cruise performance is limiting for the power sizing

The sized maximum take-off masses, wing areas, and total power are consistently higher than those of the reference aircraft, which can be attributed to the reduced high-lift performance. A sensitivity study is therefore performed on the field performance, as this directly influences the sizing of the wing for take-off and landing. The take-off field length is varied between 100% and 160% of the original value of $1279\,\mathrm{m}$. The landing field length is varied between 100% and 130% of the original value of $915\,\mathrm{m}$. The specific morphing system mass for this sensitivity study is fixed at $18\,\mathrm{kg\,m^{-2}}$, which is around the middle of the range considered, taking into account that the upper bound of the range is a conservative one. No slats were considered for this sensitivity study. The sensitivity of the maximum take-off mass to the field lengths is presented in Figure 11.8. Interestingly, the results show no dependence on the take-off field length, which is in line with the earlier observation of the take-off constraint not being the limiting one for the power sizing. As the landing field length requirement is relaxed, the landing constraint in Figure 11.7 moves towards higher wing loadings. This decreases the wing size and increases the power loading, as the cruise constraint becomes less stringent. These effects together lead to a lower take-off weight.

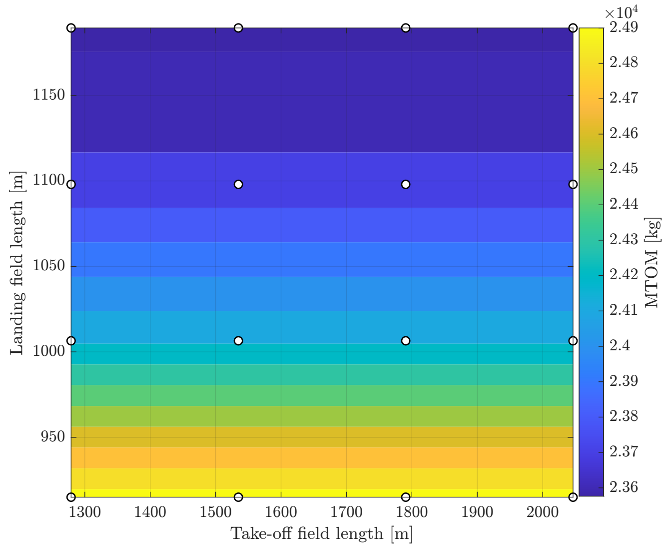

Figure 11.8: Sensitivity of MTOM to field length requirements for a morphing wing aircraft based on the ATR 72-600

The wing area behaves the same as the maximum take-off weight, only showing a dependence on the landing field length as shown in Figure 11.9. This is attributed to the same effects as described above.

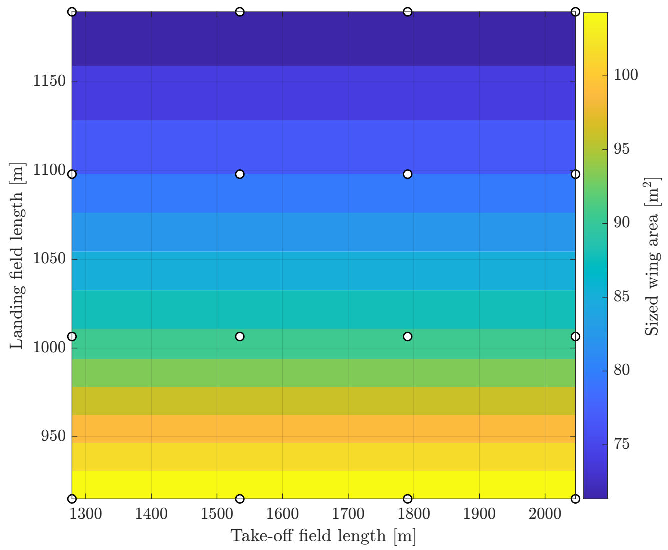

Figure 11.9: Sensitivity of sized wing area to field length requirements for a morphing wing aircraft based on the ATR 72-600

The sensitivities of the wing area and maximum take-off mass show that the decreases in these parameters flatten as the landing field length is relaxed further. The total sized power, however, shows a minimum when the landing field length is relaxed by 20%, as illustrated in Figure 11.10. Again this can be explained based on the wing thrust loading diagram in Figure 11.7. Beyond a wing loading of around $3150\,\mathrm{N\,m^{-2}}$ the one-engine-inoperative balked landing requirement, CS25.121d, becomes power limiting instead of the cruise constraint.

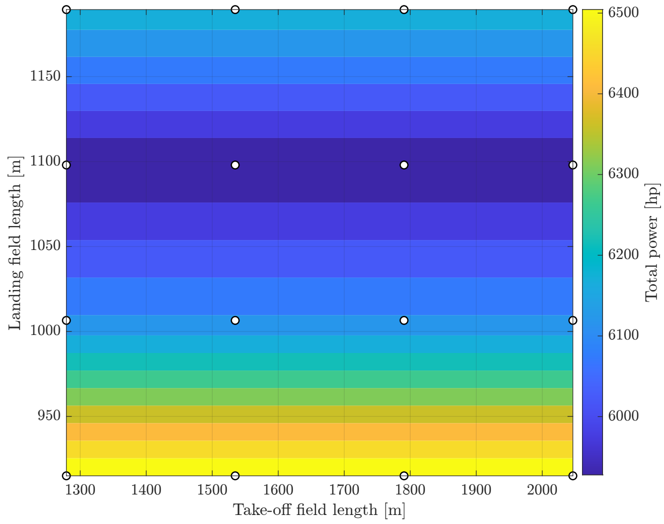

Figure 11.10: Sensitivity of sized total power to field length requirements for a morphing wing aircraft based on the ATR 72-600

11.1.3. Design selection and performance comparison

This subsection presents the performance comparison between a morphing wing ATR 72-600 based aircraft and its conventional counterpart. The selection of a design point is motivated first, based on the sensitivity studies presented in subsection 11.1.2. Given the diminishing returns in the sized wing area and maximum take-off mass, and the increase in power beyond a wing loading of $3150\,\mathrm{N\,m^{-2}}$, the value for the landing field length is set to 120% of the original value, which is equal to $1098\,\mathrm{m}$. Slats are implemented in the morphing wing aircraft given that these result in reduced wing area and total sized power, as shown in Figure 11.5 and Figure 11.6. The morphing system mass is kept at $18\,\mathrm{kg\,m^{-2}}$, as in the sensitivity studies. A side-by-side comparison of the top-level parameters of the morphing wing and conventional aircraft is shown in Table 11.7.

Table 11.7: Comparison of top-level design parameters for the ATR 72-600 based reference and morphing wing conceptual aircraft

Parameter	**Unit**	**Conventional**	**Morphing**	**Difference**
MTOM	kg	23450	23779	+1.4%
OEM	kg	13411	13746	+2.5%
Wing area	$\mathrm{m^2}$	68.63	71.95	+4.8%
Wing span	m	28.70	29.38	+2.4%
Total power	hp	5758.95	5882.10	+2.1%

Using the trimmed performance analysis tool, as detailed in chapter 8, the wing shape of the morphing wing aircraft was optimized in the design condition and for an off-design condition. In the design condition, the aircraft is performing the harmonic mission. It flies at its design cruise altitude and velocity of 24000 feet and 275 knots, at a weight equal to the geometric mean of the take-off mass and landing mass. For the off-design mission, the take-off weight, fuel mass, and mission range were selected from the Class 2 payload range diagram shown in Figure 11.11.

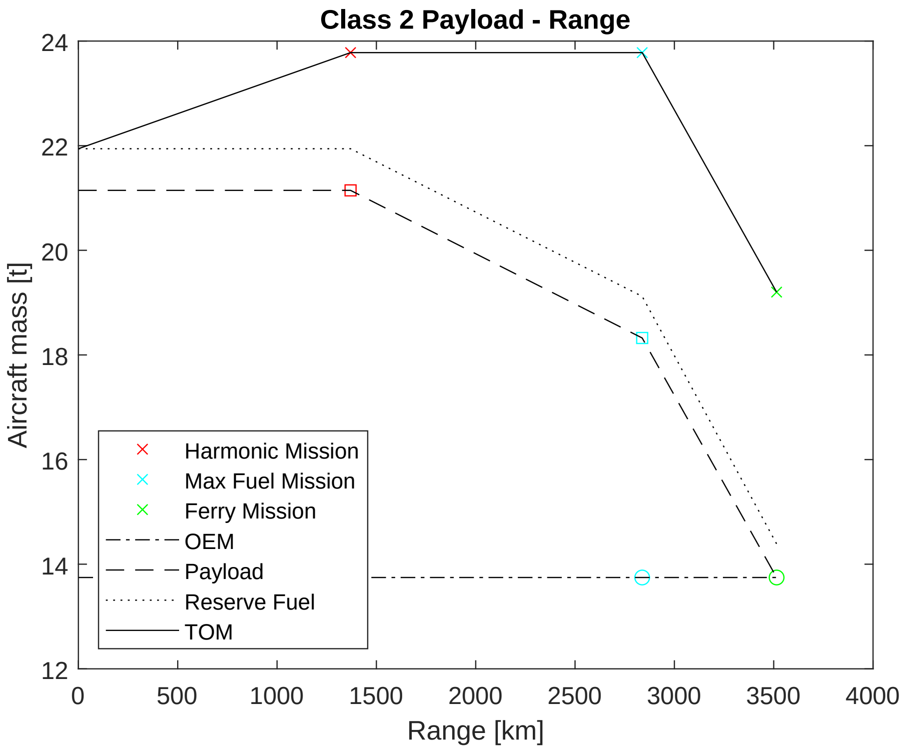

Figure 11.11: Class 2 payload range diagram for morphing wing ATR 72-600 aircraft

Two mission ranges are selected for the off-design performance estimation: a maximum-payload mission with a range of $750\,\mathrm{km}$, and the maximum-fuel mission. Together with the design mission, these represent a shorter and a longer mission relative to the design point. The take-off and fuel masses predicted by the Initiator, used as input here, are shown in Table 11.8. The Initiator predicts a higher fuel burn for the morphing wing aircraft than for the conventional counterpart on every mission. Part of this gap is the weight and power penalty visible in Table 11.7, the remainder is a limitation of the sizing loop. The morphed wing shape is not optimized for every iteration of the Initiator, as this would lead to infeasible runtimes. The aerodynamic benefit of morphing is therefore not yet present in these Initiator figures and is applied as a correction below.

Table 11.8: Take-off and fuel masses for ATR 72-600 on and off design performance comparison

		Take-off mass $[\mathrm{kg}]$	Fuel mass $[\mathrm{kg}]$
Design mission, $R = 1370\,\mathrm{km}$	Conventional	23450	2639
	Morphing	23779	2633
Off-design mission, $R = 750\,\mathrm{km}$	Conventional	22500	1700
	Morphing	22800	1800
Max fuel mission, $R = 2700\,\mathrm{km}$	Conventional	23450	5275
	Morphing	23779	5455

The results of the optimizations are shown in Figure 11.12. The improvement in lift-to-drag ratio is small in every condition considered, at most $+0.5\%$, and is largest for the design mission. As the optimizer reaches a value close to the optimum within roughly 25 iterations, the maximum-fuel mission was run for 100 iterations rather than the 200 used for the design and off-design missions. These modest gains are a further reason for not embedding the wing shape optimization in the Initiator sizing loops.

The traces also show that the conventional aircraft has a lower lift-to-drag ratio in the maximum-fuel and off-design missions than in the design mission, as expected for a fixed wing operating away from its design point. The morphing benefit, however, is *smaller* on these off-design missions than on the design mission. This goes against the expectation that morphing wings are beneficial in off-design conditions by adapting to them. This mechanism was not isolated within the scope of the present study and is left as a point for further investigation.

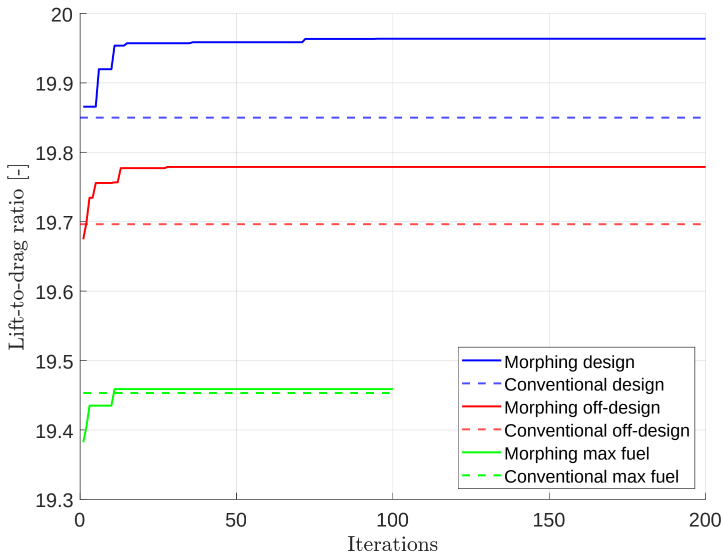

Figure 11.12: Objective trace for Bayesian morphed wing shape optimization in on and off design conditions for an ATR 72-600 based conceptual aircraft design with a morphing wing, compared with a conventional reference design

Using the optimized lift-to-drag ratios, the Initiator fuel masses from Table 11.8 are corrected for the final block-fuel comparison over the three missions. The corrected values are given in Table 11.9. The morphing wing aircraft burns more block fuel on every mission, although the performance over the design mission is nearly the same. This equal performance still comes at the cost of a 20% longer landing field length, and the addition of slats. The top-level parameters in Table 11.7 are close between the two aircraft, but the block-fuel results show that a sizing penalty remains. With the lift-to-drag gains from morphing limited to around 0.5%, that penalty is not recovered aerodynamically.

Table 11.9: Corrected fuel masses for ATR 72-600 on and off design missions and comparison between conventional and morphing aircraft block fuel performance

	Conventional [kg]	Morphing [kg]	Difference
Design mission, $R = 1370\,\mathrm{km}$	2662	2663	+0.04%
Off-Design mission, $R = 750\,\mathrm{km}$	1727	1833	+6.14%
Max Fuel mission, $R = 2700\,\mathrm{km}$	5425	5645	+4.06%

11.2. Fokker 100 case study

The Fokker 100 is a jet transport aircraft which first flew in 1986[4]. It seats up to 109 passengers with a full-payload range of 1350 nautical miles. The maximum take-off weight of the aircraft in the maximum payload configuration is 45 850 kg [64]. The design cruise Mach number and altitude are 0.74 and 10 km. The aircraft is illustrated in Figure 11.13.

4 https://www.fokker-history.com/en-gb/fokker-100, accessed: 01-07-2026

Figure 11.13: Fokker 100 belonging to KLM Royal Dutch Airlines[5]

11.2.1. High-lift performance estimation

The high-lift performance estimation for the Fokker 100 is significantly simpler than that for the ATR 72-600 because of the absence of engines near the wing. Hence, the values derived in chapter 10 are immediately applied. The planform geometry of the aircraft is estimated from three-view drawings, as the exact measurements were not available. The estimated planform geometry is shown in Figure 11.14. In reality, the aileron on the outboard wing does not continue all the way to the wing tip. This was done here as a simplification which has no effect as the morphing trailing edge at the location of the aileron is assumed to not contribute to the high-lift performance.

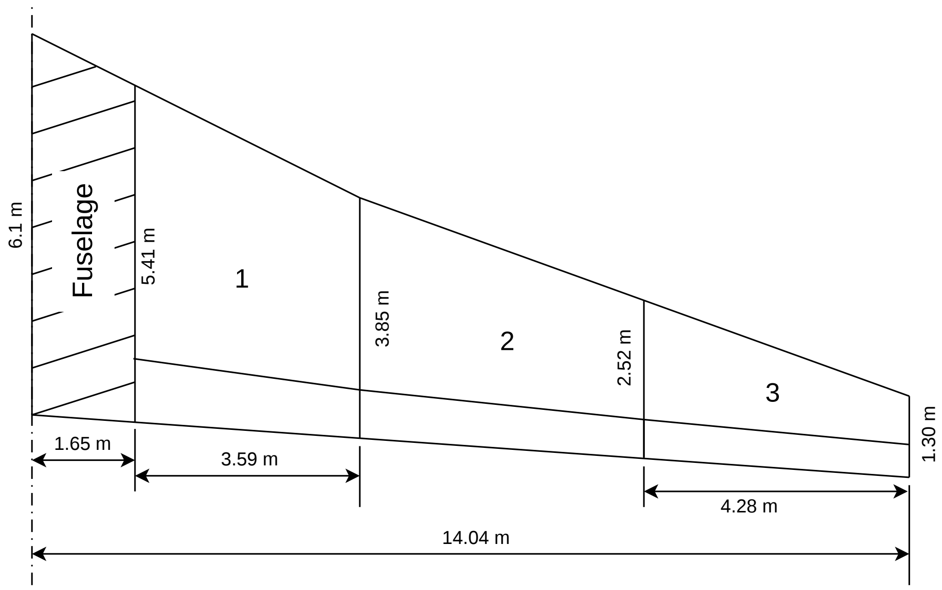

Figure 11.14: Derived wing planform geometry of the Fokker 100

The computation of the high-lift performance of the morphing Fokker 100 wing is summarized in Table 11.10. Note that the sum of the area of the sections is equal to $97.42\,\mathrm{m}^2$ while the reference planform area of the Fokker 100 is $93.5\,\mathrm{m}^2$ [64]. This is due to the fact that the method adopted by Fokker for computation of the wing area excludes any leading- or trailing-edge kinks. As can be seen in Figure 11.14, the Fokker 100 wing has a leading edge kink. This creates a small discrepancy between the computed and reference value for the wing area. The relations by Roskam [32] hold, however, as the resulting lift coefficient increase from the computations is normalized by the same reference area.

Table 11.10: Computation of wing lift increase due to a morphing trailing edge in high-lift configuration for a Fokker 100 wing

Section	S_w [m^2]	$\Lambda_{c/4}$ [deg]	K_Λ [-]	$\Delta C_{l_{max_{TO}}}$ [-]	$\Delta C_{L_{max_{TO}}}$ [-]	$\Delta C_{l_{max_L}}$ [-]	$\Delta C_{L_{max_L}}$ [-]
Fuselage	18.99	21.4	0.8819	0	0	0	0
1	33.24	21.4	0.8819	0.5	0.1568	0.63	0.1975
2	28.82	16.1	0.8989	0.5	0.1385	0.63	0.1745
3	16.37	16.1	0.8989	0	0	0	0
Total	97.42				0.2953		0.3720

As for the ATR 72, the high-lift performance for the Fokker 100 is also computed with the use of slats. The previously used relation based on the sectional maximum lift coefficient can not be applied here, due to the absence of data on the maximum lift coefficient of the airfoil sections that make up the Fokker 100 wing. Hence, a relation presented by Raymer [28] is used, who states that the lift increment is equal to 40% of the ratio of the chord with the slat extended to the basic section chord, which again is assumed to be 10%. The transformation from sectional lift increase to wing lift increase that he uses is slightly different to the one by Roskam [32], as shown in equation (11.3).

$$\Delta C_{L_{max}} = 0.9 \Delta C_{l_{max}} \left(\frac{S_{wf}}{S_w} \right) \cos \Lambda_{HL} \tag{11.3}$$

The sweep term in equation (11.3) is based on the sweep angle of the hinge line instead of the quarter chord sweep line. For the slats, this angle is equal to the leading edge sweep angle. The computation of the lift increase due to slats is summarized in Table 11.11. Note that the lift increase due to slats is now the same for take-off and landing configuration.

Table 11.11: Computation of wing lift increase due to slats for a Fokker 100 wing, following relations by Raymer [28]

Section	S_w	Λ_{LE} [deg]	$\Delta C_{l_{max}}$ [-]	$\Delta C_{L_{max}}$ [-]
Fuselage	18.99	26.6	0	0
1	33.24	26.6	0.44	0.1259
2	28.82	18.8	0.44	0.1156
3	16.37	18.8	0	0.0657
Total	97.42			0.3071

With the clean maximum lift coefficient of the Fokker 100 being 1.72 [64], the resulting maximum lift coefficients in take-off and landing configuration are 2.015 and 2.092 respectively. With the addition of slats, these become 2.322 and 2.4. The take-off maximum lift coefficient with slats exceeds the value of 2.05 of the original aircraft, and matches the landing maximum lift coefficient [64, 326].

11.2.2. Sizing studies

The sizing studies performed on the Fokker 100 aircraft are presented in this subsection. Following the ATR case study, the sensitivities of the maximum take-off mass, sized wing area, and total static thrust to the morphing system specific mass will be presented first. The range considered for the specific mass is the same as for the ATR case, between $10\,\mathrm{kg\,m^{-2}}$ and $30\,\mathrm{kg\,m^{-2}}$. Figure 11.15 illustrates the sensitivity of the maximum take-off mass to the specific mass of the morphing system. As for the ATR case, a quasi-linear relationship between the two parameters can be observed. Both the slatted and non-slatted aircraft are heavier than the reference conceptual design by 1 to 2.5 tonnes.

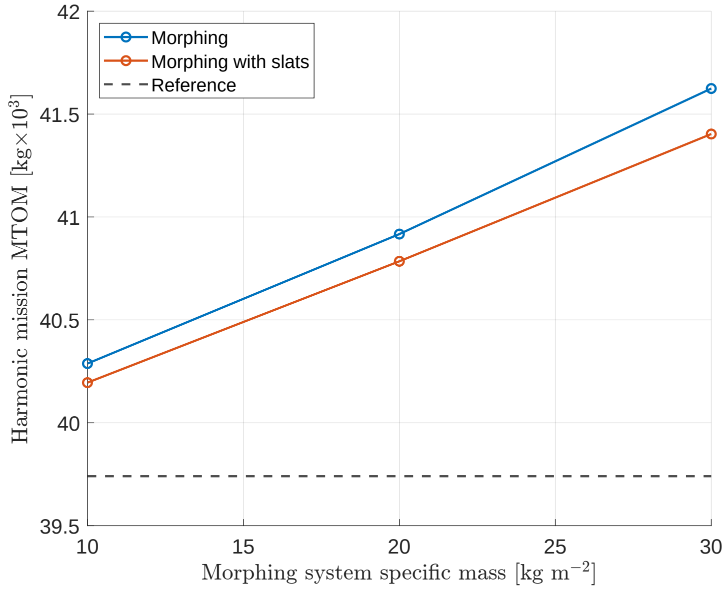

Figure 11.15: Sensitivity of maximum take-off mass to specific morphing system mass for a Fokker 100 based aircraft with a morphing wing

The sensitivity of the wing area to the specific morphing system mass is presented in Figure 11.16. The results show a significantly increased wing area for the morphing wing aircraft without slats by $15\,\mathrm{m}^2$ to $20\,\mathrm{m}^2$ across the range considered. The morphing wing aircraft with slats is much closer to the reference in terms of wing area, which is in line with the increased high-lift performance of the aircraft.

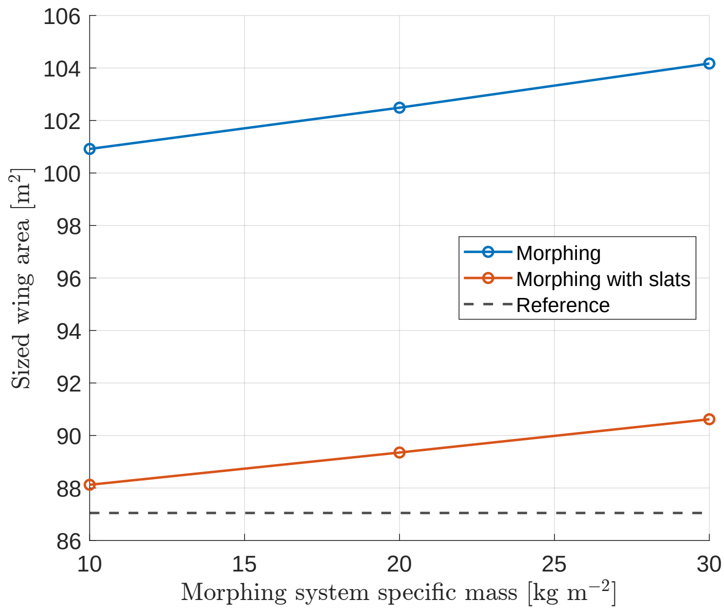

Figure 11.16: Sensitivity of sized wing area to specific morphing system mass for a Fokker 100 based aircraft with a morphing wing

Even though the wing area of the aircraft with slats is close to that of the reference, and significantly smaller than that of the morphing wing aircraft without slats, the maximum take-off masses of the two are relatively close. This can be explained to the sized total static thrust. The sensitivity of the sized total static thrust to the specific morphing system mass is shown in Figure 11.17. Interestingly, the total static thrust sized for the morphing wing aircraft without slats is lower than that of the reference aircraft. This can be explained using the wing-thrust loading diagram in Figure 11.18. The higher wing loading that the aircraft with slats can achieve pushes the landing requirement towards higher wing loading values, which causes the required thrust-to-weight ratio to meet the take-off constraint to increase. This also explains the maximum take-off masses being close. The aircraft without slats suffers from a weight penalty due to its significantly larger wings, while the predicted engine weight on the aircraft with slats is higher due to the higher required thrust.

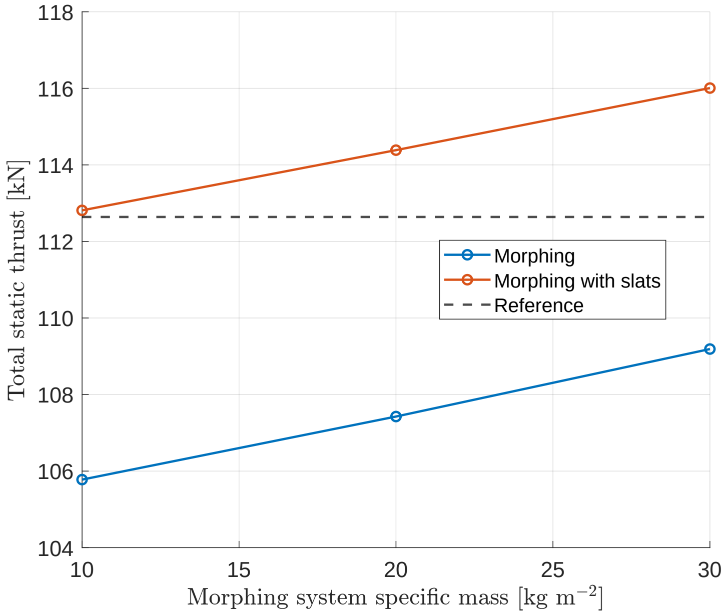

Figure 11.17: Sensitivity of total static thrust to specific morphing system mass for a Fokker 100 based aircraft with a morphing wing

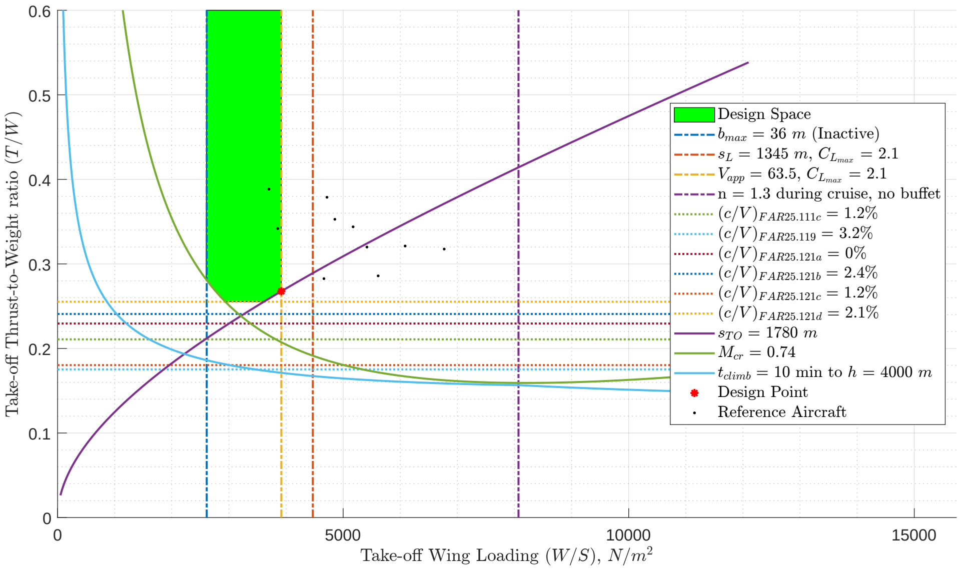

Figure 11.18: Initiator wing-thrust loading diagram for Fokker 100 based aircraft with morphing wing, no slats

The wing-thrust loading diagram presented above, and the sensitivities of the maximum take-off mass, wing area and total thrust indicate that the field performance requirements are limiting. Therefore, the sensitivities of the maximum take-off mass, wing area, and total static thrust to the required field performance will now be characterized, starting with that of the take-off mass in Figure 11.19. The behavior of the MTOM for varying field lengths is as expected. Highly relaxed field lengths lead to a low maximum take-off mass. The effect of the power loading in Figure 11.18 can be seen in the higher maximum take-off mass, even when the landing field length requirement is highly relaxed.

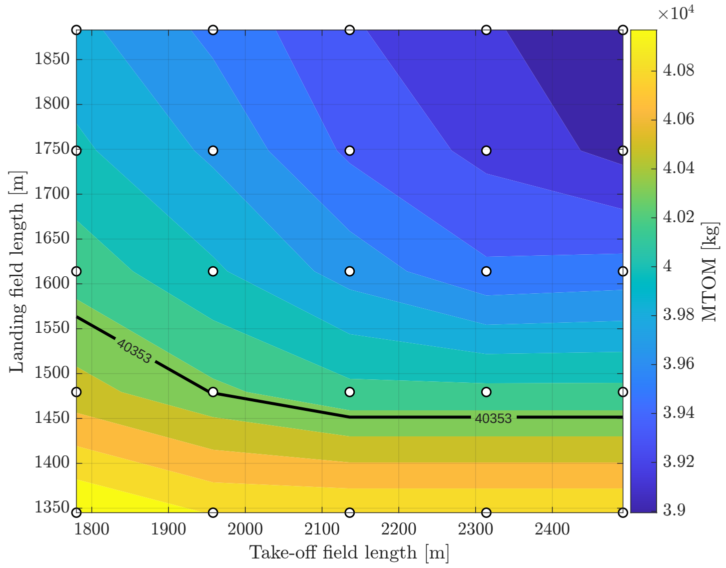

Figure 11.19: Sensitivity of MTOM to field length requirements for Fokker 100 based aircraft with a morphing wing, with reference MTOM in black

The sensitivity of the sized wing area to the field lengths is shown in Figure 11.20. It becomes clear that the landing field length is the driving requirement for the wing area sizing. Only little dependence on the take-off field length is shown, which is driven by increased engine weight at the lower take-off field length requirements. The sized wing area decreases fastest with increasing landing field length at low values of the constraint, which is in line with the results for the ATR.

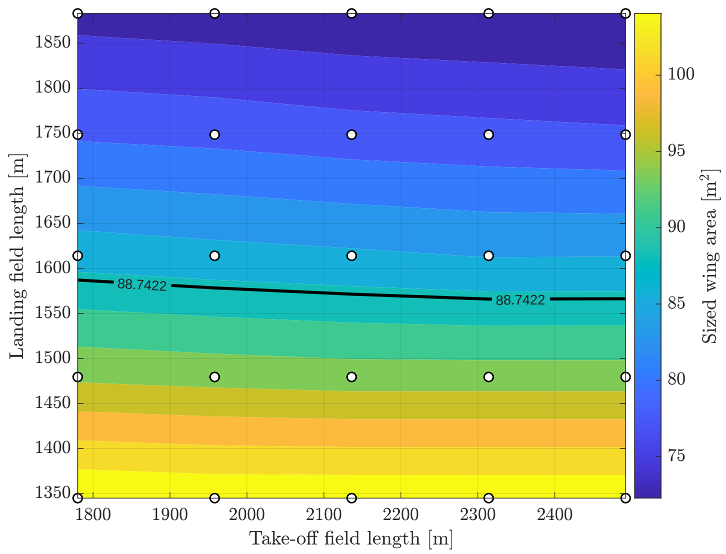

Figure 11.20: Sensitivity of wing area to field length requirements for Fokker 100 based aircraft with a morphing wing, with reference wing area in black

The variation in total static thrust with varying field lengths is presented in Figure 11.21. The sensitivity of the thrust together with that of the wing area explain the behavior of the maximum take-off mass. At the original take-off field length and a highly relaxed landing field length requirement, the sized wing area is small. To meet the take-off field length constraint, the required thrust is high. The sized total static thrust is minimum when the take-off field length constraint is highly relaxed and the landing field length constraint is moderately relaxed. This can be attributed to the wing becoming smaller at higher landing field lengths.

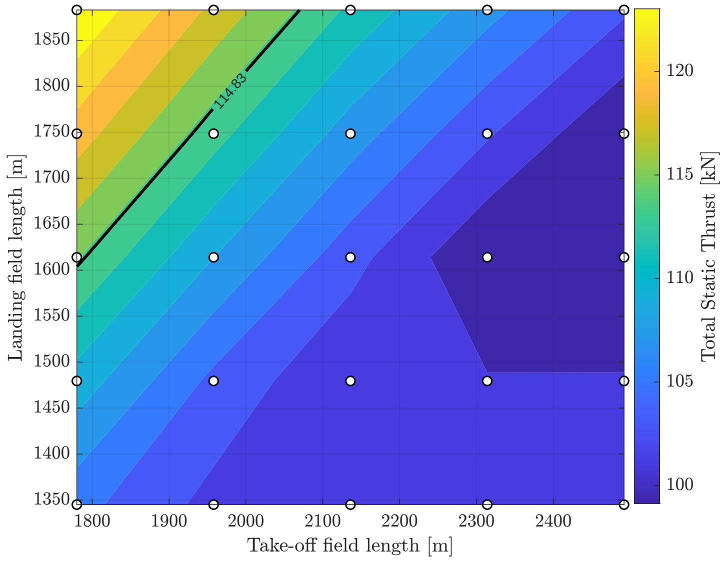

Figure 11.21: Sensitivity of total static thrust to field length requirements for Fokker 100 based aircraft with a morphing wing, with the reference total static thrust in black

11.2.3. Design selection and performance comparison

A new design point will now be chosen for the morphing wing aircraft for the block-fuel performance comparison. The sensitivities of the maximum take-off mass, wing area, and total static thrust include the reference values that were found using the Initiator for the conventional Fokker 100. These indicate that relaxing the take-off and landing field lengths beyond 120% is not necessary, as the maximum take-off mass, wing area, and sized total static thrust are already smaller than that of the conventional design. It is preferred to stay close to the original aircraft, such that the effect of morphing may be isolated. The combination of field lengths chosen is the original take-off field length with a relaxed landing field length of $1580\,\mathrm{m}$, a 17.5% increase over the standard value. This brings the maximum take-off mass, wing area and total sized static thrust closest to that of the reference aircraft, while not deteriorating the field performance by much. The specific morphing system mass chosen in the design for the block fuel comparison is $20\,\mathrm{kg\,m^{-2}}$. This is slightly higher than that of the ATR, to account for the fact that the Fokker flies at higher velocities.

Table 11.12: Comparison of top-level design parameters for the Fokker 100 based reference and morphing wing conceptual aircraft

Parameter	**Unit**	**Conventional**	**Morphing**	**Δ**
MTOM	kg	40353	40309	-0.11%
OEM	kg	22040	21870	-0.77%
Wing area	$\mathrm{m^2}$	88.74	89.02	$+0.32\%$
Wing span	m	27.35	27.39	$+0.15\%$
Total static thrust	kN	114.83	113.93	-0.78%

The missions selected for this case study are based on the results of the ATR case study. The harmonic mission is the design mission for the ATR, of which the results showed that the morphing wing could achieve the largest increase in lift-to-drag ratio for this mission. The Fokker 100 has a design mission that is different from the harmonic mission. This is shown in Table 11.13.

Table 11.13: Take-off and fuel masses for Fokker 100 design and harmonic mission

		Take-off mass [kg]	Fuel mass [kg]	Payload mass [kg]
Design mission, $R = 2500\,\mathrm{km}$	Conventional	40354	7529	10750
	Morphing	40156	7535	10750
Harmonic mission, $R = 1800\,\mathrm{km}$	Conventional	40509	6434	12000
	Morphing	40309	6439	12000

The results of the wing shape optimizations for both missions are shown in Figure 11.22. The increase in lift-to-drag ratio is about 0.4 on both missions, corresponding to 2.78% on the design mission and 2.75% on the harmonic mission. This is a substantially larger benefit than the 0.5% obtained for the ATR 72-600. The Fokker 100 cruises in the transonic regime, where the trailing edge can act on wave and pressure drag in addition to induced and trim drag, whereas the ATR generates no compressibility drag to optimize for. This is consistent with the drag reduction mechanisms set out in chapter 1. The predicted lift-to-drag ratio is slightly higher on the harmonic mission than on the design mission, even though the harmonic mission is flown at a higher lift coefficient (0.4018 against 0.3936). For a fixed wing the higher lift coefficient would be expected to raise the drag coefficient and lower the lift-to-drag ratio, so the ordering is mildly counter-intuitive. The difference is only one drag count, so the effect is minor.

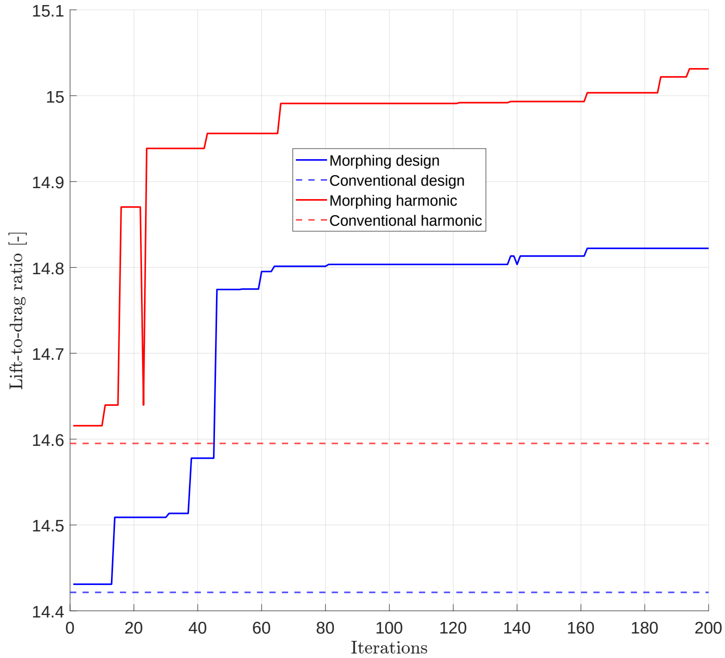

Figure 11.22: Objective trace for Bayesian morphed wing shape optimization in on and off design conditions for a Fokker 100 based conceptual aircraft design with a morphing wing, compared with a conventional reference design

Applying these lift-to-drag ratios, the fuel masses in Table 11.13 are corrected as shown in Table 11.14. The morphing wing Fokker 100 burns 3.2% less block fuel on the design mission and 3.6% less on the harmonic mission. In contrast to the ATR 72-600, where the sizing penalty outweighed the aerodynamic benefit, the transonic Fokker 100 shows a net block-fuel saving from the morphing trailing edge. Still, these savings are only found when accepting a 17.5% landing field length penalty.

Table 11.14: Corrected fuel masses for Fokker 100 design and harmonic missions and comparison between conventional and morphing aircraft block-fuel performance

	Conventional [kg]	Morphing [kg]	Difference
Design mission, $R = 2500\,\mathrm{km}$	9553	9246	-3.21%
Harmonic mission, $R = 1800\,\mathrm{km}$	8099	7807	-3.61%

12
Conclusion & Discussion

The objective of the research presented in the present report was to investigate the effect of implementing compliant chordwise two-degree-of-freedom camber-twist morphing trailing edge wings on the conceptual design and performance of turbine powered aircraft with a maximum take-off mass above $5700\,\mathrm{kg}$ certified under the CS-25 regulations. The main research question connected to this objective is *What is the effect of implementing a two-degree-of-freedom camber-twist morphing trailing edge wing on the block-fuel consumption of a CS-25 transport aircraft over a given mission, compared to a reference aircraft with a conventional wing, when assessed at conceptual design level?*. The block fuel consumption was selected as the figure of merit as it encompasses the trade-off between the increased aerodynamic efficiency and sizing penalties that morphing wings bring. Four supporting sub-questions are identified that need to be addressed before an answer to the main research question can be found, these are:

Q1. How can chordwise 2-DoF camber-twist morphing be parametrized for wings with arbitrary base airfoils using a minimum amount of variables while sufficiently describing the morphed shape space?

Q2. How can the aerodynamic efficiency in cruise of a CS-25 aircraft with a 2-DoF compliant camber-twist morphing trailing edge wing be assessed at conceptual design level, using a method with a runtime in the order of seconds to a minute that resolves relevant drag components?

Q3. How can a CS-25 transport aircraft with a 2-DoF compliant camber-twist morphing trailing edge wing be sized at conceptual design level?

- **Q3.1.** How can the uncertainty in the structural mass prediction of 2-DoF camber-twist morphing trailing edge wings for transport aircraft at conceptual design level be mitigated, given the absence of validated empirical weight models?
- **Q3.2.** What is the $\Delta C_{l_{max}}$ that a morphing airfoil in high-lift configuration can deliver over its baseline configuration, when assessed with high-fidelity methods?

Q4. What is the effect of implementing a 2-DoF compliant camber-twist morphing trailing edge wing on the conceptual-level sizing of a CS-25 transport aircraft, and how sensitive are these outcomes to the mass of the morphing system and to the top-level design requirements?

The conclusions with regards to the sub-questions listed above will be discussed first, followed by the conclusion on the main research question.

Q1: parametrization

A parametrization method for chordwise two-degree-of-freedom (2-DoF) camber morphing was proposed. The method describes the morphed shape of an arbitrary base airfoil from three inputs: the chordwise location of the rear spar and two pseudo-deflection angles. Three control points are placed on the camberline of the airfoil, at the rear spar, the trailing edge, and the mid-point between them. The mid and trailing edge control points are rotated in sequence by the two pseudo deflection angles, after which a fourth-order polynomial is fit through the resulting control points under first-order continuity at the rear spar and a specified trailing edge slope. The airfoil surfaces are then reconstructed from the morphed camberline using the original thickness distribution, which is scaled iteratively such that the arc length of the suction side skin is preserved. This preservation reflects the physical constraint of the compliant morphing structure under study.

The method requires the camber and thickness distributions of the base airfoil, which are extracted using the Class-Shape Transformation (CST) technique when smooth analytical descriptions are not available. Residual CST fitting errors are eliminated by refitting a high-order CST representation on the morphed geometry resulting in aerodynamically equivalent airfoils, which was verified using the two-dimensional viscid-inviscid panel code Xfoil.

The method is applied a specified number of times along the span to represent camber-twist morphing at wing level, with the wing geometry generated by linear interpolation between the parametrized sections. This mimics the physical coupling between camber and twist morphing in the concept under study, where twist is realized through differential camber actuation across the span. The parametrization is used in the aerodynamic analysis, in the CFD-based high-lift study, and in the sizing pipeline of the present research.

Q2: aerodynamic analysis & optimization

The Aircraft Trimmed Performance Analysis Tool (ATPAT) was developed to analyze and optimize the aerodynamic efficiency of morphing wing aircraft in cruise. ATPAT is based on quasi-three-dimensional (Q3D) aerodynamic analysis, which combines the vortex lattice method with strip theory and simple sweep theory. The three-dimensional vortex lattice analysis provides the induced drag of the aircraft and the lift distributions over its lifting surfaces. The operating conditions of a set of spanwise strips are derived from these lift distributions through simple sweep theory, accounting for wing taper. Two-dimensional viscous airfoil analysis is used to compute the viscous, pressure, and, in transonic conditions, wave drag at each strip, which is combined with the induced drag to yield the total aircraft drag. ATPAT optionally models the effect of the fuselage on the aerodynamic moment and drag.

ATPAT was validated against experimental and computational data provided by Fokker on the geometry of the Fokker 100. The predicted drag values showed good agreement in low- and high-speed conditions, and the moment prediction was sufficiently accurate in the cruise lift coefficient range for which the tool is developed. The tool meets the runtime target of seconds to a minute per evaluation, which is the requirement that enables its use inside optimization loops.

ATPAT was integrated into the Initiator aircraft design toolbox at the Delft University of Technology's faculty of aerospace engineering, and combined with both Bayesian and gradient-based unconstrained optimization algorithms. In this configuration it is used for the morphed wing shape optimizations that produce the aerodynamic results supporting the main research question.

Q3: Sizing methodology and inputs

Two inputs to the conceptual sizing of a morphing wing aircraft have no empirical basis for morphing systems. The first is the structural mass of the wing, and the second is the achievable high-lift performance of the morphing airfoils. The sub-questions of Q3 address these gaps.

The uncertainty in the structural mass is handled by treating the morphing system mass as a parameter rather than a point estimate. A range of values for the specific morphing system mass in $\mathrm{kg\,m^{-2}}$ is adopted, with the upper bound set at the specific mass of Fowler flaps for the reference aircraft. This is a conservative upper bound because Fowler flaps rely on distinct sub-surfaces and mechanisms that a compliant morphing structure does not require. The morphing system mass is combined with a Class 2 structural mass estimation that sizes the basic wing structure to resist the root bending moment in a critical load condition. The resulting wing structural mass varies with both the specific morphing system mass and the sized wing area.

The achievable maximum lift coefficient of a morphing airfoil in high-lift configuration was assessed with RANS CFD using the $k-\omega$ SST turbulence model. Morphing airfoils based on the NACA 63412 and NACA 43015 were analyzed at moderate and high trailing edge deflections. The results were compared to the conceptual estimation relationships for plain flaps, which are the most similar conventional high-lift devices to morphing trailing edges. No consistent trend was found in how the morphing airfoils compare to these relationships. The applicability of the plain flap relations to this study is questioned, as these ignore key airfoil characteristics like the camber distribution of the base airfoil. On the basis of the CFD results and a conservative deficit assumption, a maximum sectional lift increment of $\Delta C_{l_{max}} = 0.63$ is adopted for morphing trailing edges at full deflection, corresponding to a 30% deficit relative to plain flap predictions.

To support the sizing of morphing wing aircraft, the Initiator aircraft design toolbox was expanded to integrate the geometric modeling of morphing, per the parametrization method described in Q1, and the structural mass estimation described above, enabling the sizing studies presented in Q4.

Q4: Sizing studies

The sizing studies were performed on two CS-25 reference aircraft, the ATR 72-600 and the Fokker 100. The ATR 72-600 was chosen because its short standard field length requirements leave room to relax them in the sensitivity studies, since the aircraft frequently operates from airports where such short field lengths are not required. The Fokker 100 was chosen because it is the only CS-25 aircraft certified to take off without deployment of high-lift devices, which reduces the impact of the high-lift deficit on the sizing outcome. Both reference aircraft were sized in the Initiator aircraft design toolbox, with the morphing wing integrated through the parametrization of Q1, the aerodynamic analysis of Q2, and the mass and high-lift inputs above.

When subjected to the same top-level aircraft requirements, both the ATR 72-600 and Fokker 100 based morphing aircraft have a significantly higher take-off weight and higher wing area. This is a direct consequence of the deficit in high-lift performance that these aircraft have compared to their conventional counterparts. The field performance constraints can be said to be the limiting ones for morphing wing aircraft. The sensitivity of the sizing outcomes to variation in these field length requirements show that feasible aircraft designs with similar top-level sizing results can be sized when accepting worse field performance. Both the ATR 72-600 and Fokker 100 only needed a moderate relaxation of 20% of the landing field length requirement for the sizing results to be close to that of the original aircraft. Compliant morphing trailing edge wings for transport aircraft can therefore not be dismissed based on the field length requirements being limiting.

The dependence of the maximum take-off mass, sized wing area, and total power or total thrust on the specific mass of the morphing system is quasi linear for both aircraft. The maximum take-off mass was found to be most sensitive to this parameter, spanning a range of around 1.5 tonnes over the range of morphing system masses considered.

Main research question

The effect of implementing morphing trailing edge wings on the block-fuel consumption of a CS-25 aircraft depends on the aircraft. On the ATR 72-600, the aerodynamic improvements due to morphing are not substantial enough to justify the 20% increased landing field length and the addition of slats. Although the sizing penalties are small with these changes, they still outweighed the increase in lift-to-drag ratio in cruise. At best the morphing wing version of the ATR was shown to match the block-fuel performance of the conventional conceptual design over the harmonic mission. Over a shorter maximum payload mission of $750\,\mathrm{km}$ and over its maximum fuel mission, the aircraft used 6% and 4% more fuel than the conventional design.

The Fokker 100 did show improvements in the block fuel consumption of up to 3.6% over its harmonic mission. To achieve this, the landing field length requirement had to be relaxed by 17.5%, which resulted in the morphing wing aircraft being sized practically equally to the conventional reference aircraft. Because of this, the aerodynamic gains carried through to the block-fuel performance. An additional advantage for the morphing wing Fokker is that it operates in transonic conditions. Here, camber morphing can be employed to reduce wave drag, offering an additional pathway towards lower overall drag.

12.1. Discussion & future work

This section places the conclusions of the previous section in context, identifies the assumptions on which the main finding is conditional, and formulates recommendations for follow-up research.

Mechanism behind the block-fuel benefit on the Fokker 100

The main-question answer attributes the block-fuel savings on the Fokker 100 partly to the near-equal sizing between the morphing and reference designs, and partly to the availability of an additional drag reduction pathway through wave drag in transonic cruise. The relative contribution of each has not been isolated in the present research. The wing shape optimizations performed with ATPAT reported total drag as the objective, and the drag breakdown at each optimum was not analyzed component by component. A follow-up study that decomposes the optimized drag into induced, viscous, pressure, and wave contributions would identify how much of the observed benefit comes from wave drag reduction and how much from the other components. If wave drag reduction is the dominant contributor, the finding transfers to other transonic transport aircraft. If it is not, the mechanism is likely tied to the specific cruise lift coefficient of the Fokker 100 and does not transfer as cleanly. This distinction matters for the practical relevance of the technology and should be the first follow-up performed.

Morphing system mass

The main finding depends on the assumed range of specific morphing system masses. The upper bound was set at the specific mass of Fowler flaps for the reference aircraft, which is a conservative but not physically grounded value. The dependence of the maximum take-off mass on the specific morphing system mass was shown to be approximately linear, and the total spread over the range considered was around 1.5 tonnes on both platforms. If the true specific mass of a full-scale compliant morphing trailing edge system falls outside this range, the block-fuel finding shifts accordingly. Validated empirical mass data from a full-scale compliant morphing wing demonstrator would remove the largest single source of uncertainty in the present analysis. In the absence of such data, the parametric treatment adopted here is the appropriate handling at conceptual design level.

High-lift performance

The high-lift performance of compliant morphing trailing edge wings was estimated from Computational Fluid Dynamics simulations based on the Reynolds-Averaged Navier-Stokes equations on two morphing configurations across two baseline airfoils. The results only supported a conservative lower bound for the sectional lift increase due to a morphing trailing edge of 0.63 at full deflection, which drove the field performance to be limiting in the sizing of morphing wing aircraft. Two airfoils are not enough to defend this bound across the CS-25 category, and it may overestimate the sizing penalty. Additional CFD simulations across a broader set of baseline airfoils would tighten the bound. Wind tunnel experiments are preferred over further CFD because accurate prediction of stall in RANS is cumbersome and adds a source of uncertainty of its own.

Scope of the case studies

The main finding is based on two aircraft, one turboprop regional and one narrow-body jet. Although these two aircraft were selected with a grounded reason based on the expected deficit in high-lift performance, CS-25 covers a broader range of aircraft than these two data points represent. Extending the analysis to a modern narrow-body jet operating at higher cruise Mach numbers, and to a wide-body long-haul aircraft, would test whether the finding generalizes across the certification category. The Fokker 100 is representative of an older generation of jet transport and is not the strongest reference for what morphing could achieve on a modern platform.

Mission analysis

The block-fuel performance for both aircraft was assessed using the Breguet range equation on a single cruise point per mission. This does not capture the variation in weight and altitude across the cruise segment, both of which affect the achievable morphing benefit through their effect on cruise lift coefficient. A segmented Breguet analysis, in which the cruise is divided into several sub-segments each with its own morphing optimization, is likely to produce a more accurate block-fuel estimate. This refinement likely increases the estimated performance benefits of morphing.

A

ATPAT

```
%% Definition of lifting surface geometry

Nsurf = 2;                      % Number of lifting surfaces in the
    analysis; 2 for main wing & horizontal tail
AC.Wing = cell(1, Nsurf);       % Define AC.Wing cell array

% Location of the aircraft's center of gravity
AC.CG_percent_MAC = 7;          % percentage of the mean aerodynamic chord
     (x)
AC.CG_z = 1.95;                  % z coordinate of aircraft cg

% Aircraft mass
AC.mass = 40000.0;

AC.CDmisc = 0.00487;

% ---------------- Main Wing ------------------
AC.Wing{1}.ID = 'MainWing';             % Wing identifier

% Location of the leading edge of the root of the wing
AC.Wing{1}.Root_LE = struct(...
    'x', 13.99, ...
    'y', 0.0, ...
    'z', 1.95);

% AVL discretisation parameters
AC.Wing{1}.AVL.nchord = 10;
AC.Wing{1}.AVL.nspan = 24;
AC.Wing{1}.AVL.index = 1;

% Number of sections perpendicular to quarter chord for 2d viscous
    analysis
AC.Wing{1}.num_perp_sec = 9;
AC.Wing{1}.xi_c = 0.5;

% Planform geometry (w.r.t Root_LE)
%                    x    y     z    c(m)  twist angle (deg)
AC.Wing{1}.Geom = [-0.72 0.0   0.0   5.91  0.0;
                    0.0  1.25  0.0   5.43  3.5;
```

```
                    1.62 5.1   0.26 3.88  2.8;
                    4.76 14.04 0.91 1.32 -0.13];
AC.Wing{1}.firstSecInFus = true;

% Incidence angle
AC.Wing{1}.inc = 0.0;

% Define airfoils
airfoilNumPoints = 100;

AC.Wing{1}.Airfoils(1) = struct(...
    'eta', 0.0, ...
    'CST', [ 0.1606  0.1194  0.1836  0.1782   0.1064  0.1492;
            -0.1604 -0.1176 -0.2095 -0.2150  -0.1148 -0.0916], ...  % -0.20 -0.17 -0.22 -0.10 -0.25 -0.09 -0.225
    'numPoints', airfoilNumPoints);

AC.Wing{1}.Airfoils(2) = struct(...
    'eta', 0.089, ...
    'CST', [ 0.1606  0.1194  0.1836  0.1782   0.1064  0.1492;
            -0.1604 -0.1176 -0.2095 -0.2150  -0.1148 -0.0916], ...
    'numPoints', airfoilNumPoints);

AC.Wing{1}.Airfoils(3) = struct(...
    'eta', 0.363, ...
    'CST', [ 0.2018  0.1318  0.2326  0.2387   0.1548  0.2553;
            -0.1191 -0.0546 -0.1768 -0.2071  -0.0880  0.0161], ...
    'numPoints', airfoilNumPoints);

AC.Wing{1}.Airfoils(4) = struct(...
    'eta', 1.0, ...
    'CST', [ 0.1809  0.1316  0.1573  0.1718  0.1566  0.1606;
            -0.1655  0.0419 -0.1638 -0.1560  0.0579 -0.1200], ...
    'numPoints', airfoilNumPoints);

% ------------- Horizontal Tail --------------
AC.Wing{2}.ID = 'HorizontalTail';

% Location of the leading edge of the root of the wing
AC.Wing{2}.Root_LE = struct(...
    'x', 31.39, ...
    'y', 0.0, ...
    'z', 8.08);

% AVL discretisation parameters
AC.Wing{2}.AVL.nchord = 8;
AC.Wing{2}.AVL.nspan = 14;
AC.Wing{2}.AVL.index = 2;

% Number of sections perpendicular to quarter chord for 2d viscous analysis
AC.Wing{2}.num_perp_sec = 4;
AC.Wing{2}.xi_c = 0.5;

% Planform geometry (w.r.t Root_LE)
%                  x    y    z    c(m) twist angle (deg)
```

```
AC.Wing{2}.Geom = [0.0  0.0  0.0  3.07 0.0;
                   % 2.52 4.28 0.0  1.47 0.0;
                   2.95 5.02 0.0  1.19 0.0];

AC.Wing{2}.firstSecInFus = false;

% Incidence angle
AC.Wing{2}.inc = 0.0;

airfoilNumPoints = 80;

AC.Wing{2}.Airfoils(1) = struct(...
    'eta', 0.0, ...
    'CST', [0.1363  0.1481  0.0968  0.1618  0.0774  0.1552; ...
           -0.1363 -0.1481 -0.0968 -0.1618 -0.0774 -0.1552], ...
    'numPoints', airfoilNumPoints);

AC.Wing{2}.Airfoils(2) = struct(...
    'eta', 1.0, ...
    'CST', [0.1363  0.1481  0.0968  0.1618  0.0774  0.1552; ...
           -0.1363 -0.1481 -0.0968 -0.1618 -0.0774 -0.1552], ...
    'numPoints', airfoilNumPoints);

AC.Wing{2}.Control(1) = struct(...
                    'sec_idx', 1, ...          % section index (in Wing.Geom)
                    'ID',       'trimTail', ... % control surface ID
                    'gain',     1.0, ...        % deflection gain
                    'Xhinge',   0.0, ...       % hinge location on chord
                    'Xhvec',    0.0, ...
                    'Yhvec',    1.0, ...
                    'Zhvec',    0.0, ...
                    'SgnDup',   1 );

AC.Wing{2}.Control(2) = struct(...
                    'sec_idx', 2, ...          % section index (in Wing.Geom)
                    'ID',       'trimTail', ... % control surface ID
                    'gain',     1.0, ...        % deflection gain
                    'Xhinge',   0.0, ...       % hinge location on chord
                    'Xhvec',    0.0, ...
                    'Yhvec',    1.0, ...
                    'Zhvec',    0.0, ...
                    'SgnDup',   1 );

% Engine (OPTIONAL: if this field is present, it is taken into account
% in trim calculations)
AC.Engine = struct(...
    'x', 25.32, ...              % x position of the engines
    'z', 3.36, ...               % z position of the engines
    'i_h', 1.5, ...              % angle of incidence of the engine (positive is rear down)
    'maxThrust', 61600.0);       % [N] maximum thrust that engines can deliver

% Fuselage (OPTIONAL: if this field is present, it is taken into account
```

```
% in trim calculations)
% IMPORTANT: Refer to "Fuselage aerodynamic prediction methods" by:
% Nicolosi, F.; Della Vecchia, P.; Ciliberti, D.; Cusati, V.;
% to obtain the figures in the struct
AC.Fuselage = struct(...
    'i_f', -1.045, ...            % [deg] fuselage angle w.r.t horizontal
    'l_fus', 32.501, ...          % [m], fuselage length
    'd_fus', 3.30, ...
    'Swet', 292.61, ...           % [m^2], fuselage wetted area
    'Swet_n', 27.26, ...         % [m^2], nose wetted area
    'l_n', 4.80, ...
    'Swet_c', 196.92, ...         % [m^2], nose wetted area
    'Swet_t', 68.43, ...          % [m^2], nose wetted area
    'l_t', 8.98, ...
    'windshieldAngle', 42.0, ...
    'upsweepAngle', 12.0);
```

B

High lift study

OpenFOAM boundary conditions for flow parameters in CFD study

- U
  - Inlet, Farfield: freestreamVelocity
  - Airfoil: noSlip
  - Side: empty
- p
  - Inlet, Farfield: freestreamPressure
  - Airfoil: zeroGradient
  - Side: empty
- k
  - Inlet, Farfield: inletOutlet
  - Airfoil: fixedValue
  - Side: empty
- ω
  - Inlet, Farfield: inletOutlet
  - Airfoil: omegaWallFunction
  - Side: empty
- ν_t
  - Inlet, Farfield: inletOutlet
  - Airfoil: nutLowReWallFunction
  - Side: empty
- γ_{int}*
  - Inlet, Farfield: inletOutlet
  - Airfoil: zeroGradient
  - Side: empty
- Re_θ*
  - Inlet, Farfield: inletOutlet

- Airfoil: zeroGradient
- Side: empty

**Only for Langtry-Menter extension of* $k - \omega$ *SST model*

Table B.1: OpenFOAM Scheme settings for CFD simulations

Term	**OpenFOAM keyword**	**Scheme**	**Order**
Time derivative	ddtSchemes	localEuler	1st
Convection	div(phi,U)	Gauss linearUpwind	2nd
Diffusion	div(nuEff*dev2(T(grad(U)))	Gauss linear	2nd
Gradient	gradSchemes	Gauss linear	2nd
Laplacian	laplacianSchemes	Gauss linear corrected	2nd
Interpolation	interpolationSchemes	linear	2nd
Surface normal gradient	snGradSchemes	corrected	2nd

Bibliography

[1] Airbus S.A.S., *Global Market Forecast 2025*, Tech. Rep. (Airbus S.A.S., Toulouse, France, 2025).

[2] International Air Transport Association (IATA), *Aircraft Technology Net Zero Roadmap*, Tech. Rep. (International Air Transport Association (IATA), 2023) accessed: 2025-10-15.

[3] A. Concilio, I. Dimino, L. Lecce, and R. Pecora, *Morphing Wing Technologies: Large Commercial Aircraft and Helicopters* (Butterworth-Heinemann, Oxford, United Kingdom, 2018).

[4] T. A. Weisshaar, *Morphing aircraft systems: Historical perspectives and future challenges,* Journal of Aircraft **50**, 337 (2013), accessed: 2025-10-15.

[5] W. Niu, Y. Zhang, H. Chen, and M. Zhang, *Numerical study of a supercritical airfoil/wing with variable-camber technology,* Chinese Journal of Aeronautics (2020).

[6] P. Georgopoulos, J. Sodja, and R. de Breuker, *Camber-twist morphing flap concept with two chordwise degrees-of-freedom,* Journal of Intelligent Material Systems and Structures (2025).

[7] European Union Aviation Safety Agency, *Certification Specifications for Large Aeroplanes (CS-25)*, Tech. Rep. (European Union Aviation Safety Agency, 2023).

[8] European Union Aviation Safety Agency, *Definitions and Abbreviations Used in Certification Specifications for Products, Parts and Appliances (CS-Definitions), Amendment 1*, Tech. Rep. (European Union Aviation Safety Agency, 2007).

[9] T. A. Weisshaar, *Morphing Aircraft Technology – New Shapes for Aircraft Design*, Tech. Rep. RTO-MP-AVT-141 (North Atlantic Treaty Organization, Neuilly-sur-Seine, France, 2006).

[10] S. Barbarino, O. Bilgen, R. M. Ajaj, M. I. Friswell, and D. J. Inman, *A review of morphing aircraft,* Journal of Intelligent Material Systems and Structures **22**, 823 (2011).

[11] E. Torenbeek, *Synthesis of Subsonic Airplane Design* (Delft University Press, Martinus Nijhoff Publishers, 1982).

[12] J. Roskam, *Proceedings of the nasa · industry · university general aviation drag reduction workshop,* in *Session V - Trim Drag*, edited by J. Roskam (NASA and Univeristy of Kansas, Lawrence, Kansas, 1975) pp. 293–319.

[13] The Boeing Company, *Boeing history chronology,* The Boeing Company (2024).

[14] Airbus S.A.S., *Our product: History,* Airbus S.A.S. (2025).

[15] Embraer S.A., *The E195 is celebrating a birthday!* Embraer Commercial Aviation (2016).

[16] J. R. Martins, *Fuel burn reduction through wing morphing,* Encyclopedia of Aerospace Engineering, Green Aviation , 75 (2016).

[17] R. Pecora, *Morphing wing flaps for large civil aircraft: Evolution of a smart technology across the clean sky program,* Chinese Journal of Aeronautics **34**, 13 (2020).

[18] R. Pecora, F. Amoroso, and F. Amendola, *Validation of a smart structural concept for wing-flap camber morphing,* Smart Structures and Systems **14** (2014), https://doi.org/10.12989/sss.2014.14.4.659.

[19] S. Ameduri, B. Galasso, M. C. Noviello, I. Dimino, A. Concilio, P. Catalano, F. A. D'Aniello, G. M. Carossa, L. Pinazo, J. Derry, B. Biju, and S. Shreedharan, *Design and optimization of a compliant morphing trailing edge for high-lift generation,* MDPI applied sciences **15** (2025), 10.3390/app15052529.

[20] T. Mkhoyan, N. Thakrar, R. de Breuker, and J. Sodja, *Design of a smart morphing wing using integrated and distributed trailing edge camber morphing,* in *Proceedings of the ASME 2020 Conference on Smart Materials, Adaptive Structures and Intelligent Systems* (2020).

[21] S. Cortez, S. Winyangkul, and S. Sleesongsom, *The conceptual design of a variable camber wing,* Biomimetics **10** (2025).

[22] M. Giuliani, I. Dimino, S. Ameduri, R. Pecora, and A. Concilio, *Status and perspectives of commercial aircraft morphing,* Biomimetics **7** (2022), https://doi.org/10.3390/biomimetics7010011.

[23] M. Orlita and R. Vos, *Cruise performance optimization of the airbus a320 through flap morphing,* in *17th AIAA Aviation Technology, Integration, and Operations Conference* (American Institute of Aeronautics and Astronautics AIAA, 2017).

[24] G. E. Fujiwara, N. T. Nguyen, E. Livne, and M. B. Bragg, *Aerostructural design optimization of flexiblewing aircraft with continuous morphing trailing edges,* in *Proceedings of the 2018 Multidisciplinary Analysis and Optmization Conference* (American Institute of Aeronautics and Astronautics, 2018).

[25] J. P. Jasa, J. T. Hwang, and J. R. R. A. Martins, *Design and Trajectory Optimization of a Morphing Wing Aircraft*, Tech. Rep. (University of Michigan Department of Aerospace Engineering, 2018).

[26] R. Elmendorp, *Synthesis of Novel Aircraft Concepts for Future Air Travel*, Master's thesis, Delft University of Technology (2014).

[27] J. Roskam, *Airplane Design Series*, Airplane Design (DARcorporation, Lawrence, Kansas, 1985) 8 volumes, 1985-1997.

[28] D. Raymer, *Aircraft Design: A Conceptual Approach*, Vol. 6 (American Institute of Aeronautics and Astronautics, 2018).

[29] S. Stückl, *Methods for the Design and Evaluation of Future Aircraft Concepts Utilizing Electric Propulsion Systems*, Ph.D. thesis, Technische Universität München (2016).

[30] J. Roskam, *Airplane Design Part I: Preliminary Sizing of Airplanes*, Airplane Design, Vol. 1 (DARcorporation, Lawrence, Kansas, 1985).

[31] R. Vos, *Airplane design and analysis,* (2025), draft version.

[32] J. Roskam, *Airplane Design Part II: Preliminary Configuration Design and Integration of the Propulsion System*, Airplane Design, Vol. 2 (DARcorporation, Lawrence, Kansas, 1997).

[33] D. Scholz, *Lecture Notes: High Lift Systems and Maximum Lift Coefficients*, Tech. Rep. (Hamburg University of Applied Sciences, 2015).

[34] H. Kamliya Jawahar, Q. Ai, and M. Azarpeyvand, *Experimental and numerical investigation of aerodyanmic performance for airfoils with morphed trailing edges,* Renewable Energy (2018).

[35] M. Nemati and A. Jahangirian, *Robust aerodynamic morphing shape optimization for high-lift missions,* Aerospace Science and Technology **103** (2020).

[36] J. Roskam, *Airplane Design Part V: Component Weight Estimation*, Airplane Design, Vol. 5 (DARcorporation, Lawrence, Kansas, 2018).

[37] H. Mulder, *Modular Initiator Modeling of Engines*, Master's thesis, Delft University of Technology (2018).

[38] S. Wöhler, G. Atanasov, D. Silberhorn, B. Fröhler, and T. Zill, *Preliminary aircraft design within a multidisciplinary and multifidelity design environment,* in *Proceedings of the 2020 Aerospace Europe Conference* (2020).

[39] W. Mason, *Applied Computational Aerodynamics: Foundations and Classical Pre-CFD Methods*, Vol. 1 (Cambridge University Press, 1997).

[40] F. Johnson, S. Samant, M. Bieterman, R. Melvin, D. Young, J. Bussoletti, and C. Hilmes, *TranAir: A Full-Potential, Solution-Adaptive, Rectangular Grid Code for Predicting Subsonic, Transonic, and Supersonic Flows About Arbitrary Configurations*, Tech. Rep. NASA/CR-4349 (National Aeronautics and Space Administration, 1992).

[41] A. van der Wees and J. van Muijden, *A Robust Quasi-Simultaneous Interaction Method for a Full-Potential Flow with a Boundary Layer with Application to Wing/Body Configurations*, Tech. Rep. N93-27465 (National Aerospace Laboratory NLR, 1993).

[42] J. Mariëns, *Wing Shape Multidisciplinary Design Optimization*, Master's thesis, Delft University of Technology (2012).

[43] J. Katz and A. Plotkin, *Low-Speed Aerodynamics*, 2nd ed. (Cambridge University Press, 2001).

[44] J. R. Martins and A. Ning, *Engineering Design Optimization* (Cambridge University Press, 2021).

[45] P. I. Frazier, *A tutorial on bayesian optimization,* (2018), arXiv:1807.02811 [stat.ML] .

[46] H. Maathuis, *Constrained Bayesian Optimisation in High-Dimensional Spaces*, Ph.D. thesis, Delft University of Technology (2026).

[47] J. D. Anderson, *Fundamentals of Aerodynamics*, Vol. 5 (McGraw-Hill, 2011).

[48] M. F. Niţă, *Aircraft Design Studies Based on the ATR 72*, Tech. Rep. (Hamburg University of Applied Sciences, 2008) supervised by Prof. Dr.-Ing. Dieter Scholz,.

[49] Avions de transport régional, *ATR72-600 fact sheet*, Tech. Rep. (Avions de transport régional, 2020).

[50] Airbus S.A.S., *Airbus A380 Airplane Characteristics Airport and Maintenance Planning*, Tech. Rep. (Airbus S.A.S., 2020).

[51] Airbus, *A380 facts and figures*, Tech. Rep. (Airbus, 2021).

[52] M. D. Maughmer and J. G. Coder, *Comparisons of Theoretical Methods for Predicting Airfoil Aerodynamic Characteristics*, Tech. Rep. RDECOM TR 10-D-106 (U.S. Army Research, Development, and Engineering Command (RDECOM), Fort Eustis, VA 23604-5577, 2010) accessed: 2025-10-29.

[53] L. Dong, I. Men'shov, and Y. Nakamura, *Numerical prediction for airfoil stall,* in *Proceedings of the 24th International Congress of Aeronautical Sciences* (2004).

[54] D. C. Wilcox, *Turbulence Modeling for CFD* (DCW Industries, 2006).

[55] C. L. Rumsey and S. X. Ying, *Prediction of high lift: Review of present CFD capability,* Progress in Aerospace Sciences **38**, 145 (2002).

[56] F. R. Menter, M. Kuntz, and R. Langtry, *Ten years of industrial experience with the SST turbulence model,* in *Proceedings of the Fourth International Symposium on Turbulence, Heat and Mass Transfer* (2003) pp. 625–632.

[57] P. SPALART and S. ALLMARAS, *A one-equation turbulence model for aerodynamic flows,* in *30th Aerospace Sciences Meeting and Exhibit* (American Institute of Aeronautics and Astronautics, 1992).

[58] A. A. Matyushenko and A. V. Garbaruk, *Adjustment of the k-ω SST turbulence model for prediction of airfoil characteristics near stall,* Journal of Physics: Conference Series **769**, 012082 (2016).

[59] R. B. Langtry and F. R. Menter, *Correlation-based transition modeling for unstructured parallelized computational fluid dynamics codes,* AIAA Journal **47**, 2894 (2009).

[60] J. D. A. Jr., *Introduction to Flight* (McGraw-Hill, 2016).

[61] B. M. Kulfan, *Universal parametric geometry representation method,* Journal of Aircraft **45** (2008), 10.2514/1.29958.

[62] E. N. Jacobs, K. E. Ward, and R. M. Pinkerton, *The Characteristics of 78 Related Airfoil Sections from Tests in the Variable-Density Wind Tunnel*, Technical Report 460 (National Advisory Committee for Aeronautics, Langley Field, VA, 1933) originally published November 1933; reprinted 1935.

[63] M. Drela and H. Youngren, *AVL 3.36 User Primer*, Massachusetts Institute of Technology (2022).

[64] E. Obert, *Aerodynamic Design of Transport Aircraft* (IOS Press, 2009).

[65] F. Nicolosi, P. Della Vecchia, D. Ciliberti, and V. Cusati, *Fuselage aerodynamic prediction methods,* Aerospace Science and Technology **55**, 332 (2016).

[66] R. Vos and S. Farokhi, *Introduction to Transonic Aerodynamics*, Fluid Mechanics and Its Applications (Springer, 2015).

[67] A. Elham, *Adjoint quasi-three-dimensional aerodynamic solver for multi-fidelity wing aerodynamic shape optimization,* Aerospace Science and Technology **41**, 241 (2014).

[68] A. Gerasimov, *Modelling turbulent flows with FLUENT,* Lecture slides, ANSYS/Fluent Europe Ltd. (2006), slide 9. Available at: https://www.ae.metu.edu.tr/seminar/Turbulence_Seminar/Modelling_turbulent_flows_with_FLUENT.pdf.

[69] P. R. Spalart and C. L. Rumsey, *Effective inflow conditions for turbulence models in aerodynamic calculations,* AIAA **45** (2007), https://doi.org/10.2514/1.29373.

[70] M. Casey and T. Wintergerste, *ERCOFTAC Best Practice Guidelines for Industrial Computational Fluid Dynamics* (ERCOFTAC, 2000).

[71] E. N. Jacobs, R. M. Pinkerton, and H. Greenberg, *Tests of related forward-camber airfoils in the variable-density wind tunnel*, Tech. Rep. 610 (National Advisory Committee for Aeronautics, 1937).

[72] P. Georgopoulos, J. Sodja, and R. de Breuker, *Prototype wing design and manufacturing for reflexed airfoil morphing,* in *Engineering Proceedings*, Vol. 133 (2026).

[73] ATR, *Atr 72-600 factsheet,* Aircraft Factsheet, ATR (2023), available at: https://www.atr-aircraft.com.

[74] G. L. Gentry, Jr., M. Takallu, and Z. T. Applin, *Aerodynamic Characteristics of a Propeller-Powered High-Lift Semispan Wing*, Tech. Rep. Technical Memorandum 4541 (National Aeronautics and Space Administration, 1994).